ELEKTRİK-ELEKTRONİK VE HABERLEŞME MÜHENDİSLİĞİ

Editör: Doç.Dr. Zafer ORTATEPE

ELEKTRİK-ELEKTRONİK VE HABERLEŞME MÜHENDİSLİĞİ

Editör

Doç. Dr. Zafer ORTATEPE

yaz
yayınları

2024

yaz
yayınları

ELEKTRİK-ELEKTRONİK VE HABERLEŞME MÜHENDİSLİĞİ

Editör: Doç. Dr. Zafer ORTATEPE

İÇİNDEKİLER

COMPARISON OF ISOLATED WORD RECOGNITION RATES OF CLASSICAL CVA AND A NEW CVA ALGORITHM FOR SUFFICIENT DATA CONDITIONS

Serkan KESER[1]

1. INTRODUCTION

In isolated word recognition, words are received as a list of words separated by a delay, and each word is processed separately [1-2]. Isolated word recognition involves receiving a word input as an audio file. The audio file is then converted into a set of feature vectors. The word recognizer requires a classifier unit that inputs a test feature vector and assigns it to the word of interest [3]. A lot of work has been done in the field of word recognition, but there is still a need for algorithms to improve recognition rates.

In the pursuit of advancing sophisticated speech recognition systems, the CVA is known to perform well in terms of both recognition accuracy and computational efficiency, particularly for recognition problems [4-8]. The fundamental principle of CVA is to identify a single common vector for each class, representing invariant features that distinguish different classes within a recognition system. With the common vector, unwanted data, such as environmental noises, personal speech variations, etc., are eliminated from the speech signal, and a

[1] Dr. Öğr. Üyesi, Kırşehir Ahi Evran Üniversitesi, Mühendislik Mimarlık Fakültesi, Elektrik Elektronik Mühendisliği, skeser@ahievran.edu.tr, ORCID: 0000-0001-8435-0507.

common vector representing the common features of the spoken signals is found [9]. CVA has been extensively used in fields such as image recognition, speech recognition, isolated word recognition, phoneme recognition, and error detection [10-15]. Traditional subspace methods like Principal Component Analysis (PCA) and Fisher's Linear Discriminant Analysis (FLDA) often encounter dimensionality and large data issues with datasets where the number of samples exceeds the number of dimensions [16-18]. The CVA overcomes these challenges by focusing only on intra-class variability and not using inter-class distribution, which is frequently encountered in high-dimensional spaces.

The difference and indifference subspaces are entirely separate in scenarios where the number of samples does not exceed the number of feature dimensions during the training phase. However, when this number is exceeded, these two subspaces do not entirely separate, resulting in non-zero eigenvalues. The eigenvectors corresponding to the smallest k non-zero eigenvalues are used for classification. A projection matrix is found using these eigenvectors, and the test signal is projected onto the indifference subspace by multiplying it with this projection matrix. The class is then determined by measuring the Euclidean distance between the projected vector and the common vectors of the classes, selecting the class with the smallest distance. However, with large databases, the two subspaces may intermingle more, potentially negatively affecting classification performance.

This study proposes a novel approach to enhance class performance. Instead of identifying a single common vector per class as in classical CVA, it suggests dividing the sample count of each class into k equally sized subsets and finding *k* common vectors (MCV), potentially increasing recognition performance. This approach could better reflect natural variations in the speech database for large datasets. Additionally, this reduces the mixing

between difference and indifference subspaces due to the decreased sample count per class. Using MCV for each class may provide a more comprehensive classification. The proposed MVA assigns a test signal to the most suitable class among the selected k classes. Besides the Euclidean distance measure, correlation and city block distance measures are also employed. This CVA-based method is applied for the first time in the literature.

The first step of the study involves using the obtained common vectors as features. In the second step, the common vector features are used to train classifiers. This approach provides the adaptation and flexibility required by modern speech recognition systems. The proposed method leverages CVA's strong feature extraction capabilities while utilizing other algorithms' robust classification capacities. Traditional classification methods such as KNN, SVM, LSTM networks, and classifiers like CVA were employed in this study. This combination helps to tackle nonlinear problems while modeling time-varying data structures with the advantages offered by LSTM.

For each split data set of all classes, the class-specific within-class scatter matrix (Sw) is used, and projection matrices obtained with the eigenvectors corresponding to the smallest t eigenvalues are found, forming the common vectors. This new approach is considered a significant step in improving recognition rates. For each test signal, the evaluation of distance measures as many as the number of common vectors, and selecting the most suitable class through a majority vote process is critical. Unlike classical CVA, which compares a test signal with a single common vector of a class, the classification process ends without further action if the test signal is incorrectly assigned. In the proposed method, k distances are found, some of which may be incorrectly classified, while others may be correctly classified.

Thus, MVA is implemented to achieve the most class assignments from the obtained k class assignments. Experimental studies on standard data sets show that the proposed classification method significantly outperforms the traditional CVA method. The proposed method offers more advantages in processing large and complex data sets. These advantages include finding the MCV for a class by dividing the database into sub-datasets, enabling the correct class assignment of a potentially misclassified signal through majority voting, and using machine learning and deep learning classifiers to classify with the obtained common vector features. This study opens new avenues for theoretical research and offers the potential to enhance the reliability and accuracy of speech recognition systems in real-world applications.

2. MATERIAL AND METHOD

2.1. Material

This study utilized 30 individuals from the MNIST speech database, each uttering the digits 0-9. Each person utters a digit 50 times, with 40 instances used for training and 10 for testing. For feature extraction in the speech recognition system, 60-dimensional i-vectors for each utterance, 13-dimensional feature vectors composed of MFCC coefficients for each frame, and 26-dimensional feature vectors composed of MFCC+GTCC coefficients were used. The training set consisted of 400 utterances per digit for each of the 30 speakers, resulting in 12,000 utterances. Each utterance was represented by an i-vector, yielding a 12,000×60 i-vector matrix. For testing, 3,000 i-vectors were used (3,000×60). The MFCC coefficients were obtained by concatenating frames of each speech signal to form 455-dimensional features (35 frames × 13 coefficients). For speech signals with fewer than 35 frames, random small amplitude

values were appended to reach 455 dimensions. For signals with more than 455 dimensions, only the first 455 values were taken. This approach resulted in 12,000×455 dimensional training features for MFCC coefficients and 3,000×455 for testing. For MFCC+GTCC, 26-dimensional features (13 MFCC + 13 GTCC) were used per frame. Using 35 frames as a reference, 910-dimensional features were obtained, resulting in 12,000×910 training features and 3,000×910 testing features. The study also evaluated the performance of the *i* vector-based feature extraction method compared to results obtained using MFCC and MFCC+GTCC features.

2.2. Method

This study examines the hybrid application of various classifiers developed for isolated word recognition problems. The CVA finds k common vectors for each class when creating hybrid classifiers. For a total of l classes, k×l common vectors are generated. These common vectors are used as features, and classifiers such as KNN, SVM, and LSTM are trained with these features. A test signal is projected onto the indifferent subspace using k projection matrices during the testing phase. The resulting k vectors are classified using the trained classifiers based on Euclidean, correlation, and city block distance measures. The test signal is then assigned to the most suitable class among the k classes using the MVA. Classification is performed according to the k×l common vectors found using CVA.

As a result, a classification method that has not been used in the literature before has been tested for the first time. This method can enhance recognition performance and is thoroughly examined for KNN, SVM, LSTM, and CVA classifiers. In addition to these classifiers, the classical CVA is also utilized. A single projection matrix and a single common vector for each class are found for classical CVA. However, in addition to the

classical Euclidean measure, correlation and city block distance measures are also used as classification criteria.

2.2.1. Feature Extraction during Training with CVA

The process of using the CVA for feature extraction is explained in the following steps. Throughout the study, sufficient data conditions mixed different and indifferent subspaces.

Step 1: *Clustering the Dataset*

The features (x) found for each class in the training set are divided into k sub-clusters. This allows for the emergence of different features for each class and addresses intra-class variance in more detail.

Step 2: *Calculation of Projection Matrices*

A separate projection matrix $(P_m, m = 1,2, \dots, k)$ is calculated for each sub-cluster. To find the projection matrix, the within-class scatter matrix of the m-th sub-cluster $(S_{w,m})$ is calculated using the following formula:

$$S_{w,m} = \sum_{i=1}^{l} \sum_{r=1}^{n} \left(\left(x_{r,m}^i - \mu_{i,m} \right) \left(x_{r,m}^i - \mu_{i,m} \right)^T \right) \qquad (1)$$

Here, i represents the class index (i=1,2,…,l), l is the number of classes, n is the number of features in the sub-cluster of the i-th class, r is the feature index (r=1,2,…,n), and m is the sub-cluster index (m=1,2,…,k). The dimension of the feature vector x is q. Then, the eigenvalues and eigenvectors for each within-class scatter matrix $(S_{w,m})$ are calculated. Projection matrices are found using the eigenvectors corresponding to the smallest t eigenvalues. If the matrix of eigenvectors for the *m*-th sub-cluster is denoted as $U_{a,m}$ $(U_{a,m} \in R^{q \times t})$, the projection matrices for the k sub-clusters are found as follows:

$$P_m = \left(U_{a,m} \right) \left(U_{a,m} \right)^T, \text{m=1,2,…,k} \qquad (2)$$

where, $P_m \in R^{q \times q}$.

Step 3: *Calculation of Common Vector Features*

The common vector $(x_{m,i}^{com})$ for the *i*-th class in each subset is found by taking the column-wise average of the product of the projection matrix P_m and the feature matrix $X_{m,i}$ of the *i*-th class in the subset.

$$x_{m,i}^{com} = average(X_{m,i} \times P_m) \tag{3}$$

Here, $X_{(m,i)} \in \mathbb{R}^{n \times l}$. A total of $k \times l$ common vectors are obtained. For each class, there are k common vectors. These common vectors were used as features to train the classifiers and are called multiple common vectors (MCV).

2.2.2. Classification and Majority Voting Algorithm

2.2.2.1. Classification

The KNN, SVM, LSTM Networks, and CVA are used for classification. Classifying a test feature x is first multiplied by k projection matrices, and the distances to all common vectors are calculated. These distances are computed as follows:

$$d_{m,i} = \text{distance}\left(xP_m, x_{m,i}^{com}\right) \tag{4}$$

The distance () refers to Euclidean, Correlation, or Cityblock distances $(i = 1,2, \dots l, m = 1,2, \dots, k)$. Then, the test feature x is assigned to the k classes that yield the shortest distances. Using the obtained distances $d_{m,i}$, the closest class for each projection matrix is determined for the test signal x. These classes, $C_1, C_2, \dots, C_l$ represent the k class assignments.

$$C_j = \arg\min_i \left(d_{m,i}\right) \tag{5}$$

As a result, for a test signal x, k classes are determined (j=1,2,…,k). The majority voting method decides which of the determined classes will be selected. Majority voting determines

which class a test signal is assigned to the most. The test signal is assigned to the class with the highest number of assignments. However, in some cases, a test signal may be assigned equally to different classes. In such cases, the class with the smallest average distance is selected.

The block diagram shown in Fig. 1 illustrates the training and testing processes described above. During the training phase, the data for each class is divided into k equal parts. For all classes, k within-class scatter matrices and projection matrices are obtained. Then, $k \times l$ common vectors are found. Using the class labels, training is performed for KNN, SVM, and LSTM. Since CVA is a subspace classifier, it does not require such training. During the testing phase, a test signal is multiplied by the k projection matrices obtained in the training phase to find the x_m vectors. Each of these vectors is classified according to a distance measure. Then, the MVA assigns the test signal to the most appropriate class.

Figure 1. Test and Training Phases of the Proposed Method for Recognition
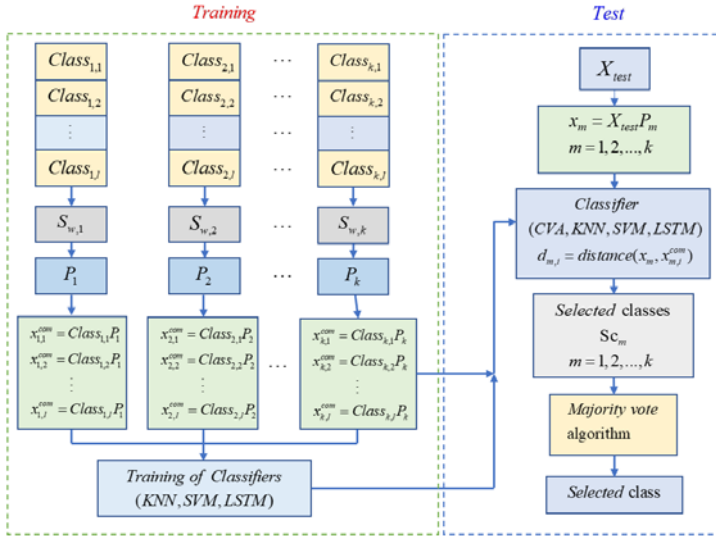
2.2.2.2. Majority Voting Algorithm (MVA)

For class selection, the class with the most assignments is chosen using the MVA. If multiple classes have the same number of assignments, the class with the smallest average distance among them is selected. First, the number of times each class is selected is found using the following Eq. 6.

$$f(C_i) = \sum_{j=1}^{k} \delta(C_i, C_j) \tag{6}$$

Here, $f(C_i)$ is the frequency of selection for the i-th class. The δ function is defined as $\delta(a, b) = 1$ if $a = b$; otherwise, it is 0. If multiple classes are selected with the same frequency, the following equation is used:

$$C_f = \arg \min_{i \in S} \left(\frac{1}{f(C_i)} \sum_{j=1}^{k} d_{m,j} \times \delta(C_i, C_j) \right) \tag{7}$$

Here, S is the set of classes with the highest frequency. C_f is the class with the smallest average distance.

2.3. The Classifiers Used in the Study

The hybrid classification approach offers a more comprehensive and flexible recognition system than using a single common vector for the CVA, providing advantages, particularly in applications requiring diversified classification strategies. Below is an explanation of how the classifiers used in this study are applied.

2.3.1. K-Nearest Neighbors (KNN)

KNN is a simple and practical classification method that classifies a test sample based on its k nearest neighbors [19]. In this study, the KNN algorithm was tested with k=5. The recognition performance of KNN was measured using various distance metrics such as Euclidean, Manhattan (Cityblock), and Pearson Correlation.

2.3.2. Support Vector Machines (SVM)

SVM is a robust classifier that seeks to find the optimal separating hyperplane in the feature space [20,21]. In this study, the recognition performance of SVM was evaluated using linear and polynomial kernel functions based on the MCV obtained for each class. SVM is effective in high-dimensional data spaces and was operated to maximize the inter-class separation of common vectors obtained through OVY.

2.3.3. Long Short-Term Memory (LSTM) Networks

LSTM is an advanced type of neural network particularly effective for modelling time-varying data structures [22,23]. In this study, LSTM networks were trained using multiple common vectors for each class, and the contribution of these vectors to the recognition performance was investigated. LSTM is critical in understanding the context over time and learning long-term dependencies, especially in audio signal processing. The LSTM network architecture of this study consists of an input layer, an LSTM layer containing 80-dimensional hidden layer units, a fully connected layer, a softmax classification layer, and classification output. Fig. 2 shows the LSTM structure used for N-dimensional feature vectors.

Figure 2. The Recognition Block Diagram Of The LSTM Network For N-Dimensional Test Feature Vector
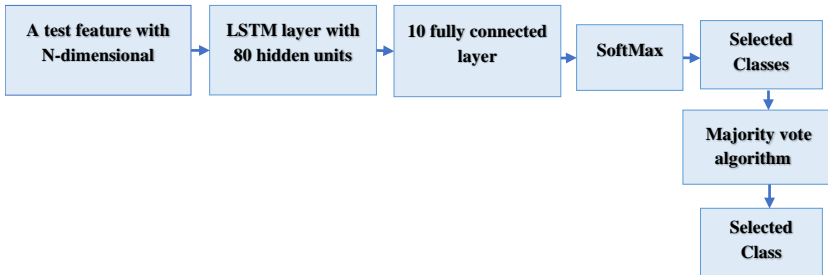
2.3.4. Common Vector Approach (CVA)

In this study, CVA was used both for feature extraction and for classifying these features. In addition to the Euclidean distance metric traditionally used by CVA, correlation and city block distance metrics were also tested.

3. EXPERIMENTAL STUDIES

The MNIST database is a dataset where 60 people voiced digits from 0 to 9. In this study, a total of 12,000 speech signals from 30 people were used for training, and 3,000 speech signals were used for testing. The sampling frequency of the audio signals is 16,000 Hz. Features were extracted by overlapping 30 ms frames by one-third of their length. Each person has 400 speech signals for training, with 40 speech signals per class. There are a total of 10 classes representing the digits 0 to 9. For testing, each person has ten speech signals per class, totalling 100 speech signals. During both the training and testing phases, 13 MFCC and 13 GTCC coefficients were obtained from each frame of the speech signals. The average number of frames was taken as 35. For speech signals longer than 35 frames, only the first 35 frames were used, while for speech signals shorter than 35 frames, the missing frames were filled by generating random small-valued numbers to match 35 frames. These frames were concatenated side by side to obtain feature vectors of 910 dimensions ($= 26 \times 35$). The results obtained using the 910-dimensional vectors formed by concatenating the MFCC and GTCC feature vectors obtained from each frame are given in Table 1 and Table 2 below. Similar procedures were performed for the 13-dimensional MFCCs to obtain 455-dimensional features, and the results are shown in Table 3 and Table 4. Table 1 gives the recognition rates obtained using Euclidean, correlation, and city block distance metrics with classical CVA. The recognition rates were found

using the eigenvectors corresponding to the smallest t eigenvalues. Here, the eigenvectors corresponding to the smallest eigenvalues from $Dim_t = 704$ to $Dim_t = 720$ were used for classification. The subscripts in the tables indicate the abbreviations for the distances (Euclidean (euc), Correlation (corr), and Cityblock (cb)). Dim_t represents the number of eigenvectors corresponding to the smallest eigenvalues used.

Table 1. Recognition Rates Found Using CVA Without Majority Voting

Dim$_t$	CVA$_{euc}$	CVA$_{corr}$	CVA$_{cb}$
720	94.60	94.26	93.23
719	94.76	95.00	93.86
718	94.46	**95.13**	93.53
717	94.66	95.06	93.86
716	94.63	95.00	94.13
715	94.80	94.66	94.23
714	95.06	94.86	94.53
713	94.86	94.53	94.00
712	94.60	94.66	94.10
711	94.53	94.40	**94.26**
710	95.06	94.90	94.56
709	**95.63**	95.50	94.80

According to the results in Table 1, the highest recognition rates using classical CVA were obtained with the Euclidean distance metric for $Dim_t = 709$ at 95.63% and with the correlation distance metric for $Dim_t = 718$ at 95.13%. These rates are higher compared to the Euclidean distance metric. For Table 2, 10 projection matrices and a total of 100 common vectors were used, and the MVA was applied for recognition. For KNN, classification was performed with $k = 5$ neighbors across all tables.

Table 2. Results Found with A Majority Vote for Ten Projection Matrices and 100 Common Vectors

Di m_t	CVA$_e$ uc	CVA$_{co}$ rr	CVA cb	KNN$_e$ uc	KNN$_{co}$ rr	KNN cb	SVM$_l$ in	SVM$_p$ ol	LST M
720	97.23	97.03	97.30	93.73	93.90	93.13	93.06	87.50	93.36
719	97.36	97.10	97.30	93.40	93.96	93.00	92.83	86.40	93.80
718	97.46	97.03	97.23	94.43	94.63	93.33	92.60	88.30	94.03
717	97.36	97.26	97.26	93.70	94.13	93.16	91.47	90.03	93.33
716	97.46	97.16	97.40	93.90	94.10	93.50	93.66	90.43	93.83
715	97.46	96.96	97.33	93.90	94.56	94.00	94.03	90.30	94.20
714	97.40	97.20	97.36	94.06	94.43	94.20	93.40	90.30	94.13
713	97.30	97.06	**97.54**	93.60	94.23	93.90	93.66	90.60	93.83
712	97.26	97.16	97.43	94.03	**94.70**	94.43	93.33	90.56	93.23
711	97.30	97.16	97.26	93.90	94.50	94.50	93.73	90.66	93.56
710	97.40	97.23	97.26	93.56	94.43	94.00	94.03	91.16	93.40
709	97.10	97.16	97.33	93.40	94.30	93.93	94.13	91.70	93.53

Table 2 shows that CVA's highest recognition rate was 97.54%, with the cityblock distance metric for Dim$_t$=713. The recognition rate obtained with majority voting is higher than the classical CVA in Table 1. In Table 2, the highest recognition rate for KNN reached 94.7%, while SVM and LSTM gave lower recognition rates than KNN. Fig. 1 and Fig. 2 show the indices of the wrongly recognized speech signals according to the values providing the highest recognition rate (95.63%, 97.54%) in Table 1 and Table 2, respectively. There are 3000 indices for 3000 test signals. For ease of presentation, only the index of the first 18 wrongly recognized signals are shown in bar graphs. The red bars show the index of the common wrongly recognized signals resulting from the two classifications.

Figure 3. Indices of Incorrectly Recognized Signals for CVAeuc in Table 1 (k=709).
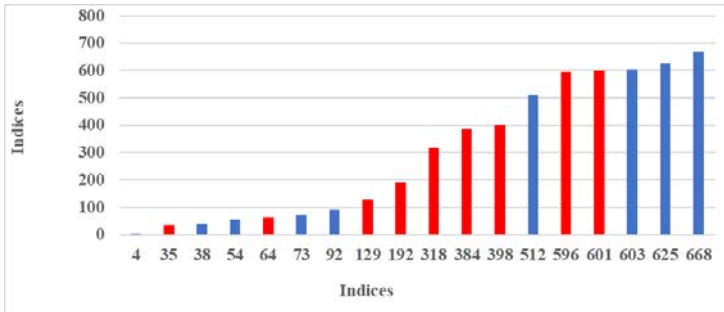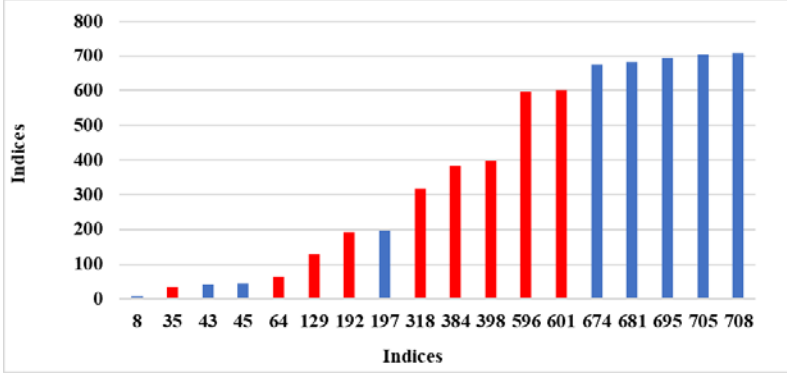
Figure 4. Indices of Incorrectly Recognized Signals for CVAcb in Table 2 (k=714)

When the results obtained by the classical CVA and the proposed classification method for the misrecognized sound signal with index 73 in Figure 3 are examined, it is found that the classical CVA_{euc} assigns the sound signal with index 73 in Figure 1 to class 2 (two) (k=709). The true class of this audio signal is seven. The same signal was assigned to 10 classes with the CVA_{cb} classifier of the proposed classification method. These are h= [2, 7, 7, 7, 2, 7, 7, 7, 7, 7, 9, 7, 7] class sequences. With the classification method proposed with the MVA, class 7 was selected for this sequence. In the analyses, it was observed that many signals that were misclassified with the classical CVA were assigned to the correct class with the proposed method. This is clearly seen when the recognition rates are analysed. Table 3 shows the recognition results obtained with CVA for 455-dimensional MFCC features without using the MVA.

Table 3. Results That Were Found Without Majority Votes for CVA.

Dim$_t$	CVA$_{euc}$	CVA$_{corr}$	CVA$_{cb}$
390	94.33	94.33	93.60
389	93.83	94.16	93.46
388	94.43	94.63	93.70
387	94.40	**94.80**	93.96
386	93.73	93.96	93.00
385	94.33	94.20	93.30
384	94.60	94.36	93.80
383	94.23	94.10	93.53
382	94.23	94.10	93.93
381	93.70	93.43	93.03
380	93.76	93.40	93.03
379	93.83	93.40	92.73

Table 3 shows that the Cityblok distance criterion gives the highest recognition rates. The highest recognition rate is 91.16% for *Dim$_t$*=382. For Table 4, 10 projection matrices and 100 common vectors were used, as shown in Table 2. The size of MFCC features is 455. The MVA was applied for recognition.

Table 4. Results That Were Found With A Majority Vote for Ten Projection Matrices And 100 Common Vectors

Dim$_t$	CVA$_{euc}$	CVA$_{corr}$	CVA$_{cb}$	KNN$_{euc}$	KNN$_{corr}$	KNN$_{cb}$	SVM$_{lin}$	SVM$_{pol}$	LSTM
390	95.06	95.16	94.03	89.20	90.20	90.53	89.50	82.50	93.3
389	94.73	94.96	94.16	89.46	90.43	91.30	89.23	83.33	92.86
388	95.13	94.96	94.36	90.26	91.26	91.46	89.30	82.56	93.56
387	94.90	**95.16**	94.53	90.43	91.40	91.76	90.20	82.80	**93.96**
386	95.06	94.83	94.36	89.83	91.00	91.96	89.90	81.40	93.43
385	**95.33**	94.90	94.43	90.13	91.10	92.00	90.86	81.86	93.43
384	94.80	94.63	94.23	90.06	90.76	92.00	90.70	78.90	92.96
383	94.73	94.60	94.40	90.43	91.06	91.86	90.20	82.73	92.90
382	95.06	94.70	94.16	91.16	91.20	92.06	90.03	80.86	92.26
381	94.50	94.23	93.93	90.46	90.70	91.23	90.50	83.40	92.13
380	94.33	94.00	93.86	90.93	90.73	91.60	90.43	82.03	91.86
379	94.10	93.80	93.90	90.40	90.23	92.16	89.90	81.13	92.63

According to the results in Table 4, the highest recognition rate of 95.33% was obtained using the **CVA$_{euc}$**. While the highest recognition rate in Table 3 without a majority vote was 94.80%, it is seen that the recognition rate increases to 95.33% when a majority vote is used in Table 4. This clearly shows the advantage of using a majority vote. The same situation is valid for Table 1

and Table 2. While the highest recognition rate obtained in Table 1 is 95.63%, the highest recognition rate increases to 97.54% in Table 2, where a majority vote is used. **KNN$_{cb}$, KNN$_{corr}$,** and **KNN$_{euc}$** showed lower recognition performance. **SVM$_{lin}$** has the best performance among SVM methods with 90.86%, while **SVM$_{pol}$** has the lowest recognition rate with 83.40%. **LSTM** showed a good performance with the highest recognition rate of 93.96%. In Table 5 and Table 6, i-vectors with a size of 60 were used as features and recognition was performed. Projection matrices were found using eigenvectors corresponding to the smallest eigenvalues between 9-21 and used in recognition. In Table 5, recognition was performed with classical CVA using one projection matrix and ten common vectors. In Table 5, the highest recognition rate was 99.55% with Euclidean and Cityblok distance criteria.

Table 5. Results That Were Found Without Majority Vote for CVA.

Dim$_t$	CVA$_{euc}$	CVA$_{corr}$	CVA$_{cb}$
21	99.35	99.35	99.45
20	99.42	99.42	99.42
19	99.42	99.42	99.45
18	99.52	99.45	99.38
17	99.48	99.42	99.38
16	99.52	99.45	99.38
15	99.45	99.38	99.42
14	99.42	99.38	99.42
13	99.45	99.38	99.45
12	99.45	99.48	99.52
11	99.55	99.52	99.45
10	99.55	99.48	99.52
9	99.52	99.52	99.55

Table 6 shows that the recognition rates of the classifiers are all above 99%. The highest recognition rates were 99.69% for CVA_{euc} and CVA_{cb} methods. CVA_{corr} and KNN_{euc} methods share the highest recognition rates with 99.62%. KNN_{cb} also showed high performance with 99.69%. SVM_{lin} and SVM_{pol} were

relatively low at 99.42% and 99.35% respectively. The LSTM method gave the highest recognition rate of 99.59%. When these results are compared with Table 5, they show that the majority vote method effectively increases recognition rates, and the best performance is obtained when the Dim_t dimension is between 9-11.

Table 6 Results That Were Found With A Majority Vote for Ten Projection Matrices And 100 Common Vectors.

Dim_t	CVA_{euc}	CVA_{corr}	CVA_{cb}	KNN_{euc}	KNN_{corr}	KNN_{cb}	SVM_{lin}	SVM_{pol}	LSTM
21	99.38	99.35	99.35	99.28	99.31	99.45	99.14	98.87	99.38
20	99.45	99.38	99.45	99.38	99.38	99.52	99.31	98.97	99.38
19	99.42	99.38	99.48	99.45	99.35	99.48	99.31	99.01	99.55
18	99.45	99.52	99.52	99.45	99.48	99.55	99.28	98.87	99.25
17	99.45	99.45	99.48	99.52	99.55	99.55	99.28	98.91	99.35
16	99.52	99.48	99.65	99.55	99.48	99.55	99.31	99.14	99.48
15	99.52	99.48	99.65	99.48	99.48	99.55	99.21	99.35	99.38
14	99.52	99.52	99.55	99.55	99.48	99.59	99.42	99.14	99.35
13	99.55	99.52	99.52	99.52	99.52	99.52	99.38	99.11	99.59
12	99.48	99.52	99.45	99.48	99.52	99.48	99.35	99.21	99.45
11	99.62	99.59	99.48	99.62	99.62	99.48	99.42	99.14	99.42
10	99.62	99.62	99.55	99.55	99.48	99.65	99.14	97.85	99.42
9	99.69	99.55	99.69	99.62	99.48	99.69	99.21	97.99	99.45

As a result, when Table 5 and Table 6 using i-vector are compared, it is seen that the results in Table 6 using majority voting are higher than Table 5 with 99.69%.

4. CONCLUSIONS

This study proposes a new method to improve recognition rates using the CVA in isolated word recognition systems. To better represent intra-class variations in large databases, the proposed method divides the dataset of each class into k subsets and calculates separate projection matrices and common vectors for each subset. This process creates a more detailed and flexible recognition system than the traditional CVA method. Experiments using various classifiers such as KNN, SVM, LSTM, and CVA have shown that using multiple common vectors instead of a single common vector significantly increases

the recognition rates. In the proposed method, the samples of each class are divided into k subsets and projection matrices, and common vectors are calculated for each subset. Classifiers are trained with these common vectors.

In the test phase, each test signal is projected into the indifference subspace with k projection matrices, k classifications are made, and the final class is determined by majority voting. The proposed method provides a significant performance improvement compared to the traditional SVM method. According to the experimental results, the recognition rates obtained using classifiers were higher than the conventional SVM method. A better representation of intra-class variations can explain this and the decrease in the interference between subspaces due to the reduction in the number of samples per class and the effects of the MVA. The MVA increases the recognition rates by reducing the probability of misclassification.

The results obtained using i vector-based feature extraction provided a recognition rate of over 99% compared to the traditional MFCC and GTCC methods. These results show that using an i-vector is a significant performance improvement compared to the recognition rate of about 97.5% given by MFCC and GTCC. It was also observed that Euclidean achieved overall higher recognition rates than Cityblock and Correlation distance measures. The proposed CVA-based hybrid classification method can potentially increase recognition rates in large datasets. This method, which better represents intra-class variations and minimizes inter-subspace interference, provides higher accuracy rates in speech recognition systems.

Moreover, the results obtained using hybrid classifiers are more advantageous than CVA alone. This study makes an essential contribution to theoretical research and real-world applications and improves the reliability of speech recognition

systems. These findings can guide the development of methods for word recognition systems and other similar classification applications. Furthermore, more detailed studies on different classification algorithms and common vector combinations can extend and optimize the application areas of this approach. Future work investigates how these techniques can be optimized for other datasets and real-world scenarios.

Conflict of Interest Statement

There is no conflict of interest between the authors.

Statement of Research and Publication Ethics

The study is complied with research and publication ethics

REFERENCES

[1] Emillia, N. R., Suyanto, S., & Maharani, W. (2012). Isolated word recognition using ergodic hidden markov models and genetic algorithm. TELKOMNIKA (Telecommunication Computing Electronics and Control), 10(1), 129-136. http://doi.org/10.12928/telkomnika.v10i1.769

[2] Sajjan, S. C., & Vijaya, C. (2012, March). Comparison of DTW and HMM for isolated word recognition. In International Conference on Pattern Recognition, Informatics and Medical Engineering (PRIME-2012) (pp. 466-470). IEEE. http://doi.org/10.1109/ICPRIME.2012.6208391

[3] Rabiner, L. R., Levinson, S. E., & Sondhi, M. M. (1983). On the application of vector quantization and hidden Markov models to speaker-independent, isolated word recognition. Bell System Technical Journal, 62(4), 1075-1105. https://doi.org/10.1002/j.1538-7305.1983.tb03115.x

[4] Gulmezoglu, M. B., Dzhafarov, V., & Barkana, A. (2001). The common vector approach and its relation to principal component analysis. IEEE Transactions on Speech and Audio Processing, 9(6), 655-662. http://doi.org/10.1109/89.943343

[5] Gülmezoğlu, M. B., Dzhafarov, V., Edizkan, R., & Barkana, A. (2007). The common vector approach and its comparison with other subspace methods in case of sufficient data. Computer Speech & Language, 21(2), 266-281. https://doi.org/10.1016/j.csl.2006.06.002

[6] Sadıç, S., & Gülmezoğlu, M. B. (2011). Common vector approach and its combination with GMM for text-

independent speaker recognition. Expert Systems with Applications, 38(9), 11394-11400. https://doi.org/10.1016/j.eswa.2011.03.009

[7] Lu, Q., Jiang, B., Gopaluni, R. B., Loewen, P. D., & Braatz, R. D. (2018). Locality preserving discriminative canonical variate analysis for fault diagnosis. Computers & Chemical Engineering, 117, 309-319. https://doi.org/10.1016/j.compchemeng.2018.06.017

[8] Günal, S., Ergin, S., Gülmezoğlu, M. B., & Gerek, Ö. N. (2006). On feature extraction for spam e-mail detection. In Multimedia Content Representation, Classification and Security: International Workshop, MRCS 2006, Istanbul, Turkey, September 11-13, 2006. Proceedings (pp. 635-642). Springer Berlin Heidelberg. https://doi.org/10.1007/11848035_84

[9] Gulmezoglu, M. B., Dzhafarov, V., Keskin, M., & Barkana, A. (1999). A novel approach to isolated word recognition. IEEE Transactions on Speech and Audio Processing, 7(6), 620-628. https://doi.org/10.1109/89.799687

[10] Kirkbas, A., Demircali, A., Koroglu, S., & Kizilkaya, A. (2020). Fault diagnosis of oil-immersed power transformers using common vector approach. Electric Power Systems Research, 184, 106346. https://doi.org/10.1016/j.epsr.2020.106346

[11] Wen, Y. (2012). An improved discriminative common vectors and support vector machine based face recognition approach. Expert Systems with Applications, 39(4), 4628-4632. https://doi.org/10.1016/j.eswa.2011.09.119

[12] Cevikalp, H., Neamtu, M., Wilkes, M., & Barkana, A. (2005). Discriminative common vectors for face

recognition. IEEE Transactions on pattern analysis and machine intelligence, 27(1), 4-13. https://doi.org/10.1109/TPAMI.2005.9

[13] Lakshmi, C., Ponnavaikko, M., & Sundararajan, M. (2010, May). Improved kernel common vector method for face recognition varying in background conditions. In International Symposium Computational Modeling of Objects Represented in Images (pp. 175-186). Berlin, Heidelberg: Springer Berlin Heidelberg. https://doi.org/10.1007/978-3-642-12712-0_16

[14] Cevikalp, H., Neamtu, M., & Barkana, A. (2007). The kernel common vector method: A novel nonlinear subspace classifier for pattern recognition. IEEE Transactions on Systems, Man, and Cybernetics, Part B (Cybernetics), 37(4), 937-951. https://doi.org/10.1109/TNN.2006.881485

[15] Keser, S., & Edizkan, R. (2009, April). Phonem-based isolated Turkish word recognition with subspace classifier. In 2009 IEEE 17th Signal Processing and Communications Applications Conference (pp. 93-96). IEEE. https://doi.org/10.1109/SIU.2009.5136340

[16] Chen, S., Liu, J., & Zhou, Z. H. (2004). Making FLDA applicable to face recognition with one sample per person. Pattern recognition, 37(7), 1553-1555. https://doi.org/10.1109/TPAMI.2012.70

[17] Takiguchi, T., & Ariki, Y. (2007). PCA-Based Speech Enhancement for Distorted Speech Recognition. Journal of multimedia, 2(5).

[18] Abolhassani, A. H., Selouani, S. A., & O'Shaughnessy, D. (2007, December). Speech enhancement using PCA and variance of the reconstruction error in distributed speech

recognition. In 2007 IEEE Workshop on Automatic Speech Recognition & Understanding (ASRU) (pp. 19-23). IEEE. https://doi.org/10.1109/ASRU.2007.4430077

[19] Mucherino, A., Papajorgji, P. J., Pardalos, P. M., Mucherino, A., Papajorgji, P. J., & Pardalos, P. M. (2009). K-nearest neighbor classification. Data mining in agriculture, 83-106. https://doi.org/10.1007/978-0-387-88615-2_4

[20] Awad, M., Khanna, R., Awad, M., & Khanna, R. (2015). Support vector machines for classification. Efficient learning machines: Theories, concepts, and applications for engineers and system designers, 39-66.

[21] Cevikalp, H. (2016). Best fitting hyperplanes for classification. IEEE transactions on pattern analysis and machine intelligence, 39(6), 1076-1088. https://doi.org/10.1109/TPAMI.2016.2587647

[22] Jadhav, S., Zhao, J., Fan, Y., Li, J., Lin, H., Yan, C., & Chen, M. (2023). Time-varying sequence model. Mathematics, 11(2), 336. https://doi.org/10.3390/math11020336

[23] An, Z., Li, S., Wang, J., & Jiang, X. (2020). A novel bearing intelligent fault diagnosis framework under time-varying working conditions using recurrent neural network. ISA transactions, 100, 155-170. https://doi.org/10.1016/j.isatra.2019.11.010

DESIGN AND CONTROL OF BIDIRECTIONAL THREE-PHASE T-TYPE INVERTER

Zafer ORTATEPE[1]

1. INTRODUCTION

Power electronics technology has been the cornerstone of modern energy systems, enabling efficient conversion and control of electrical power in a wide range of applications. With the growing demand for renewable energy integration and advanced industrial drives, the need for more efficient and reliable inverter topologies has intensified. Conventional two-level inverters, although widely used, face challenges such as high switching losses, significant electromagnetic interference (EMI), and elevated total harmonic distortion (THD), particularly in high-power applications (Franquelo et al., 2008). In response, multi-level inverter topologies, including the three-level T-type inverter, have been developed to address these limitations by offering improved efficiency, enhanced power quality, and reduced THD (Abu-Rub, Holtz, Rodriguez, & Baoming, 2010).

The T-type inverter, is particularly attractive for medium and high power applications due to its simple structure (Ngo, Nguyen, Tran, Lim, & Choi, 2018). Unlike conventional two-level inverters, which generate only two voltage levels at the output, the T-type inverter generates three voltage levels, resulting in lower switching frequencies, reduced losses, and improved harmonic performance (Huynh, Ho, & Chun, 2020). The lower voltage stress and improved power quality make the T-

---

[1] Assoc. Prof. Dr., Pamukkale University, Faculty of Technology, Department of Automotive Engineering, zortatepe@pau.edu.tr, ORCID: 0000-0001-7771-1677.

type topology especially suitable for applications such as photovoltaic (PV) systems, wind turbines, motor drives, and grid-connected systems (Alnamer, Mekhilef, & Mokhlis, 2018).

The improvement of multi-level inverters marks a significant milestone in power electronics. Early two-level inverters were limited by their high switching frequencies and the resulting switching losses, leading to increased stress on semiconductor devices. In 1981, Nabae, Takahashi, and Akagi proposed the neutral-point clamped (NPC) inverter, a three-level topology that significantly improved power conversion efficiency and reduced harmonic distortion by dividing the DC link voltage into three levels (Nabae, Takahashi, & Akagi, 1981). Building on this concept, the T-type inverter is introduced as a variant, featuring a simplified design and enhanced voltage balancing across switching devices (Schweizer & Kolar, 2013).

Multi-level inverters, including diode-clamped, capacitor-clamped, and cascaded H-bridge (CHB) topologies, have been widely explored in various applications (Cui & Ge, 2018), (He & Cheng, 2016), (Maheswari, Bharanikumar, Arjun, Amrish, & Bhuvanesh, 2021). Among these, the three-level T-type inverter strikes a balance between complexity and performance, providing an ideal solution for applications where efficiency and higher power quality are required (Do et al., 2020). The three-phase T-type inverter offers several advantages over its two-level counterparts. First, by generating three voltage levels at the output, the T-type inverter significantly reduces the rate of change of voltage (dV/dt) and the associated switching losses (Chen & Narimani, 2019). This reduction in switching stress leads to improved thermal management, extending lifespan of semiconductor devices such as insulated-gate bipolar transistors (IGBTs) and metal-oxide-semiconductor field-effect transistors (MOSFETs) (Gurpinar & Castellazzi, 2016). In addition, the three-level output reduces the harmonic content in the generated

waveforms, leading to lower THD and reducing the need for bulky output filters (De Almeida Cacau, Torrico-Bascopé, Neto, & Torrico-Bascopé, 2014).

Another advantage of the T-type inverter is its reduced EMI. Lower switching frequencies and smoother output waveforms help mitigate EMI issues, making the T-type inverter well-suited for applications such as medical equipment and aerospace systems (Roy & Banerjee, 2024). Furthermore, the reduction in losses enables the use of smaller heat sinks and cooling systems, assisting to the overall compactness of the system design (Baimel et al., 2023).

In this paper, a design for a bidirectional three-phase T-type inverter, covering the control strategies, and modulation techniques are presented. Simulation results are provided by MATLAB/Simulink to validate the proposed design. The rest of the paper as follows: Section 2 introduces the three-phase T-type inverter topology and its switching states. Section 3 gives the modulation techniques and control method. Section 4 gives the simulation results and Section 5 gives the conclusion part, respectively.

2. THREE-PHASE T-TYPE INVERTER

The three-phase T-type inverter is a variant of the NPC multi-level inverter, designed to enhance power conversion efficiency and improve voltage stress distribution across the semiconductor devices. Its unique structure allows for the generation of three voltage levels, which significantly improves output power quality and reduces switching losses.

This topology has become particularly attractive for medium and high power applications such as renewable energy systems, grid-connected power electronics, and industrial drives

due to its cost-effectiveness, reliability, and ability to achieve high efficiency with minimal complexity. The circuit diagram of the three-phase T-type inverter is given in Figure 1.

Figure 1. The Circuit of The Three-Phase T-Type Inverter
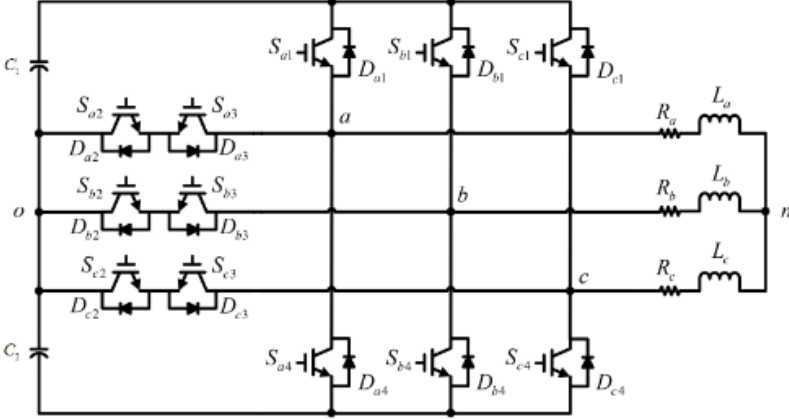
2.1. Basic Structure

The three-phase T-type inverter derives its name from the configuration of its switching elements, which resemble a "T" shape in circuit diagrams. Unlike conventional two-level inverters that generate only two output voltage levels ($+V_{dc}/2$ and $-V_{dc}/2$), the T-type inverter adds an intermediate level, 0V, resulting in three distinct voltage levels: $+V_{dc}/2$, 0, and $-V_{dc}/2$. This additional level helps in reducing the THD of the output waveform and lowering EMI. The basic structure of a three-phase T-type inverter consists of:

DC-Link: The DC link is divided into two capacitors, providing the midpoint connection necessary to achieve zero-voltage level. This midpoint helps achieve the third voltage level in the output waveform.

Switching Devices: Each leg of the three-phase T-type inverter contains two IGBT or MOSFET and two clamping diodes. The IGBT operates in conjunction with the diodes to

clamp the voltage to zero when required, ensuring the creation of the intermediate voltage level.

Clamping Diodes: The T-type inverter uses clamping diodes to direct current flow and manage voltage stress across the switches. These diodes protect the switches by clamping the voltage and reducing stress, which improves the overall reliability of the system.

2.2. Operating Principle of Single T-Type Module

The three-phase T-type inverter operates by switching between the three voltage levels based on the modulation strategy. The three-level operation is achieved through the following switching states:

Positive Voltage State: The top switch in the inverter leg is turned-on, while the bottom switch is off. This results in an output voltage of $+V_{dc}/2$.

Zero Voltage State: Both the top and bottom switches are turned-off, and the current flows through the clamping diodes. This produces a zero voltage output.

Negative Voltage State: The bottom switch is turned-on, and the top switch is off, resulting in an output voltage of $-V_{dc}/2$.

Switching states and current paths for each output voltage level of the T-type inverter topology is given in Figure 2. The combination of these switching states allows the T-type inverter to generate a three-level output voltage waveform, which improves overall efficiency and reduces the switching frequency. The zero voltage level also helps reduce the dV/dt (rate of voltage change), minimizing the switching losses and reducing the stress on the semiconductors. Besides, the switching states and output voltage levels for the leg A is given in Table 1.

Table 1. Switching States and Output Voltage Levels (Leg A)

State	Output Voltage	S_{a_1}	S_{a_2}	S_{a_3}	S_{a_4}
Positive voltage	$+V_{dc}/2$	1	0	0	0
Zero	0	0	1	1	0
Negative voltage	$-V_{dc}/2$	0	0	0	1

Figure 2. Switching States and Current Paths of the T-type Inverter Topology (leg A) (a) Positive ($+V_{dc}/2$) (b) Zero (c) Negative Voltage States ($-V_{dc}/2$)

(a)   (b)   (c)
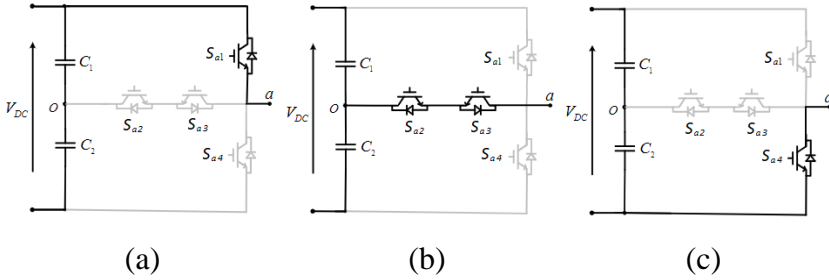
3. MODULATION AND CONTROL METHOD

3.1. Modulation Techniques

To control the switching of the T-type inverter and ensure high quality output, various pulse width modulation (PWM) techniques can be used. The most common techniques include:

Sinusoidal pulse width modulation (SPWM): SPWM is widely used in three-level inverter types due to its simplicity and effectiveness in generating high quality waveforms. By comparing a reference sine wave with carrier signals, the inverter generates switching signals that control the switching states.

Space vector modulation (SVM): SVM is another commonly used modulation technique for controlling T-type inverters. It provides superior control performance over the output voltage vector and reduces switching losses compared to

SPWM. In SVM, the three-phase voltage vector is synthesized from a combination of available switching states, reducing harmonic distortion and improving voltage utilization.

Capacitor voltage balancing modulation techniques: One of the challenges in T-type inverters is balancing the voltages across the capacitors in the DC-link. To address this, special control techniques are improved to maintain the neutral point voltage, preventing it from drifting and ensuring balanced operation.

3.2. Bidirectional Structure and Control Method

The ability to generate high-quality output with minimal harmonic distortion, reduced switching losses, and balanced voltage stresses across the switches makes the T-type inverter highly suitable for renewable energy and grid-tied inverters. Figure 3 shows the block diagram of a bidirectional three-phase T-type inverter modeled in MATLAB/Simulink. This inverter is designed to operate with three output phases (R, S, T), and it incorporates several key features of T-type topologies. The figure highlights the arrangement of power electronic devices and control signals used to achieve three-level voltage output for each phase.

Figure 3. Block Diagram of the Bidirectional Three-Phase T-type Inverter in MATLAB/Simulink
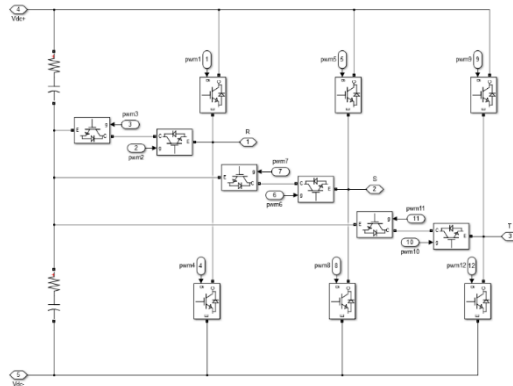
The simulation setup provided by this model is used for further analysis and testing of control strategy, modulation technique and its impact on the overall performance of the inverter in real-world scenarios.

Figure 4 shows the modulation control block for a bidirectional three-phase T-type inverter, implemented in MATLAB/Simulink. This block is responsible for generating the PWM signals that control the switching of the power devices. These PWM signals determine the output voltage levels, enabling efficient and accurate power conversion. The switching frequency is selected as 10kHz for the simulation studies.

Figure 4. Modulation Control Block of Bidirectional Three-Phase T-Type Inverter in MATLAB/Simulink
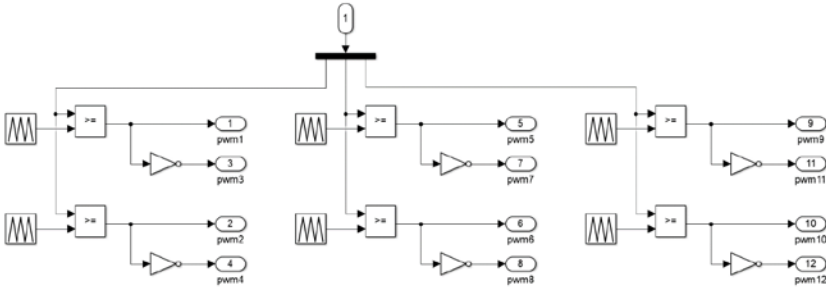
Figure 5 shows the control system block in MATLAB/Simulink for generating the dq-axis equivalents of voltage and current, using a Phase Locked Loop (PLL) for synchronization. Transformation of three-phase quantities into *dq0* components is crucial for effective control in the synchronous reference frame, commonly used in inverter systems for active and reactive power management, as well as grid synchronization. The use of PLL ensures that the inverter remains robust in operation even under varying grid conditions, making it highly suitable for grid-tied applications.

Figure 5. PLL and *dq*-axis Equivalents of Voltage and Current Generation Control Block in MATLAB/Simulink
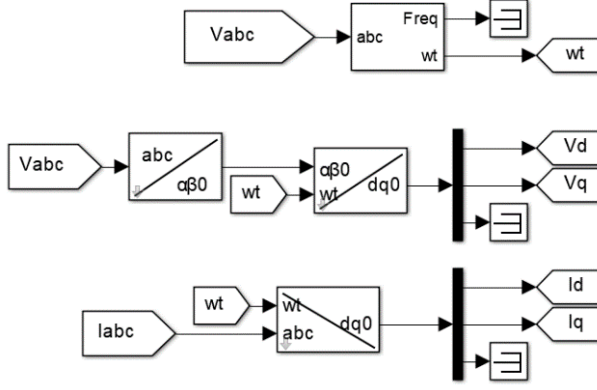
Figure 6 illustrates a control block diagram, specifically for generating *dq*-axis reference currents for a grid-connected (grid-to-load) system in MATLAB/Simulink. It emphasizes the use of closed-loop control through a PI controller to regulate the *d*-axis current, typically related to active power control, while keeping reactive power at zero (using the *q*-axis). The PI parameters of this control block is selected as $K_{P_1} = 100$ and $K_{I_1} = 5000$. Since the system is controlled with unity, the gain coefficients are determined as 1/600.

Figure 6. Grid-to-Load *dq* Reference current Generation Control Block in MATLAB/Simulink
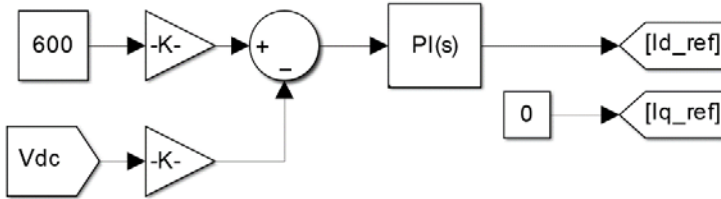
Figure 7 represents another control block diagram, but it focuses on generating *dq*-axis reference currents for a load-to-grid system in MATLAB/Simulink. The main difference from the previous figure is the inclusion of additional power inputs and

control logic that incorporates switching between two reference power levels.

Figure 7. Load to Grid dq Reference Current Generation Control Block in MATLAB/Simulink
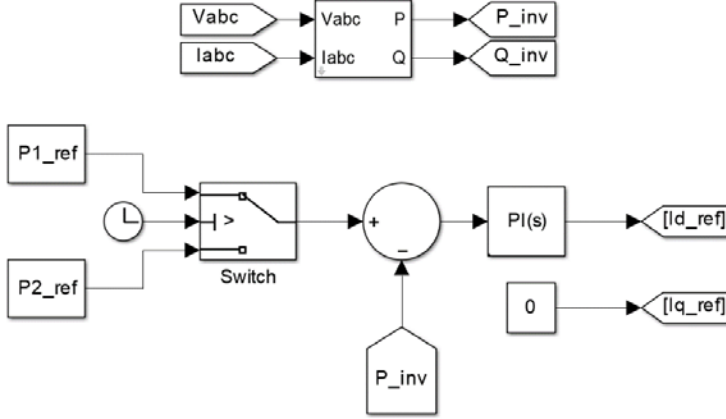
The PI controller ensures smooth dynamic response, keeping the system output in line with the desired power levels. The PI parameters of this control block is selected as $K_{P_2} = 0.001$ and $K_{I_2} = 5$. This control block diagram is typical of grid-tied power systems, where power control is crucial. The control objective is to regulate active power flow from a load-to-grid by adjusting the d-axis reference current ($I_{d_{ref}}$), which directly correlates with active power transfer in a *dq*-based control scheme.

Figure 8 shows the transformation of reference currents into modulation signals that are applied to the three-phase T-type inverter, ensuring that it produces the appropriate three-phase voltages to match the system's power requirements. The PI parameters of this control block is selected as $K_{P_3} = 10$, $K_{I_3} = 100$, $K_{P_4} = 10$ and $K_{I_4} = 100$. The modulation signals are generated based on *dq* current references to produce three-phase output voltages (V_a, V_b, V_c) for the inverter control.

Figure 8. Modulation Signal Generation Control Block in MATLAB/Simulink
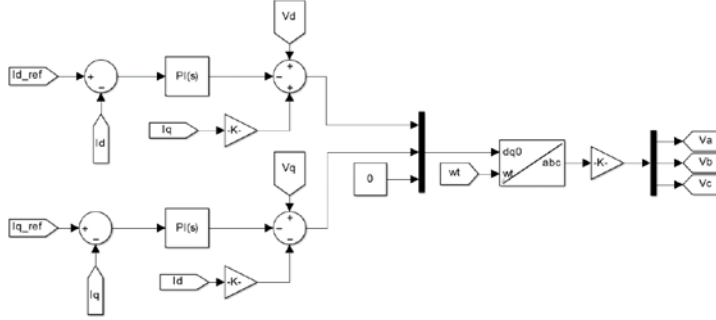
4. SIMULATION RESULTS

To validate the theoretical analysis of the bidirectional three-phase T-type inverter topology, simulation studies are performed by MATLAB/Simulink under different conditions. Table 2 shows the design and control parameters of the system.

Table 2. Design and Control Parameters Used in Simulation

Parameters	Values
Grid voltage (V_{ph-ph})	400 [V_{AC}]
Output power	10 [kW]
DC link voltage	700 [V_{DC}]
Switching frequency	10 [kHz]
LC filter inductance (L_f)	300 [uH]
LC filter capacitor (C_f)	15 [uF]
Voltage control parameters	100, 5000 (K_{P_1}, K_{I_1})
Power control parameters	0.001, 5 (K_{P_2}, K_{I_2})
Current control parameters	10, 100 ($K_{P_{3,4}}, K_{I_{3,4}}$)

Figure 9 shows the simulation layout for bidirectional three-phase T-type inverter topology in MATLAB/Simulink environment.

Figure 9. The Simulation Layout for Bidirectional Three-Phase T-Type Inverter Topology (Grid-To-Load Operation)
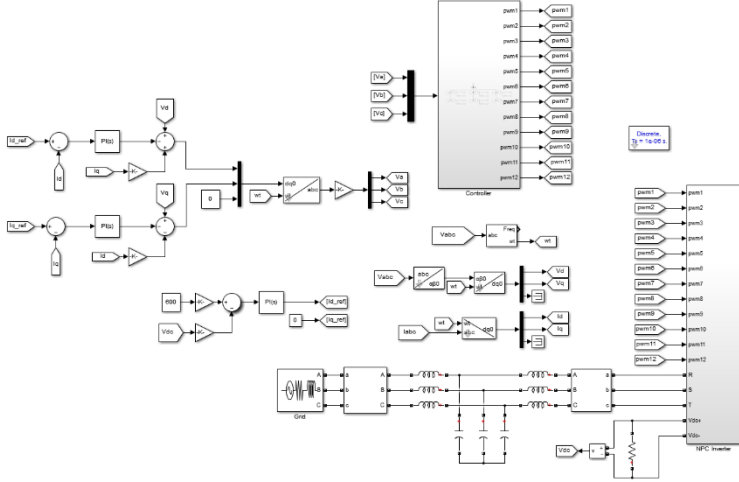
Figure 10 demonstrates a well-controlled T-type inverter, with grid synchronization achieved across all three phases. The minor differences between the grid and inverter-side voltages are a result of the inverter's switching operation, but overall, the system maintains a high level of power quality. The inverter side and grid side voltages are closely matched, which indicates that the control system of the inverter is effectively synchronized with the grid. This is crucial for grid-connected inverters, ensuring that power is transferred smoothly between the inverter and the grid without causing disturbances. Besides, the figure highlight that the inverter generates voltages with a structure close to the grid voltages in terms of amplitude and frequency, ensuring proper operation and power transfer.

Figure 10. Grid Side Voltage and Inverter Side Voltages of the Three-Phase T-Type Inverter
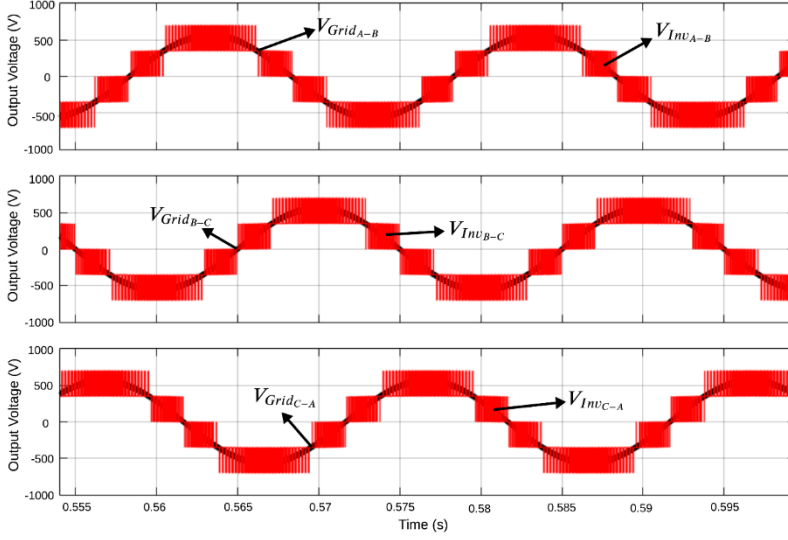
Figure 11. DC-Link Voltage of the Three-Phase T-Type Inverter
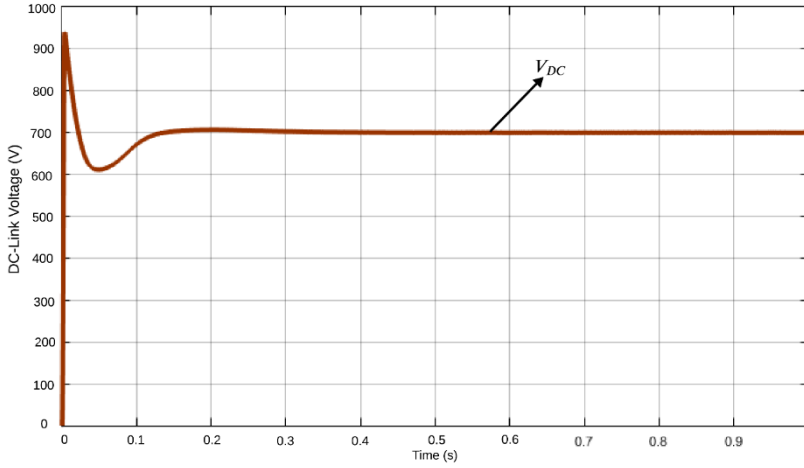
Figure 11 shows the DC-link voltage (V_{DC}) of a three-phase T-type inverter over time. Initially, there is a sharp rise in the DC-link voltage, reaching a peak of around 900 V, followed by a dip below the steady-state value. This transient behavior is typical during the inverter startup, where voltage overshoot

occurs due to capacitor charging and control adjustments. After approximately 0.2 seconds, the voltage stabilizes around 700 V, indicating that the DC-link has reached a steady operating state. A well-regulated DC-link provides proper inverter performance, reducing losses and maintaining the desired output voltage waveform quality.

Figure 12. The Modulation Signals of Three-Phase T-Type Inverter
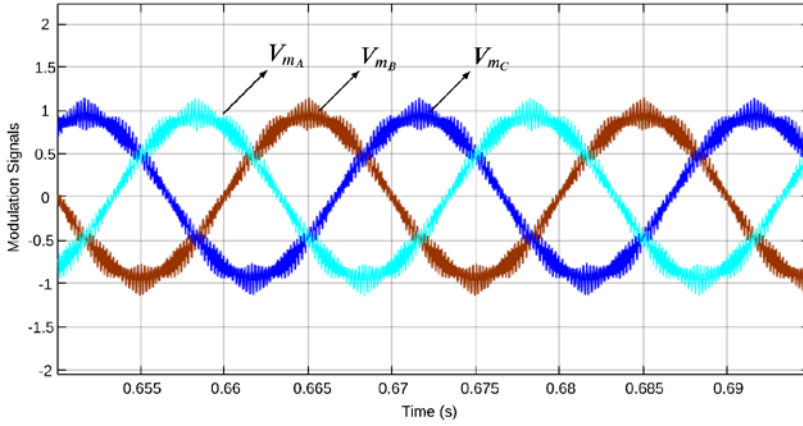
Figure 12 presents the modulation signals ($V_{m_A}, V_{m_B}, V_{m_C}$) of a three-phase T-type inverter. These signals correspond to the modulation indices for each phase in the inverter, controlling the switching states that generate the output voltage waveforms. The waveforms are sinusoidal, phase-shifted by 120 degrees to represent the balanced three-phase nature of the system. These modulation signals ensure that the inverter produces three-phase output voltages with the correct amplitude and phase alignment.

Figure 13 shows the output voltage ($V_{O_{AB}}, V_{O_{BC}}, V_{O_{CA}}$) and output current ($I_{O_A}, I_{O_B}, I_{O_C}$) waveforms of bidirectional three-phase T-type inv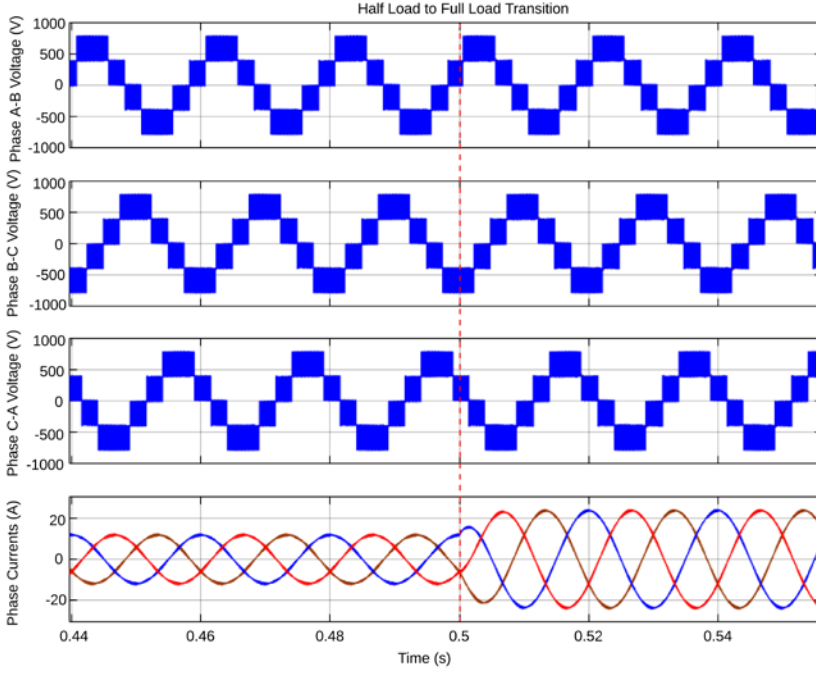erter under half load to full load (grid-to-load) operation. At 0.5 seconds, the load is increased two times and the current is observed to increase at the same rate. Despite this, there is no distortion in the phases of the output voltage waveform.

Figure 13. The Output Voltage ($V_{O_{AB}}, V_{O_{BC}}, V_{O_{CA}}$) and Output Current ($I_{O_A}, I_{O_B}, I_{O_C}$) Waveforms of Bidirectional Three-Phase T-Type Inverter Under Half Load To Full Load (Grid-To-Load) Operation

Figure 14 depicts the output voltage ($V_{O_{AB}}$) and output current (I_o) waveforms of the bidirectional three-phase T-type inverter under h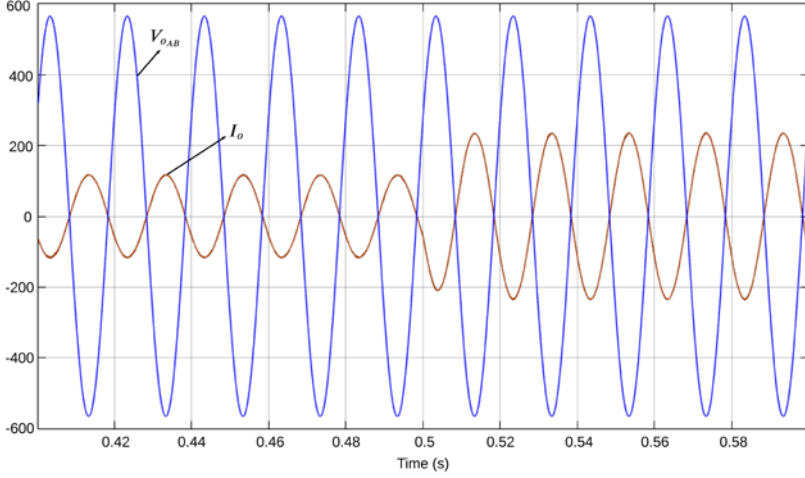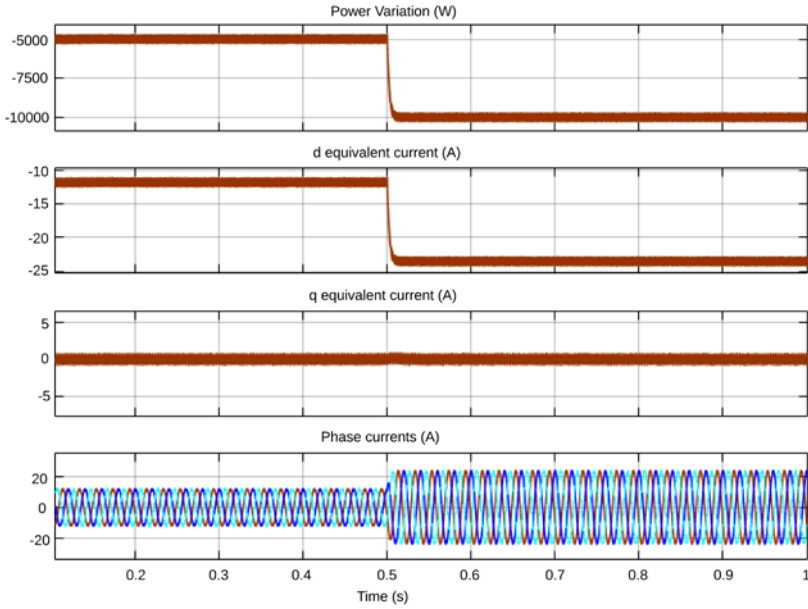alf load (5kW) to full load (10kW) (load-to-grid) operation. At 0.5 seconds, the reference output power is increased two times and the current is observed to increase at the same rate. Also, current and voltage waveforms have an 180^0 phase difference. This means that the inverter transfers energy to the grid.

Figure 14. The Output Voltage ($V_{O_{AB}}$) and Output Current (I_o) Waveforms of the Bidirectional Three-Phase T-Type Inverter Under Half Load To Full Load (Load-To-Grid Operation)

Figure 15. The Output Active Power (P_o), dq-Axis Currents (I_d, I_q) and Phase Current ($I_{O_A}, I_{O_B}, I_{O_C}$) Waveforms of the Bidirectional Three-Phase T-Type Inverter

Finally, figure 15 shows the output active power (P_o), dq-axis currents (I_d, I_q) and phase current ($I_{O_A}, I_{O_B}, I_{O_C}$) waveforms of the bidirectional three-phase T-type inverter. At 0.5 seconds, the reference output power is increased two times (5kW to 10kW) and the phase current is observed to increase at the same rate as shown in figure. Besides dq-axis forms of the phase currents are shown in the figure. During the step change, d-axis current of the inverter is increased two times as negative output, while q-axis keeps constant due to the reference reactive power component is set to zero.

5. CONCLUSION

In this paper, design and analysis of a bidirectional three-phase T-type inverter is presented. The T-type inverter provides a significant improvement over conventional two-level inverters by reducing THD, lowering switching losses, and enhancing voltage stress distribution across semiconductor devices. These features make the T-type inverter particularly suitable for medium and high power applications.

Simulation results show that the three-phase T-type inverter offers a compelling balance between performance and complexity. The ability to generate three voltage levels improves power quality and reduces the need for large passive filters. The use of PWM modulation method highlights the versatility of this topology. These technique ensure efficient control of switching states and maintain voltage balance across the DC-link capacitors. In conclusion, the three-phase T-type inverter stands out as an effective solution for modern power electronics implementations that demand high efficiency, reliability, and power quality.

REFERENCES

Abu-Rub, H., Holtz, J., Rodriguez, J., & Baoming, G. (2010). Medium-voltage multilevel converters State of the art, challenges, and requirements in Industrial applications. *IEEE Transactions on Industrial Electronics*, 57(8), 2581–2596. Retrieved 20 September 2024 from https://doi.org/10.1109/TIE.2010.2043039

Alnamer, S. S., Mekhilef, S., & Mokhlis, H. Bin. (2018). A Four-Level T-Type Neutral Point Piloted Inverter for Solar Energy Applications. *Energies 2018, Vol. 11, Page 1546*, 11(6), 1546. Retrieved 20 September 2024 from https://doi.org/10.3390/EN11061546

Baimel, D., Barbie, E., Bronshtein, S., Sitbon, M., Aharon, I., & Kuperman, A. (2023). High power T-type-based multi-level inverter for electric vehicles. *Energy Reports*, 9, 220–225. Retrieved 20 September 2024 from https://doi.org/10.1016/J.EGYR.2023.09.181

Chen, T., & Narimani, M. (2019). Soft-switching t-type multilevel inverter. *Journal of Power Electronics*, 19(5), 1182–1192. Retrieved 20 September 2024 from https://doi.org/10.6113/JPE.2019.19.5.1182

Cui, D., & Ge, Q. (2018). A Novel Hybrid Voltage Balance Method for Five-Level Diode-Clamped Converters. *IEEE Transactions on Industrial Electronics*, 65(8), 6020–6031. Retrieved 20 September 2024 from https://doi.org/10.1109/TIE.2017.2784399

De Almeida Cacau, R. G., Torrico-Bascopé, R. P., Neto, J. A. F., & Torrico-Bascopé, G. V. (2014). Five-Level T-type inverter based on multistate switching cell. *IEEE Transactions on Industry Applications*, 50(6), 3857–

3866. Retrieved 20 September 2024 from https://doi.org/10.1109/TIA.2014.2311508

Do, D. T., Nguyen, M. K., Quach, T. H., Tran, V. T., Blaabjerg, F., & Vilathgamuwa, D. M. (2020). A PWM Scheme for a Fault-Tolerant Three-Level Quasi-Switched Boost T-Type Inverter. *IEEE Journal of Emerging and Selected Topics in Power Electronics*, 8(3), 3029–3040. Retrieved 20 September 2024 from https://doi.org/10.1109/JESTPE.2019.2922687

Franquelo, L. G., Rodriguez, J., Leon, J. I., Kouro, S., Portillo, R., & Prats, M. A. M. (2008). The age of multilevel converters arrives. *IEEE Industrial Electronics Magazine*, 2(2), 28–39. Retrieved 20 September 2024 from https://doi.org/10.1109/MIE.2008.923519

Gurpinar, E., & Castellazzi, A. (2016). Single-Phase T-Type Inverter Performance Benchmark Using Si IGBTs, SiC MOSFETs, and GaN HEMTs. *IEEE Transactions on Power Electronics*, 31(10), 7148–7160. Retrieved 20 September 2024 from https://doi.org/10.1109/TPEL.2015.2506400

He, L., & Cheng, C. (2016). A Flying-Capacitor-Clamped Five-Level Inverter Based on Bridge Modular Switched-Capacitor Topology. *IEEE Transactions on Industrial Electronics*, 63(12), 7814–7822. Retrieved 20 September 2024 from https://doi.org/10.1109/TIE.2016.2607155

Huynh, A. T., Ho, A. V., & Chun, T. W. (2020). Three-Phase Embedded Modified-Z-Source Three-Level T-Type Inverters. *IEEE Access*, 8, 130740–130750. Retrieved 20 September 2024 from https://doi.org/10.1109/ACCESS.2020.3009720

Maheswari, K. T., Bharanikumar, R., Arjun, V., Amrish, R., & Bhuvanesh, M. (2021). A comprehensive review on cascaded H-bridge multilevel inverter for medium voltage high power applications. *Materials Today: Proceedings*, 45, 2666–2670. Retrieved 20 September 2024 from https://doi.org/10.1016/J.MATPR.2020.11.519

Nabae, A., Takahashi, I., & Akagi, H. (1981). A New Neutral-Point-Clamped PWM Inverter. *IEEE Transactions on Industry Applications*, IA-17(5), 518–523. Retrieved 20 September 2024 from https://doi.org/10.1109/TIA.1981.4503992

Ngo, V. Q. B., Nguyen, M. K., Tran, T. T., Lim, Y. C., & Choi, J. H. (2018). A Simplified Model Predictive Control for T-Type Inverter with Output LC Filter. *Energies 2019, Vol. 12, Page 31*, 12(1), 31. Retrieved 20 September 2024 from https://doi.org/10.3390/EN12010031

Roy, P., & Banerjee, A. (2024). A study on performance parameters of three-level T-type inverter based PMSM drives for electric vehicles applications. *Electrical Engineering*, 106(2), 1121–1134. Retrieved 20 September 2024 from https://doi.org/10.1007/S00202-023-01779-6/FIGURES/18

Schweizer, M., & Kolar, J. W. (2013). Design and implementation of a highly efficient three-level T-type converter for low-voltage applications. *IEEE Transactions on Power Electronics*, 28(2), 899–907. Retrieved 20 September 2024 from https://doi.org/10.1109/TPEL.2012.2203151

PIEZOELECTRIC ENERGY HARVESTING APPLICATION IN WEAVING LOOM MACHINE SYSTEMS

Onur Mahmut PİŞİRİR[1]

Mehmet ERTUĞRUL[2]

Selahattin PAZARCI[3]

Okan BİNGÖL[4]

1. INTRODUCTION

Electric energy needed today is obtained as a result of the conversion of kinetic energy through alternators in wind, hydroelectric, thermal, and nuclear power plants, in addition to solar power plants (IEA, 2023). Renewable energy sources and energy-saving practices are gaining more and more importance due to the risk of depletion of fossil fuels, the primary energy source of traditional thermal power plants based on non-renewable energy sources, which are widely used in electricity generation, and environmental damages (Energy Institute, 2024).

In recent years, annual electricity generation in Turkey has amounted to 328 billion kWh, compared to 29,239 TWh worldwide. By 2050, global generation is expected to reach

---

[1] Öğr. Gör. Dr., Süleyman Demirel University, Distance Education Application and Research Center, onurpisirir@sdu.edu.tr, ORCID: 0000-0001-6895-3420.

[2] Isparta University of Applied Sciences, Faculty of Technology, l1722705050@isparta.edu.tr, ORCID: 0009-0009-4799-6056.

[3] Isparta University of Applied Sciences, Faculty of Technology, l1922705054@isparta.edu.tr, ORCID: 0009-0000-8756-5992.

[4] Prof. Dr., Isparta University of Applied Sciences, Faculty of Technology, okanbingol@isparta.edu.tr, ORCID: 0000-0001-9817-7266.

42,298 TWh, while in Turkey, it is expected to reach 450,754 GWh by 2032 (EÜAŞ, 2023; TEİAŞ, 2023). In Turkey, 42.6% of electricity consumption is in the industrial sector, while the rest is in the commercial, residential, agricultural, and transportation sectors (TEDAŞ, 2024). Thermal power plants account for 57.75% of the energy generation, and they mostly use natural gas and coal (EPDK, 2024; TPAO, 2023). Coal accounts for 27% of Turkey's primary energy consumption sources, and thermal power plants are monitored with RADISA stations due to their radioactive content (NDK, 2023).

Fossil fuels, which cause environmental problems such as climate change by increasing the amount of greenhouse gases in the atmosphere with high carbon dioxide emissions, are also rapidly depleting in the face of growing energy demand due to their non-renewable nature (Ghosh and Ghosh, 2020). Therefore, renewable energy sources with a lower carbon footprint, such as solar, wind, geothermal, hydropower, and biomass, replace fossil fuels (Sayed et al., 2023).

Energy harvesting is the process of converting various types of energy present in the environment into electrical energy. Piezoelectric energy harvesting (PEH) is one of the electromagnetic, electrostatic, and piezoelectric methods used to extract electrical energy from vibrational energy present in the environment (Erturk and Inman, 2011). Piezoelectric transducers can be made of different materials and have a wide range of applications (Sezer and Koç, 2021). This new technology is considered a self-powered solution for low energy-consuming systems such as wireless and microelectronic devices that do not require charging or battery replacement (Kim et al., 2011). Energy harvesting is also used in industrial applications (Díez et al., 2019). In addition to reducing production costs, such practices contribute to sustainable energy solutions (Maamer et al., 2019).

The idle energy generated in industrial production lines can be converted into electrical energy with various types of harvesting (White and Zaghari, 2022). Sustainable renewable energy source solution that allows for reducing the environmental impact of industrial production lines and saving energy in production also provides proactive maintenance by enabling monitoring of vibration and pressure parameters in case of malfunctions that may occur in the lines (Gücüyener, 2018). Energy harvesting systems are being developed for industrial applications. Energy harvesting systems are evaluated in industrial applications (Hada, Janak, and Smilek, 2018). Piezoelectric energy harvesting systems are also being evaluated for different industrial applications (Aabid et al., 2021). One of the industrial production lines where the piezoelectric transducer energy harvesting solution can be applied is the looms of textile mills (Saravanan and Albert, 2023).

This study aims to convert the inert kinetic energy generated by the electric motor on the loom into electrical energy to provide energy to the lighting system of the loom by using piezoelectric transducers as a renewable energy source. Within the scope of the experimental study, the oscillating kinetic energy generated by the AA motor on the loom was converted into electrical energy at a voltage value of approximately 8V using 20 piezoelectric transducers. The voltage value of the electrical energy obtained with the voltage divider circuit and voltage sensor connected to the Arduino Uno Rev3 microcontroller was monitored, and when sufficient voltage was generated, switching between grid electricity and renewable energy source was controlled with a 2-channel relay module.

2. MATERIALS AND METHODS

2.1. Piezoelectric Transducers

Piezoelectric materials with high electromechanical coupling factor and piezoelectric coefficient, shown in Figure 2, stand out with the advantages of providing high output voltage and not requiring an additional power source compared to electrostatic, electromagnetic, and triboelectric energy harvesting mechanisms (Covaci, and Gontean, 2020; Pradeesh et al., 2022). Piezoelectric transducers, which can be used in different application areas with various structures and designs and can be selected according to application requirements, offer higher energy density than electrostatic and electromagnetic methods (Wakshume & Płaczek, 2024). Moreover, piezoelectric and ferroelectric materials have been shown to exhibit piezoelectric and ferroelectric properties that can harvest heat energy as well as vibration and wind energy in low-power power generation and can provide polarity change with external electric field applications (Yuan et al., 2024).

Figure 1. Characteristics of Piezoelectric Materials
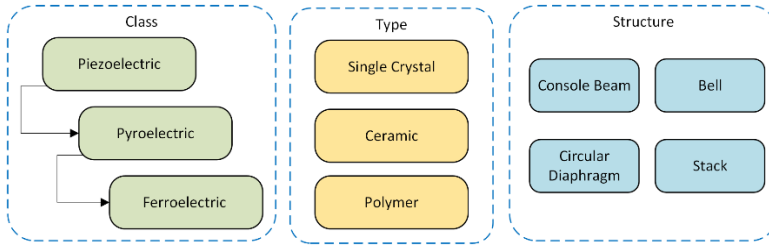
Among the piezoelectric types, the high energy conversion rates of ceramics, the flexibility of polymers, and both the high energy conversion rates and flexibility of composites stand out (Li and Lee, 2022). Apart from the existing species, there are also studies with meta-materials (Lee et al., 2022). Piezoelectric material production studies are ongoing with different methods, such as additive manufacturing (Chen et al.,

2020). Table 1 shows piezoelectric energy harvesting applications of different types and structures.

Table 1. Piezoelectric Energy Harvesting Fields of Application

Reference	Fields of Application
(Panda, et al., 2022)	Biomedical
(Sharma, et al., 2022)	Tile flooring
(Wu, Bao, and Wang., 2021)	Rain
(Zheng, et al., 2023)	Wind
(Zhang, et al.)	Bearing
(Liu, et al., 2021)	Wearable Technologies
(Chen, et al., 2021)	Highway
(Kargar, Masoud, and Hao., 2022)	Ocean
(Sekhar, et al., 2021)	Building

The piezoelectric and inverse piezoelectric effect is given in Eq.1 and Eq.2 (Kamel, 2022). The dielectric coefficient in these equations can be written in units of C/N with the symbol d or in units of Cm^{-2}, VmN^{-1} and Vm^{-1} with the symbols e, g, and h, respectively (Smith and Kar-Narayan, 2022).

$$D = dT + \varepsilon E \tag{1}$$

$$S = sT + dE \tag{2}$$

Source and load impedance must be equalized to maintain efficient energy conversion (Liang and Liao, 2011). In addition to the bridge diode topology, voltage doubler, and nonlinear switching rectifier circuits can also be used in the rectification stage to reduce energy dissipation (Çiftci et al., 2021). Power optimization in energy harvesting is achieved with AA-DA converters such as SEH, SSHI, SECE, SMBF, S3HI, and H-S3HI and MPPT circuits such as Hill-climbing, FOCV and P&Q (Li et al., 2022).

2.2. Weaving Looms

Weaving machines were developed from looms to weave large and complex patterns (Kovačević and Schwarz, 2015). Today, looms are classified according to weft insertion and

shedding systems and the product produced (Derstekstil, 2015). Electric looms generate high vibration and energy during the production process (Badkar and Benal, 2021). This energy can be converted into electrical energy by piezoelectric transducers (Saravanan and Albert, 2024).

2.3. Prototype Product

The prototype product uses an AA electric motor to convert electrical energy into circular motion, which is then transferred to the loom as linear motion. The mechanical energy that cannot be used is converted into electrical energy to power the loom lighting system using piezoelectric transducers placed under the loom. The required voltage and current values for the system are provided by the connections of the transducers in series and parallel, respectively. Sensors monitor the voltage, current, and power consumption, and when the required voltage value is reached, the microcontroller decides to switch the system supply.

2.3.1. Mechanical Design

The prototype product includes mechanical and electromechanical components such as the AA electric motor, powertrain, spring-loaded bench, and piezoelectric transducers, as illustrated in Figure 3. The AA electric motor is connected to the piezoelectric transducers through the powertrain and the spring-loaded bench.

Figure 3. Model of Prototype Product
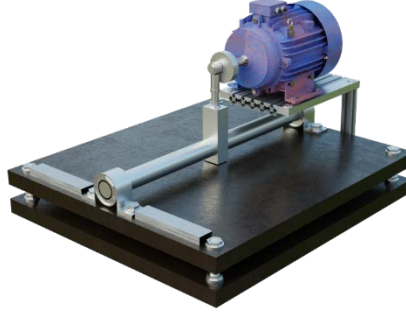
Figure 4(a) shows the prototype product. Among the electromechanical components of the product, the AA electric motor provides the conversion of electrical energy into circular mechanical energy. With the powertrain, the kinetic energy in the form of circular motion is converted into kinetic energy in the form of linear motion, the kinetic energy in the form of oscillating linear motion is transferred to the piezoelectric transducers with the spring-loaded bench organ, and the kinetic (mechanical) energy in the form of oscillating linear motion is converted into electrical energy with the piezoelectric transducers. The interactions between the mechanical components whose tasks are described are explained in the mechanical system flow chart in Figure 4(b). In the process described in the diagram, mechanical energy is converted into electrical energy via transducers to be used in the supply of the lighting system.

Figure 4. (a) Electromechanical and Mechanical Components of the Prototype Product, (b) System Flowchart

(a)

Electrical energy is converted into circular motion by the motor.	The motion oscillation is converted into mechanical strain energy on piezoelectric transducers located between the bench.	Mechanical tension energy is converted into electrical energy by transducers.
The circular motion is converted into linear motion by the power transmission organs and transferred to the loom.	With the transferred movement, the machine performs a controlled oscillation with an average value of 20 Hz with the help of springs.	

(b)

2.3.2. Electrical Design

The lighting system of the prototype product operates at a nominal voltage of 12 V and a current of 250 mA. These values are provided by the adapter during the supply of the system from the grid, while during the supply from the renewable energy source, they are provided by series and parallel connection topologies, rectifiers, and filter circuits, as shown in the diagram in Figure 5. It is also shown in the figure that the supply transition between the grid and the transducer is provided by the microcontroller through electromagnetic relays depending on the voltage value condition read through the voltage divider circuit. The feeding status can be monitored with the LCD screen.

Figure 5. Electronic Circuit Schematic of the Prototype Product
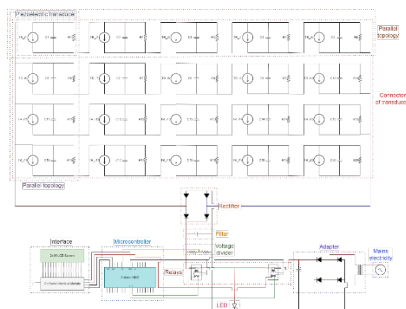
The one piezoelectric transducer in the prototype product, shown in the diagram in Figure 6(a), can convert energy at an average open circuit voltage of 20 V RMS and short circuit current of 160 µA at nominal operating frequency as shown in the output in Figure 6(b). The voltage-time characteristic of the equivalent circuit of the piezoelectric transducer can also be observed in the same output graph.

**Figure 6. (a) Piezoelectric Transducer Demonstration, (b) Voltage-Time Plot**

(a)   (b)
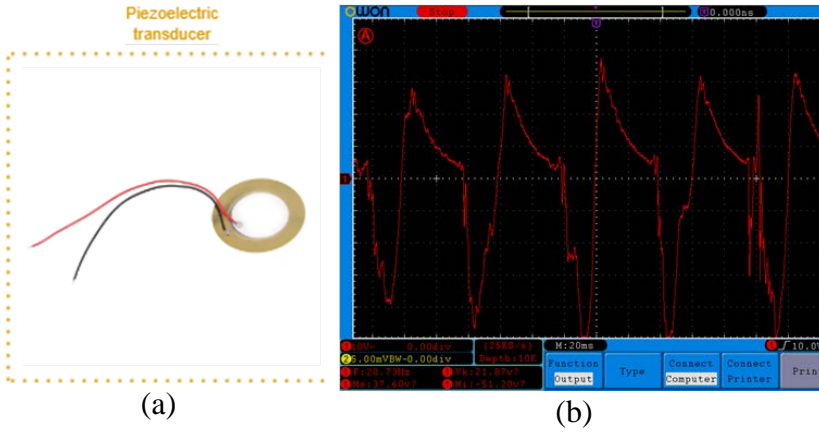
To sustainably meet the voltage and current values required for the supply of the lighting system, an average open circuit voltage value of 110 V RMS was obtained by connecting five piezoelectric transducers in series connection topology as shown in the diagram in Figure 7(a) and an average short circuit current value of 500 uA was obtained by connecting five series connected piezoelectric transducer groups in parallel connection topology as shown in Figure 7(b).

Figure 7. (a) Piezoelectric Transducer Series Connection, (b) Parallel Connection

(a)

(b)
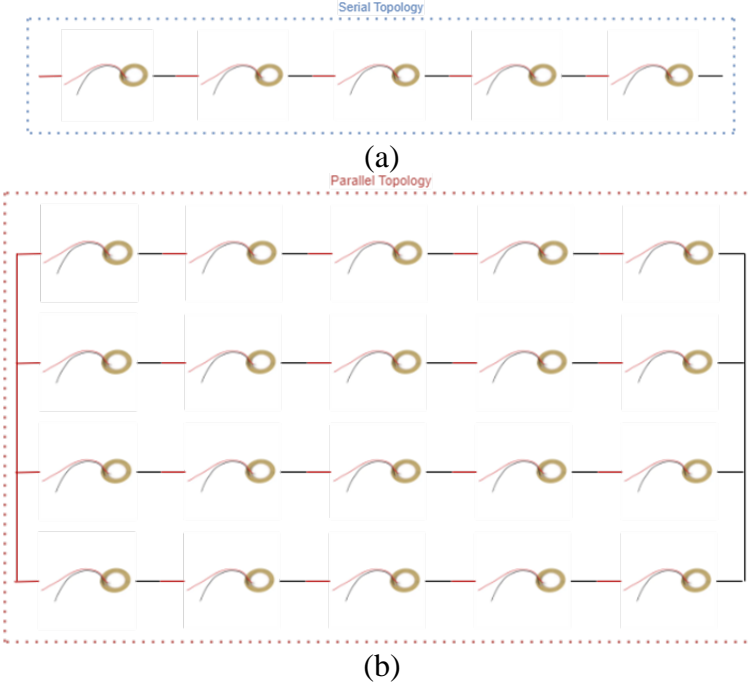
To obtain direct current, it was observed that 50 V open circuit and 325 uA short circuit direct current values were obtained when a capacitor-filtered full wave rectifier blind diode circuit was connected to the output of the transducer system with 110 V RMS and 500 uA values. After obtaining the nominal voltage and current values required for the supply of the lighting system, as shown in the diagram in Figure 8, the supply transition between the transducer and the mains is realized by controlling the relay elements and the microcontroller. When the transducer reaches the voltage value, the grid is first deactivated, and then the transducer system is activated, while when the voltage drops below the value, the grid is activated after the transducer is deactivated. The activated system and the piezoelectric voltage can be monitored.

Figure 8. Transition Connection Between Mains and Transducer
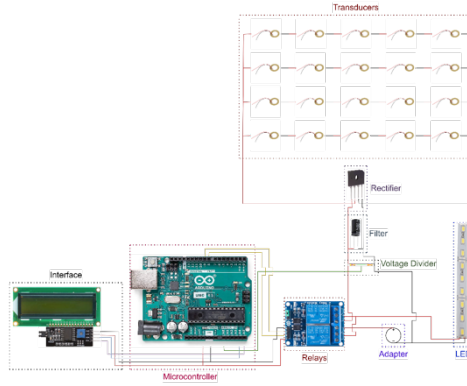
As shown in the diagram in Figure 9, energy conversion, obtaining supply voltage, current, and waveform values, monitoring the voltage value obtained, and switching between supply sources are provided with the electronic hardware whose design is described above.

Figure 9. Flowchart of Electronic Hardware
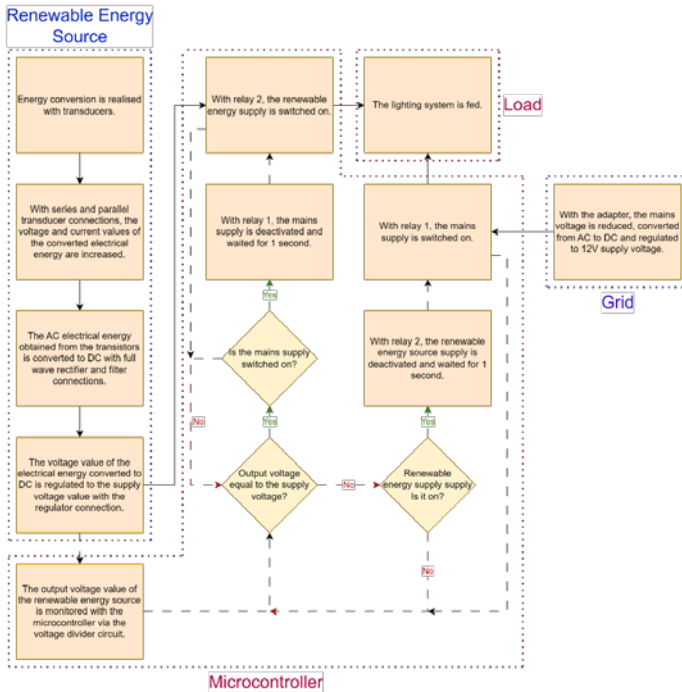
The microcontroller controls the grid and transducer relays by comparing the voltage value of the electrical energy converted by the renewable energy source being monitored with the control voltage value. The control voltage is a 5 V step signal representing the nominal supply voltage of the lighting system, the voltage monitored by the voltage divider circuit is the voltage of the electrical energy converted by the transducers, the microcontroller is Arduino UNO, and the grid and transducer switches are 2-channel electromagnetic relays. According to the output values of the control system (1 or 0), the lighting system is powered by either the grid or a renewable energy source.

In the software of the microcontroller, first, analog input pins for reading the signal from the voltage divider circuit, output pins for controlling the mains and source relays, resistor values for converting the voltage divider circuit value into voltage value, a variable for storing the defined voltage value and variables for determining the initial states of the relays are defined. Then, if the source voltage is equal to the supply voltage value, the supply is realized through the renewable energy source. Otherwise, it is realized through the grid. In the transitions between sources, the source that is activated is controlled and deactivated before the other source is activated, and a 1-second wait is realized.

The flowchart of the microcontroller software is shown in the diagram in Figure 10. The diagram shows the closed loop in which pins, values, and variables are defined, the operating modes of the defined pins are determined, conditions are checked, and relays are triggered depending on the controlled conditions.

Figure 10. Software Flowchart
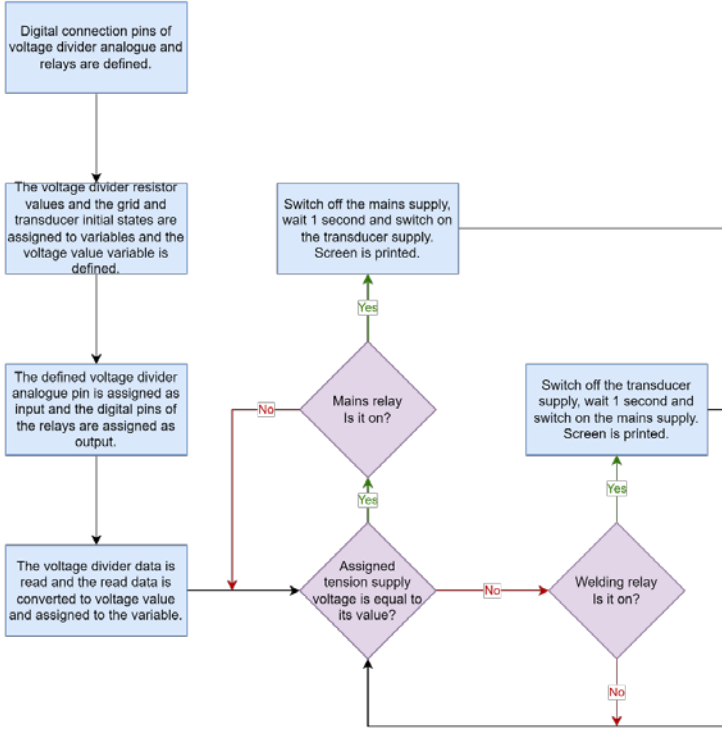
3. RESULTS AND DISCUSSION

In the prototype product, transducers that provide piezoelectric energy conversion, which is preferred among mechanical energy harvesting methods, were used. It is measured with a multimeter that 20 V RMS open circuit voltage and 160 uA short circuit current can be obtained with one of the piezoelectric class transducers in ceramic structure and button type. With the conversion of these values, only 1 5 mm red LED, which can operate at 5 V and 20 mA, can be made to blink during vibration. To increase the power, 5 of the transducers are connected in series, and 4 of the groups connected in series of 5 are connected in parallel. With the realized connection, it is

measured that 110 V RMS open circuit voltage and 500 uA short circuit current values are reached. A blunt diode and filter capacitor were used to convert the electrical energy generated in the form of AA waves by the transducers into DA. It is measured that the DA output drops to 50 V open circuit voltage and 325 uA short circuit current. Operating at 12 V and 250 mA nominal values, it is measured that the lighting system can be supplied with approximately 8 V with the energy source under load. The lighting system operates at a lower brightness compared to the mains supply.

The connected transducers were positioned in the system, as shown in Figure 11. In the system, motion energy is generated as 915 1/mm circular motion with a 1.1 kW AA motor. The generated circular motion energy is converted into linear motion by the powertrain. The converted linear motion energy is transmitted to the positioned piezoelectric transducers with a spring bench. Foam and silicon are used to optimize the mechanical power transfer between the benches and transducers and to increase the strain and shape change. The output of the transducers, which converts the transmitted mechanical energy into electrical energy, is connected to the load.

Figure 11. Positioning of Transducers in the System

In the feeding of the electrical load consisting of the lighting system, the transition control between the mains and the source is provided by a 2-channel 12V relay module. The

triggering of the module is controlled by the Arduino UNO microcontroller board via digital input and output pins. Triggers are realized when the source voltage reaches the supply voltage and drops below the supply voltage. The source voltage is measured by a voltage divider circuit consisting of 47 kΩ and 33 kΩ resistors, which operates at 150 µA by reducing 12 V to approximately 5 V with an error of 50 mV. The measured value is monitored via the microcontroller analog input. The source activated in the appropriate voltage range is printed on the screen, as shown in Figure 12(a) and Figure 12(b).

Figure 12. (a) Lighting Mains Supply, (b) Supply With Piezoelectric Energy Harvesting

(a)   (b)

In the field of energy-saving solutions with renewable energy sources in industrial production lines, the prototype of the product shown in Figure 13 was realized on the industrial production line of weaving loom and energy saving in lighting systems with piezoelectric renewable energy source.

Figure 13. Operating Prototype
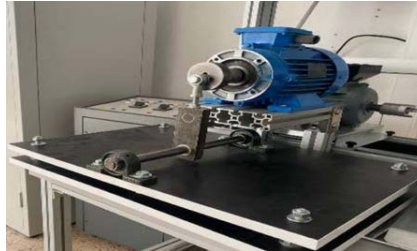
4. CONCLUSION

In this study, a prototype has been developed to convert the inert kinetic energy produced by the electric motors of weaving looms in textile factories into electrical energy by piezoelectric transducers to feed lighting systems. The system utilizes piezoelectric mechanical energy harvesting to improve energy efficiency and reduce fossil fuel use. The results demonstrated the potential of renewable energy sources to save energy in industrial applications. Furthermore, this approach contributes to the minimization of carbon footprint and environmental sustainability. It is envisaged that the developed prototype can be extended to contribute to energy savings in industrial applications other than looms.

5. ACKNOWLEDGMENT

REFERENCES

Aabid, A., Raheman, M. A., Ibrahim, Y. E., Anjum, A., Hrairi, M., Parveez, B., ... & Mohammed Zayan, J. "A systematic review of piezoelectric materials and energy harvesters for industrial applications." Sensors 21.12 (2021): 4145.

Badkar, P. S., & Benal, M. M. "Vibration analysis of the power loom." Materials Today: Proceedings 42 (2021): 1382-1386.

Chen, C., Wang, X., Wang, Y., Yang, D., Yao, F., Zhang, W., ... & Hu, D. "Additive manufacturing of piezoelectric materials." Advanced Functional Materials 30.52 (2020): 2005141.

Chen, C., Xu, T. B., Yazdani, A., & Sun, J. Q. "A high density piezoelectric energy harvesting device from highway traffic—System design and road test." Applied Energy 299 (2021): 117331.

Çiftci, B., Chamanian, S., Koyuncuoğlu, A., Muhtaroğlu, A., & Külah, H. "A low-profile autonomous interface circuit for piezoelectric micro-power generators." IEEE Transactions on Circuits and Systems I: Regular Papers 68.4 (2021): 1458-1471.

Covaci, C., and Gontean, A. "Piezoelectric energy harvesting solutions: A review." Sensors 20.12 (2020): 3512.

Derstekstil, "Dokuma Makinelerinin Sınıflandırılması", URL: https://www.derstekstil.name.tr/dokuma-makinelerinin-s%C4%B1n%C4%B1fland%C4%B1r%C4%B1lmas%C4%B1.html, (Erişim Tarihi: 08.08.2024).

Díez, P. L., Gabilondo, I., Alarcón, E., & Moll, F. "Mechanical energy harvesting taxonomy for industrial environments: Application to the railway industry." *IEEE Transactions*

on Intelligent Transportation Systems 21.7 (2019): 2696-2706.

Energy Institute, "Statistical Review of World Energy", 73rd edition, 2024, URL: https://www.energyinst.org/__data/assets/pdf_file/0006/1542714/EI_Stats_Review_2024.pdf, (Erişim Tarihi: 08.08.2024).

EPDK, "Elektrik Piyasası 2023 Yılı Piyasa Gelişim Raporu", 2024, URL: https://www.epdk.gov.tr/Detay/DownloadDocument?id=fx+hB3E2Cns=, (Erişim Tarihi: 08.08.2024).

Erturk, A., & Inman, D. J. "Piezoelectric energy harvesting." John Wiley & Sons, 2011.

EÜAŞ, "Elektrik Üretimi Ve Ticareti Sektör Raporu 2023", 2023, URL: https://webim.euas.gov.tr/file/6f28096f-c481-40d8-9662-440e0054f7ef?download, (Erişim Tarihi: 08.08.2024).

Ghosh, S. K., & Ghosh, B. K. "Fossil fuel consumption trend and global warming scenario: Energy overview." Glob. J. Eng. Sci 5.2 (2020): 1-6.

Gücüyener, İ. "Machine vibration measurement with high resolution designed tracking software." International Journal of Humanities and Arts Studies ANNEX 1 (2018): 20-25.

Hadas, Z., Janak, L., & Smilek, J. "Virtual prototypes of energy harvesting systems for industrial applications." Mechanical Systems and Signal Processing 110 (2018): 152-164.

IEA, "Electricity Market Report 2023", 2023, URL: https://iea.blob.core.windows.net/assets/255e9cba-da84-4681-8c1f-

458ca1a3d9ca/ElectricityMarketReport2023.pdf, (Erişim Tarihi: 08.08.2024).

Kamel, N. A. "Bio-piezoelectricity: fundamentals and applications in tissue engineering and regenerative medicine." Biophysical Reviews 14.3 (2022): 717-733.

Kargar, S. M., & Hao, G. "An atlas of piezoelectric energy harvesters in oceanic applications." Sensors 22.5 (2022): 1949.

Kim, H. S., Kim, J. H., & Kim, J. "A review of piezoelectric energy harvesting based on vibration." International journal of precision engineering and manufacturing 12 (2011): 1129-1141.

Kovačević, S., & Schwarz, I. "Weaving complex patterns-from weaving looms to weaving machines." Cutting Edge Research in Technologies. England: In Tech (2015): 93-111.

Lee, G., Lee, D., Park, J., Jang, Y., Kim, M., & Rho, J. "Piezoelectric energy harvesting using mechanical metamaterials and phononic crystals." Communications Physics 5.1 (2022): 94.

Li, D., Wang, C., Cui, X., Chen, D., Fei, C., & Yang, Y. "Recent progress and development of interface integrated circuits for piezoelectric energy harvesting." Nano Energy 94 (2022): 106938.

Li, T., & Lee, P. S. "Piezoelectric energy harvesting technology: from materials, structures, to applications." Small Structures 3.3 (2022): 2100128.

Liang, J., & Liao, W. H.. "Impedance modeling and analysis for piezoelectric energy harvesting systems." IEEE/ASME transactions on mechatronics 17.6 (2011): 1145-1157.

Liu, Y., Khanbareh, H., Halim, M. A., Feeney, A., Zhang, X., Heidari, H., & Ghannam, R. "Piezoelectric energy harvesting for self-powered wearable upper limb applications." Nano Select 2.8 (2021): 1459-1479.

Maamer, B., Boughamoura, A., El-Bab, A. M. F., Francis, L. A., & Tounsi, F. "A review on design improvements and techniques for mechanical energy harvesting using piezoelectric and electromagnetic schemes." Energy Conversion and Management 199 (2019): 111973.

NDK, "2023 Yılı Faaliyet Raporu", 2023, URL: https://webim.ndk.gov.tr/file/1fd8dceb-7c39-4622-9ecf-0db2d384b7d4, (Erişim Tarihi: 08.08.2024).

Panda, S., Hajra, S., Mistewicz, K., In-na, P., Sahu, M., Rajaitha, P. M., & Kim, H. J. "Piezoelectric energy harvesting systems for biomedical applications." Nano Energy 100 (2022): 107514.

Pradeesh, E. L., Udhayakumar, S., Vasundhara, M. G., & Kalavathi, G. K. "A review on piezoelectric energy harvesting." Microsystem Technologies 28.8 (2022): 1797-1830.

Saravanan, K., & Albert, J. R. "Enhancing energy efficiency in power looms: utilizing regression machine learning for electrokinetic energy assessment." *The Journal of The Textile Institute* (2024): 1-26.

Saravanan, K., & Albert, J. R. "Optimizing energy utilization in the weaving industry: Advanced electrokinetic solutions with modified Piezo Matrix and Super Lift Luo converter." Electric Power Components and Systems (2023): 1-27.

Sayed, E. T., Olabi, A. G., Alami, A. H., Radwan, A., Mdallal, A., Rezk, A., & Abdelkareem, M. A. "Renewable energy and energy storage systems." Energies 16.3 (2023): 1415.

Sekhar, B. C., Dhanalakshmi, B., Rao, B. S., Ramesh, S., Prasad, K. V., Rao, P. S., & Rao, B. P. "Piezoelectricity and its applications." Multifunct. Ferroelectr. Mater 71.1 (2021).

Sezer, N., & Koç, M. "A comprehensive review on the state-of-the-art of piezoelectric energy harvesting." Nano energy 80 (2021): 105567.

Sharma, S., Kiran, R., Azad, P., & Vaish, R. "A review of piezoelectric energy harvesting tiles: Available designs and future perspective." Energy Conversion and Management 254 (2022): 115272.

Smith, M., & Kar-Narayan, S. "Piezoelectric polymers: theory, challenges and opportunities." International Materials Reviews 67.1 (2022): 65-88.

TEDAŞ, "2023 Yılı Türkiye Elektrik Dağıtımı Sektör Raporu", 2024, URL: https://www.tedas.gov.tr/FileUpload/MediaFolder/25819 eac-d024-4308-891a-d248db8c1e0a.pdf, (Erişim Tarihi: 08.08.2024).

TEİAŞ, "10 Yıllık Talep Tahminleri Raporu (2023-2032)", 2023, URL: https://webim.teias.gov.tr/file/f09f9857-4844-42b0-a0fa-74cdacfe4013?download, (Erişim Tarihi: 08.08.2024).

TKİ, "Kömür Sektör Raporu 2022", URL: https://webim.tki.gov.tr/file/1da785ad-141f-42a1-9c4c-c83914a1664d?downloadi, (Erişim Tarihi: 08.08.2024).

TPAO, "2023 Petrol ve Doğal Gaz Sektör Raporu", 2023, URL: https://www.tpao.gov.tr/file/2405/tpao-2023-petrol-ve-

dogal-gaz-sektor-raporu-19746659d1d4d2383.pdf,
(Erişim Tarihi: 08.08.2024).

Wakshume, D. G., & Płaczek, M. Ł. "Optimizing Piezoelectric Energy Harvesting from Mechanical Vibration for Electrical Efficiency: A Comprehensive Review." Electronics 13.5 (2024): 987.

White, N. M., & Zaghari, B. "Energy harvesting: an overview of techniques for use within the transport industry." *IEEE Electrical Insulation Magazine* 38.3 (2022): 24-32.

Wu, N., Bao, B., & Wang, Q. "Review on engineering structural designs for efficient piezoelectric energy harvesting to obtain high power output." Engineering Structures 235 (2021): 112068.

Yuan, X., Shi, J., Kang, Y., Dong, J., Pei, Z., & Ji, X. "Piezoelectricity, pyroelectricity, and ferroelectricity in biomaterials and biomedical applications." Advanced Materials 36.3 (2024): 2308726.

Zhang, L., Zhang, F., Qin, Z., Han, Q., Wang, T., & Chu, F. "Piezoelectric energy harvester for rolling bearings with capability of self-powered condition monitoring." Energy 238 (2022): 121770.

Zheng, X., He, L., Wang, S., Liu, X., Liu, R., & Cheng, G. "A review of piezoelectric energy harvesters for harvesting wind energy." Sensors and Actuators A: Physical 352 (2023): 114190.

CLOUD COMPUTING BASED TEMPERATURE CONTROL APPLICATION

Batın DEMİRCAN[1]

1. INTRODUCTION

Over the past decade, there has been a significant evolution in computing paradigms. One of the most prominent paradigms is cloud computing, which facilitates the easy development of internet-based services (Armbrust et al., 2010). Cloud computing technologies, which have advanced in parallel with evolving technology, offer virtually unlimited capacity in terms of data storage and computational power while being based on the sharing of resources.

Moreover, cloud computing has become a crucial enabler for businesses by reducing the costs associated with hardware and software management, as it allows access to scalable and on-demand computing resources. Cloud computing has redefined how organizations approach their computing needs (Kushida, Murray, & Zysman, 2015; Skillfloor, 2023).

A structure often utilized alongside cloud computing is the Internet of Things (IoT) systems. Major service providers in the fields of cloud computing and IoT include companies like Amazon, Google, and Microsoft (Amazon, 2024; Google, 2024a; Microsoft, 2024). Today, applications in which multiple cloud platforms can be utilized together are being implemented to take advantage of cloud computing platforms (Google, 2024b).

---

[1] Lect., Balıkesir University, Balıkesir Vocational School, Department of Electronic and Automation, batindemircan@gmail.com, ORCID: 0000-0002-0765-458X.

In this study, a temperature control system was developed based on cloud computing and IoT. Measurement data obtained from a temperature sensor via a controller board was recorded and used to activate or deactivate a digital output on the Nodemcu controller board. Additionally, the measurement data was transmitted to the cloud computing environment in real time. The digital output controlled by the controller board was activated or deactivated either locally, based on a temperature setpoint input by the user, or remotely, through an interface implemented in the cloud computing environment.

2. ELECTRONIC SYSTEM ARCHITECTURE

In this study, a Nodemcu board was used to provide physical control and to establish a connection with the cloud computing platform. The Nodemcu board is equipped with an integrated ESP8266 module, features a 32-bit RISC architecture processor, and includes 16 GPIO pins. The general appearance of the Nodemcu board is shown in Figure 1 (Components101, 2020).

Figure 1. Nodemcu Esp8266 Board
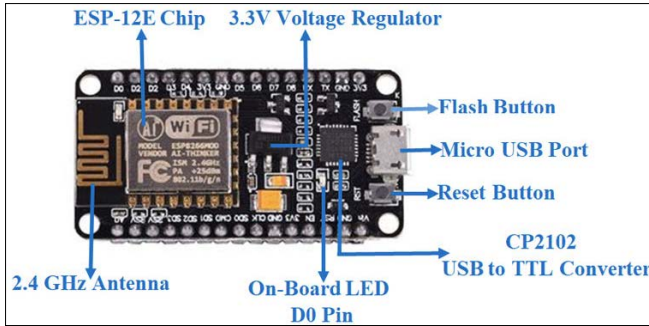
Dht22 sensor was used to measure the ambient temperature. Data from this sensor was initially received by the Nodemcu board and subsequently transmitted to the cloud platform. The Dht22 sensor provides a digital output, operates within a voltage range of 3.3-6V, can measure temperatures in the

range of -40°C to 80°C, and supports measurement intervals as fast as 2 seconds. It is capable of measuring both temperature and humidity (Liu, 2024). The appearance of the Dht22 temperature sensor is shown in Figure 2 (alldatasheet.com, 2024).

Figure 2. Dht22 Sensor
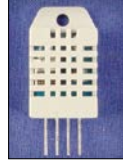
A single-channel relay module was used to control the digital output, both in response to a user-defined temperature setpoint and through direct control by the user via the cloud platform. The schematic diagram illustrating the overall structure of the system is presented in Figure 3.

Figure 3. Structure of System
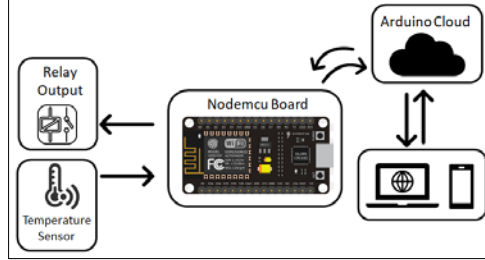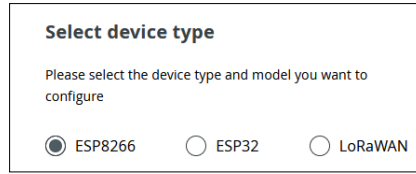
3. CLOUD SYSTEM ARCHITECTURE

For the cloud computing aspect in this study, the Arduino Cloud platform, provided by the Arduino company, was utilized. Arduino Cloud platform supports the use of both Arduino boards and boards from other manufacturers. Depending on the type of membership, users are offered various features with both paid and free usage options. Cloud structure also includes the ability to visualize data using dashboards (Arduino, 2024a).

Since a free membership was used for the platform, the limitations included the use of only 2 "things" simultaneously, a 1-day data storage period, and unlimited dashboards (Arduino, 2024b). First step was to select the appropriate hardware on the cloud computing side. The selection interface for the Nodemcu board is shown in Figure 4.

Figure 4. Device Settings-I

Selecting the device within the cloud platform, the chosen device needs to be assigned a name. The device naming structure is shown in Figure 5.

Figure 5. Device Settings-II
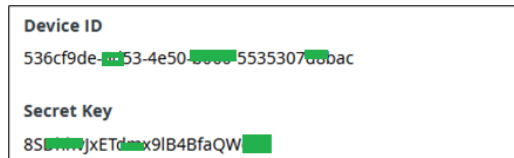
After naming the device, the Arduino Cloud platform automatically generates a "device ID" and a "secret key" for the device. The identification screen on the cloud platform is shown in Figure 6. The information provided on this screen can also be downloaded as a ".pdf" file for future reference.

Figure 6. Device Settings-III

After defining the device on the cloud platform, a "thing" must be created within the cloud structure. The screen used for this definition process is shown in Figure 7.

Figure 7. Thing Settings
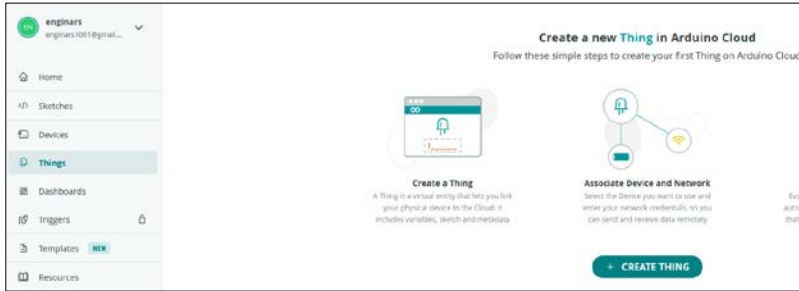
To enable internet access for the Nodemcu board, the "Wi-Fi" settings of the application area must be transferred to the board. The Wi-Fi settings screen is presented in Figure 8.

**Figure 8. Wi-Fi Settings**

An online code editor is opened within the cloud computing platform. Through this online code editor, software can be uploaded to the Nodemcu board, which is connected to the computer via a wired connection. However, to ensure that the Nodemcu board is recognized by the platform, the software named "Arduino Agent" must be executed on the computer. Figure 9 shows the icon of the software minimized in the computer environment.

**Figure 9. Arduino Agent Software Icon**
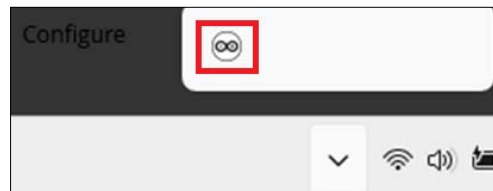
The code editor provided by the cloud platform contains information related to the Nodemcu board, allowing software to be uploaded via a USB connection using the cloud-based code editor. Figure 10 shows the cloud interface, which is configured and ready for the software upload after the initialization process is completed.

Figure 10. Arduino Cloud Program Editor
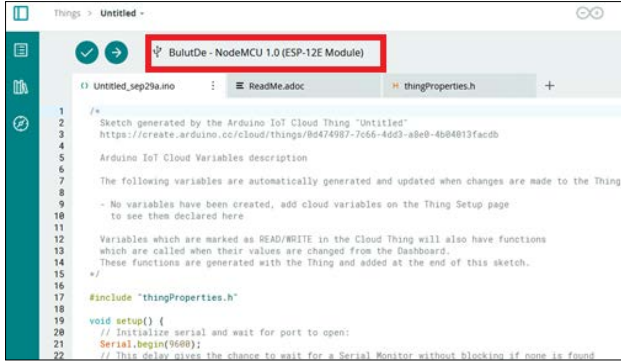
After the compilation process, the code corresponding to the developed program structure was directly sent from the cloud platform to the Nodemcu board via USB connection. Figure 11 illustrates the process of uploading the software to the board.

Figure 11. Wi-Fi Settings
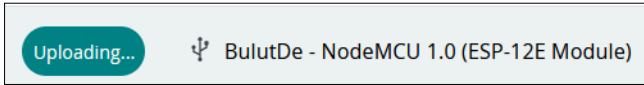
To facilitate data retrieval and transmission to the cloud, it is necessary to define variables within the cloud system. Figure 12 shows the variable definition screen for temperature data in the application implemented on the cloud platform.

Figure 12. Cloud Variable-I

When defining variables, there are options for periodic updates for a specified duration and for updates when the defined variable value changes. Additionally, when defining a variable on the cloud platform, it can be set as either "read-only" or "read/write." The temperature limit information required to activate the output connected to the Nodemcu board when the user-defined setpoint is reached is defined in Figure 14.

Figure 14. Cloud Variable-II
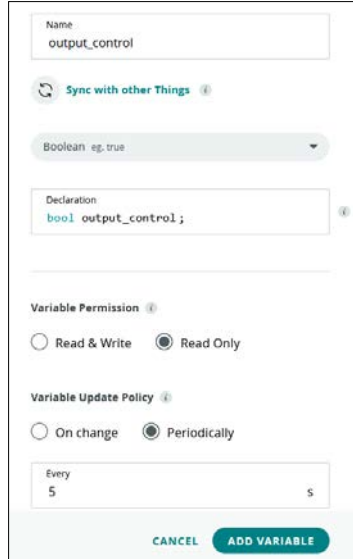
Figure 14 shows the variable definition screen for the output that will be remotely controlled and connected to the relay module in the implemented application.

Figure 14. Cloud Variable-III

After defining the variables and uploading the program to the Nodemcu board, an interface design is necessary to facilitate communication between the user and the physical hardware through the same platform. At this point, a user interface containing the defined variables should be created within the "Dashboard" feature offered by Arduino Cloud. Once the operations on the cloud platform are completed, the application can be executed directly.

Figure 15 shows the connection information for the Nodemcu board, which has been connected to the cloud platform and is running the program. Through this screen available in the cloud, the connection of the Nodemcu board can be activated or deactivated.

Figure 15. Associated Device Screen
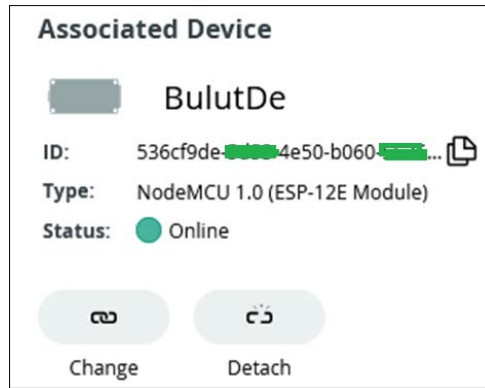
4. EXPERIMENTAL RESULTS

The system implemented in this study is shown in Figure 16. Here, the system is operational; however, the relay output is not activated due to the software structure within the Nodemcu board.

Figure 16. Physical System-I
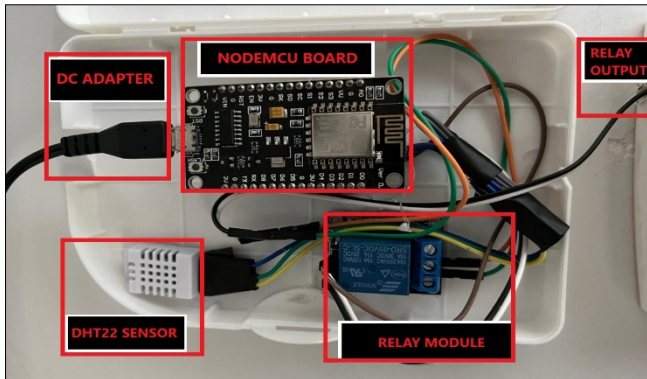
The operational state of the system with the relay output activated is shown in Figure 17. When the relay output is activated, both the LED on the Nodemcu board and the LED on the relay module are illuminated.

Figure 17. Physical System-II
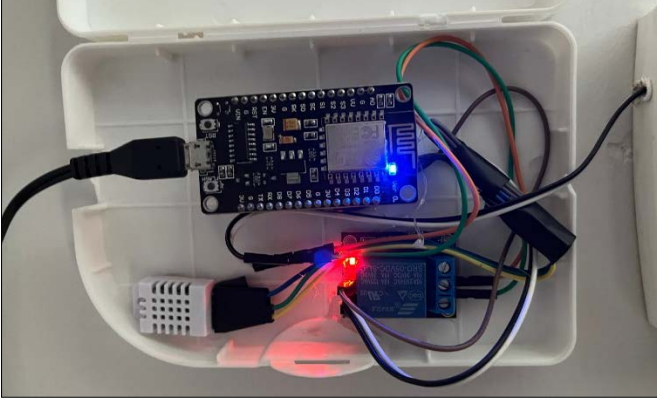
The structure used to activate or deactivate the relay output on the cloud computing side is shown in Figure 18. Here, the user manually controls the output.

Figure 18. Arduino Cloud Output Control (1:output off, 2:output on)
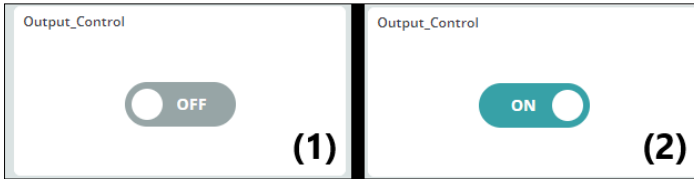
The temperature values obtained from the Dht22 sensor were transmitted in real-time to a cloud platform, where they were recorded. For the measurement day, the minimum temperature was 25.0°C, and the maximum temperature was 30.7°C. The relay control was activated when the set threshold was exceeded, and the output control was also performed independently by the user, regardless of the temperature control. Figure 19 presents the dashboard screen used on the cloud platform.

Figure 19. Arduino Cloud Dashboard
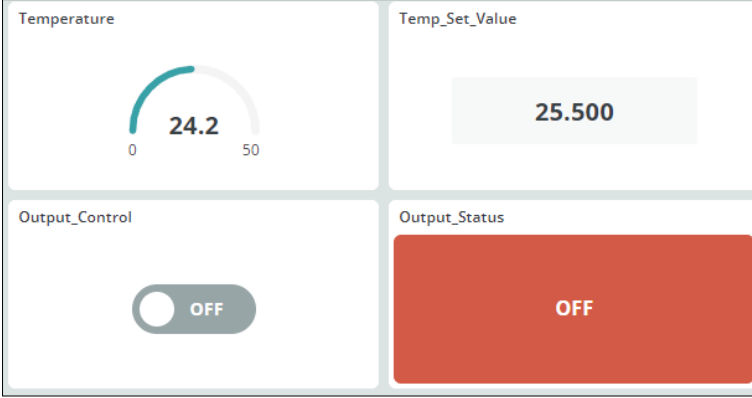
5. CONCLUSIONS

In this study, a temperature measurement and digital output control application was implemented within the rapidly growing field of cloud computing technology, aligned with current technological advancements. The system utilized cloud computing for both data transmission to control the output and data retrieval for recording the measured temperature values. The implementation of the study benefited from the services offered by the Arduino Cloud platform, accessed through a free membership option that allows for only 1-day data storage.

In cases where an increase in the number of devices and data storage duration is necessary, the use of different membership options will be required. Additionally, it was observed that the wireless internet speed in the area where the application was conducted caused some delays in transmitting data to the cloud and in the user's ability to control the output from the cloud side. However, this delay is not considered critical for the implemented system.

REFERENCES

alldatasheet.com. (2024). DHT22. Retrieved October 5, 2024, from https://www.alldatasheet.com/html-pdf/1132459/ETC2/DHT22/109/1/DHT22.html

Amazon. (2024). Amazon Web Services (AWS). Retrieved October 5, 2024, from https://aws.amazon.com/tr/

Arduino. (2024a). Arduino Cloud . Retrieved October 5, 2024, from https://cloud.arduino.cc/

Arduino. (2024b). Arduino Cloud Plans and Benefits. Retrieved October 6, 2024, from https://cloud.arduino.cc/plans/

Armbrust, M., Fox, A., Griffith, R., Joseph, A. D., Katz, R., Konwinski, A., … Zaharia, M. (2010). A view of cloud computing. *Communications of the ACM*, *53*(4), 50–58. https://doi.org/10.1145/1721654.1721672

Components101. (2020). NodeMCU ESP8266 . Retrieved October 5, 2024, from https://components101.com/development-boards/nodemcu-esp8266-pinout-features-and-datasheet

Google. (2024a). Cloud Computing Services | Google Cloud. Retrieved October 5, 2024, from https://cloud.google.com/

Google. (2024b). Google Cloud. Retrieved October 5, 2024, from https://cloud.google.com/multicloud/

Kushida, K. E., Murray, J., & Zysman, J. (2015). Cloud Computing: From Scarcity to Abundance. *Journal of Industry, Competition and Trade*, *15*(1), 5–19. https://doi.org/10.1007/S10842-014-0188-Y/FIGURES/3

Liu, T. (2024). *Digital-output relative humidity & temperature sensor/module DHT22 (DHT22 also named as AM2302)*

Capacitive-type humidity and temperature module/sensor.

Microsoft. (2024). Bulut Bilişim Hizmetleri | Microsoft Azure. Retrieved October 5, 2024, from https://azure.microsoft.com/tr-tr

Skillfloor. (2023). The Impact of Cloud Computing on Data Analytics and Big Data . Retrieved October 5, 2024, from https://skillfloor.medium.com/the-impact-of-cloud-computing-on-data-analytics-and-big-data-888899dead38

DEVELOPMENTS IN THE FIELD OF PIEZOELECTRIC WIND ENERGY HARVESTING (PWEH)

Onur Mahmut PİŞİRİR[1]

Mehmet ERTUĞRUL[2]

1. INTRODUCTION

Electric power consumption proliferates in various sectors such as industry, transportation, housing, trade, utilities, agriculture, forestry, and fisheries. Figure 1(a) shows detailed electric power consumption by sector (IEA, 2021). Electricity is generated from different sources such as coal, natural gas, oil, nuclear power, hydropower, wind, solar, and bioenergy. Figure 1(b) shows the distribution of electricity generation by source (Ritchie and Rosado, 2020). Given the risk of depletion and environmental damage of non-renewable fossil fuels, the trend toward renewable energy sources in electricity generation is increasing (Molla, Farrok, and Alam, 2024).

[1] Öğr. Gör. Dr., Süleyman Demirel University, Distance Education Application and Research Center, onurpisirir@sdu.edu.tr, ORCID: 0000-0001-6895-3420.

[2] Isparta University of Applied Sciences, Faculty of Technology, l1722705050@isparta.edu.tr, ORCID: 0009-0009-4799-6056.

Figure 1. (a) Electric power consumption by sector (IEA, 2021) and (b) electric power generation by source (Ritchie and Rosado, 2020)
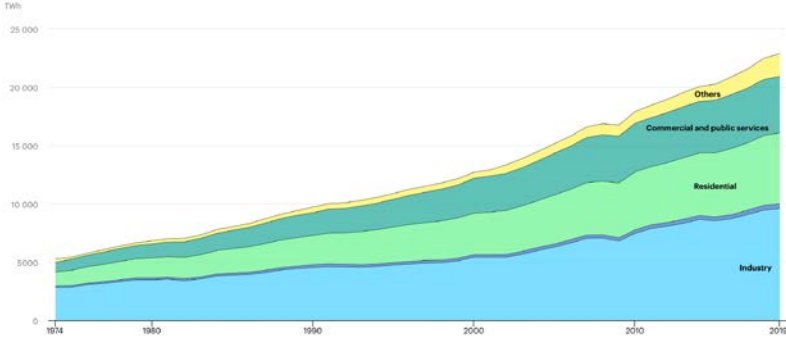
(a)
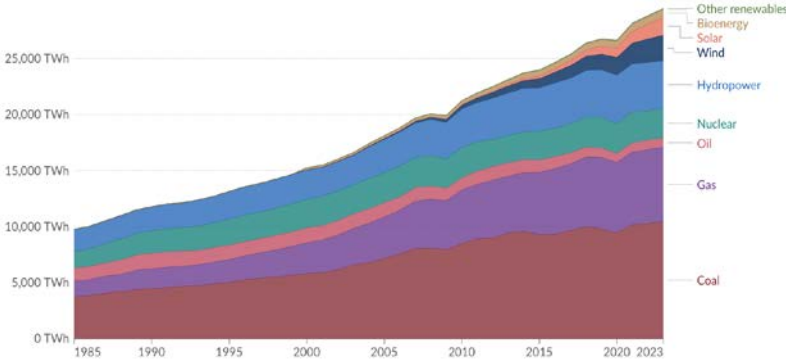
(b)

Different types of energy, such as light, heat, electromagnetic radiation, and motion in the environment, can be converted into electrical energy with photovoltaic, thermoelectric, electromagnetic radiation, electromagnetic induction, electrostatic induction, and piezoelectric effect energy harvesting technologies, as shown in Figure 2. The conversions are realized by transducers such as photovoltaic cells, thermoelectric, inductors, and piezoelectric (Chen, 2019). Radiofrequ 12 mW/cm^2, thermoelectric 60 μW/cm^3, piezoelectric

7.31 mW g^2/cm^3 and photoelectric $15mW/cm^2$ energy density conversion can be achieved. (Mohammadi and Sohn, 2023).

Figure 2. Energy harvesting technologies
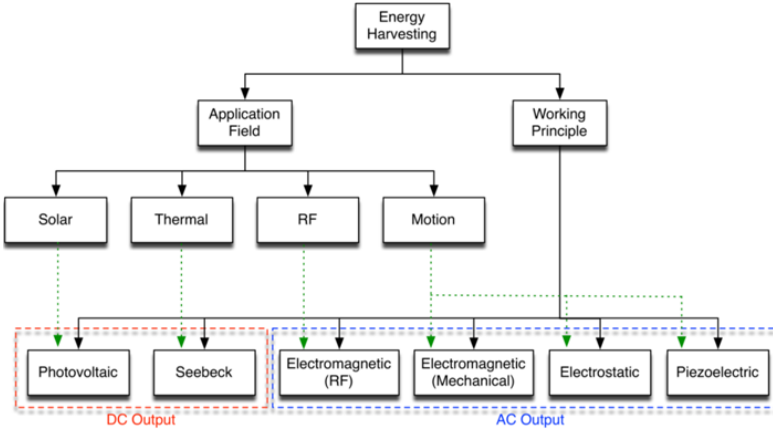
Source: (Caliò et. al., 2014)

The working principles of piezoelectric, electromagnetic and electrostatic mechanical energy harvesting methods are shown in Figure 3 (a), Figure 3 (b), and Figure 3 (c) below. Among the piezoelectric, electromagnetic, and electrostatic mechanical energy harvesting technologies with energy density values of 35,4 mj/cm^3, 24,8 mj/cm^3 and 4 mj/cm^3 respectively, piezoelectric is characterized by maximum output power, no need to control the gap and small size, electromagnetic by high output current, long life and robustness and durability, and electrostatic by the ease of size reduction, high output voltage and adjustable coupling coefficient. (Wakshume and Płaczek, 2024).

Figure 3. (a) piezoelectric, (b) electromagnetic, and (c) electrostatic mechanical energy harvesting technologies
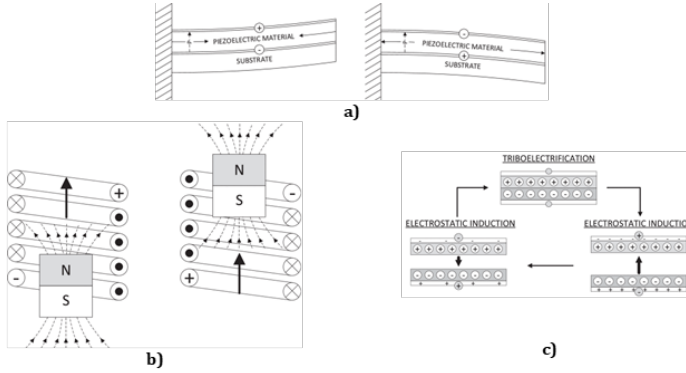
Source: (Díez, et. al., 2019)

2. PIEZOELECTRIC ENERGY HARVESTING

Figure 4, which includes the classification of ferroelectric, pyroelectric, and piezoelectric crystals with pyroelectric and piezoelectric effects, shows the class relationship. Ferroelectricity provides polarity change with an electric field, pyroelectricity provides heat, and piezoelectricity provides the conversion of mechanical energy into electrical energy.

Figure 4. The relationship between dielectric, piezoelectric, pyroelectric, and ferroelectric materials
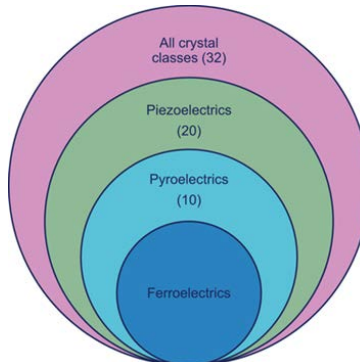
Source: (Vijayakanth and Thangavel et al., 2022)

Figure 5 shows the classification of piezoelectric materials. Among the classes of piezoelectric materials, natural single crystals have the characteristics of highly ordered structure and high performance, ceramics have high performance, high crystallinity, and resistance to harsh conditions, polymers have light weight, flexibility, and easy processability, while composites have the properties of both ceramics and polymers. (Sapkal, Kandasubramanian and Panda, 2022).

Figure 5. Classification of piezoelectric materials
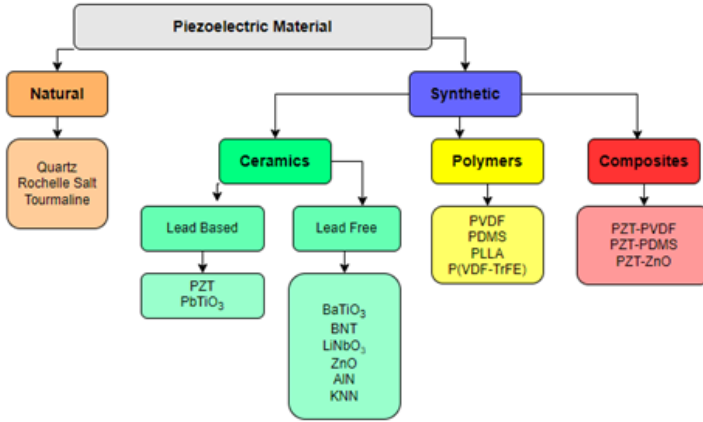
Source: (Brusa, Carrera, and Delprete, 2023)

Among the piezoelectric transducer types, the cantilever beam in Figure 6 (a) is preferred for maximum stress applications, the circular diaphragm in Figure 6 (b) for low-frequency applications, the bell type in Figure 6 (c) for high-impact force applications and the stack type in Figure 6 (d) for high-pressure applications. The electrical power of materials that can operate with piezoelectric and inverse piezoelectric effects in different modes is related to the transducer diameter (Sx), deformation depth (Dx), and frequency (fx) (Han and Ko, 2021).

Figure 6. (a) Cantilever beam, (b) circular diaphragm, (c) bell type, and (d) stack type piezoelectric transducer types
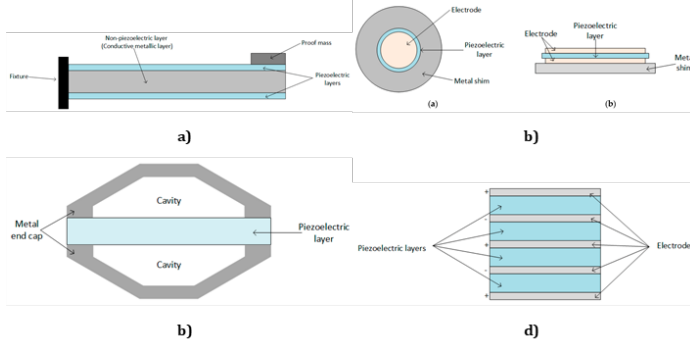
Source: (Covaci and Gontean, 2020)

The operating modes of the piezoelectric transducers, numbered according to polarization and force directions, are shown in Figure 7. Of the modes, the d31 mode provides a relatively high output in current and the d33 mode in voltage (Sezer and Koç, 2021).

Figure 7. Piezoelectric transducer operating modes
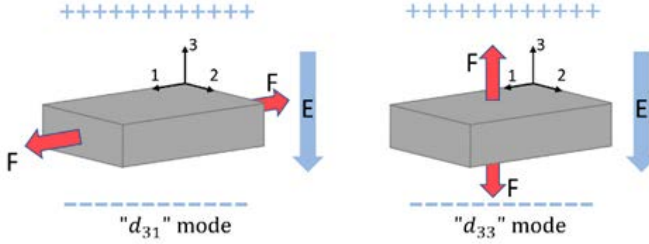
Source: (Zhao, 2023)

As shown in Figure 8, a two-way energy conversion can take place: the piezoelectric effect, where mechanical stress is converted into electricity, and the inverse piezoelectric effect, where electricity is converted into motion. The equations of piezoelectric and inverse piezoelectric effect transformations are given in Equation 1 and Equation 2 (Truitt and Mahmoodi, 2013).

$$D = \varepsilon^T E + d_{ij}T \qquad\qquad (1)$$

$$S = d_{ij}E + s^E T \qquad\qquad (2)$$

Figure 8. Electromechanical coupling of piezoelectric effect
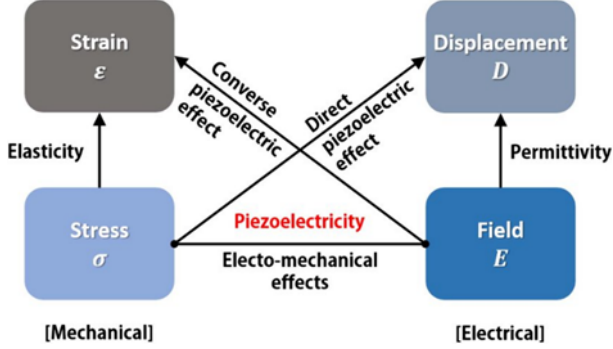
Source: (Song, 2019)

Figure 9 shows the equivalent circuit of the piezoelectric conversion. It can be seen that the mechanical part of the piezoelectric energy harvesting system, which consists of mechanical parts modeled with an inductor, resistor, and capacitor and electrical parts modeled with a capacitor, can also be modeled with an alternating current source.

Figure 9. Piezoelectric energy harvesting equivalent circuit
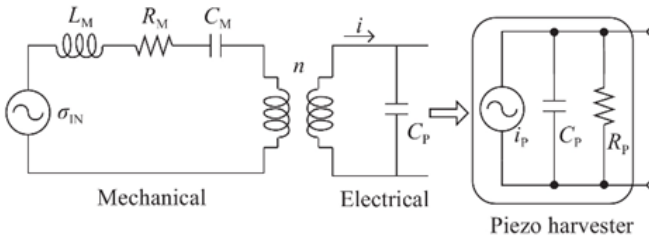
Source: (Liu et. al., 2018)

As shown in the equivalent circuit, electronic circuit interfaces shared in Figure 10 are used to ensure maximum power transfer by reducing reactive power and switching losses during

energy harvesting from piezoelectric materials acting as AA sources with capacitive characteristics.

Developments in the field of PEH, piezoelectric materials and transducer designs, PEH modeling, and electrical power interfaces, MEMS/NEMS PEH technologies, vibrations, PEH from biological applications, fluids, and waste energy are ongoing (Ghazanfarian, Mohammadi and Uchino, 2021). Research is being conducted on achieving high power output to further expand the application areas (Wu, Bao and Wang, 2021). Among the application areas where research is being carried out, PEH tiles can be given as an example (Sharma et al., 2022). Research on the geometries of these transducer structures is ongoing (Pradeesh et al., 2022). Cantilever beam configurations such as unimorph, bimorph, and fixed-end beam, spiral cantilever with end mass, magnetic mass, and magnetic coupling, and spring pendulum system modifications are used to improve performance (Zhu et al., 2021). Research shows that the efficiency of transducers in cantilever beam structures can be increased with optimization algorithms (Yurchenko et al., 2022).

Figure 10. Structures and applications of PEH IC
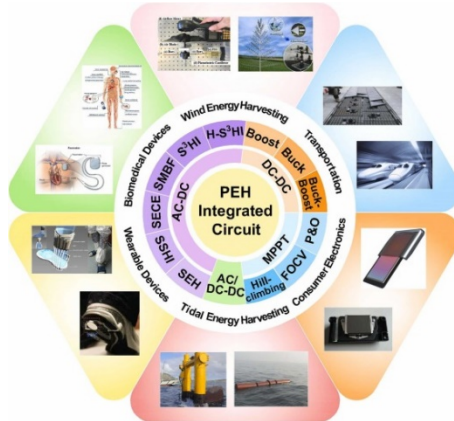
Source: (Li et al., 2022)

3. PIEZOELECTRIC WIND ENERGY HARVESTING (PWEH)

Piezoelectric wind energy harvesting (PWEH), which has applications in subway tunnel wind energy, low-power sensor energy harvesting, waterproof hybrid wind energy harvester, and aviation piezo wind harvester, has flow-induced vibration (FIV), turbulence-induced vibration (TIV), vortex-induced vibration (VIV), wind-induced vibration (WIV), galloping, aero-elastic flutter and flapping working principle types (Ali et al., 2024). Research is ongoing in the field of PWEH operating principles, especially VIV, where optimum efficiency can be achieved at low wind speed, aero-elastic flutter, where self-excitation and deflection can be achieved, and galloping, which combines both positive features (Wen et al., 2021). Hybrid operating principles, such as the combination of VIV and galloping, are also being investigated (Du et al., 2024). In this research, different geometries are developed to ensure optimization (Shi, Hu and Zou, 2022). Research on PWEHs, which are classified according to bluff, blade, flag, wind concentrator, and wind turbine structures, continues in the fields of theoretical modeling, structure, application, and signal processing, and it is foreseen to develop application designs such as power generation, energy storage and wind distribution in the future (Zheng, et al., 2023). Work is ongoing on platform geometries such as flags (Yang et al., 2021). Ongoing studies show that performance can be improved by modifications to structures such as bluffs (Zhang et al., 2024). Studies are being conducted to evaluate various application areas of PWEH, such as building integration (Calautit and Johnstone, 2023). In addition to wind energy, energy can also be harvested from different flow types, such as water flow and ocean waves with PEH transducers (Naqvi et al., 2022).

It is seen that the studies in the literature shared in Table 1 are generally carried out on the operating principles and structure

classes of PWEH. Operating principles and construction classes directly affect PWEH efficiency (Ma and Zhou, S., 2022). Among these studies, rotary PWEH transducers were also mentioned (Liu et al., 2023).

Table 1. PWEH experimental studies

Technology	Description	Resource
R-PWEH	Rotating PWEH	He et al., 2022
NC-PWEH	Non-contact PWEH	Wang et al., 2021
PEHCG/ PEHTG	PEH based on Coupled transverse and interference galloping Effect	Kim, Lee and Seok, 2022
Multimodal PWEH	Multimodal PWEH model	Sheeraz et al., 2022
MC-PWEH	PWEH excited indirectly by a coupler via magnetic-field coupling	Kan et al., 2021
Omnidirectional PWEH	Omnidirectional PWEH	Shi et al., 2021
	In-plane omnidirectional flutter PWEH	Li et al., 2023
Low-speed PWEH	Spindle-like and butterfly-like bluff body PWEH	Wang et al., 2020
Hybrid PWEH	Conjunction of VIV and galloping body PWEH	Yang et al., 2020
PWEH with stepped beam	Galloping-based PWEH with stepped beam	Zhang et al. , 2020
PEHS	Piezoelectric energy harvesting systems with wind catcher	Sitharthan et al., 2021
Bladeless vibration-based PWEH wind turbine	VIV design	Younis et al., 2022
PEH-MFC	Macro fiber composites based on flutter mode PEH	Liu et al., 2020
PWEH (RLC-VEM)	PWEH windmill with rotary to linear converter and vibration enhancement mechanism	Sheeraz et al., 2021
Microscale PWEH	Cantilevered beam PWEH	Alaei, Afrasiab and Dardel, 2020
Wariable cross-section cantilever-based PWEH	PWEH for low-speed wind	Zhao et al., 2022
BPEH	Bistable PEH	Liu et al., 2023
Non-contact PWEH	Magnetic-coupling non-contact PWEH	Liao et al., 2022
TEP-WEH	Hybrid Triboelectric-Electromagnetic-Piezoelectric WEH	Tian et al., 2024
DE-PWEH	Double-bluffbody exciter PWEH	Wang et al., 2023
MNPWEH	Multi-degree-of-freedom and magnetic PWEH	Wei et al., 2024
Double acting PEH	Improved windmill model	He et al., 2021
FD-PENG	Flutter-driven piezoelectric nanogenerator	Gu et al., 2024

4. RESULTS AND DISCUSSION

The electrical energy needed in various sectors such as industry, commerce and households is derived from primary energy sources such as heat, light, electromagnetic fields and motion. These energy transformations are realized through energy harvesting technologies such as alternators, generators, photovoltaic cells and thermovoltaic cells. In addition to macro-scale applications, sectors with high energy demand are turning to micro energy harvesting methods with technologies such as wireless sensor networks, self-powered devices and micro-electromechanical systems (MEMS). Mechanical energy harvesting methods include electromagnetic, triboelectric and electrostatic methods as well as piezoelectric energy harvesting (PEH). Piezoelectric materials can be produced in various classes such as crystalline, ceramic, polymer and composite and can have piezoelectric and ferroelectric properties. Piezoelectric transducers are available in various structures such as cantilever beams, circular diaphragms, bell type, and stack types and are generally used in two different modes of operation. The piezoelectric and inverse piezoelectric effect enables bidirectional energy conversion, and PEH systems are integrated with equivalent circuit compatible converters.

Considering the energy production and consumption data, it is seen that the transition to sustainable energy has become a necessity. In this context, there is a shift from non-renewable fossil fuels such as coal, natural gas, and oil to renewable energy sources such as solar, wind, and hydroelectricity. Among renewable energy sources, piezoelectric transducers for harvesting wind energy are called PWEH (Piezoelectric Wind Energy Harvesters) transducers. While electromagnetic conversion in wind power plants (WPPs) is realized at the macro scale through alternators, PWEH systems provide energy conversion at the micro-scale with piezoelectric generators. These

transducers are used on the bluff body (obstacle), wing, flag, wind concentrator, and wind turbine body structures by working principles such as FIV (Fluid-Induced Vibration), TIV (Turbulent-Induced Vibration), VIV (Vortex-Induced Vibration), WIV (Wake-Induced Vibration), aeroelastic flutter and flapping. Intensive research on airframe structures and operating principles in these areas is ongoing.

As a result of these developments, solutions for battery replacement or charging problems are expected to be developed in microsystems, while in macro systems, it is aimed to reduce greenhouse gas emissions and thus carbon footprint by providing energy efficiency and savings.

5. CONCLUSION

Due to the risk of depletion and environmental damage of non-renewable energy sources, global energy policies are increasingly shifting towards renewable energy sources. This transition is encouraging the development of micro-energy systems, not only for large-scale power generation but also for low-power devices. In particular, piezoelectric energy harvesting (PEH) systems based on the collection of mechanical energy present in the environment are among the leading technologies in this field. With ongoing research, PEH micro energy systems, which are widely used today, are expected to develop further in the future and become a dominant solution in devices with low power requirements.

Although experimental studies on piezoelectric wind energy harvesting (PWEH) have limited application areas for the time being, research on increasing efficiency in this field has gained momentum. Literature reviews on operating principles and body structures reveal that this technology is adaptable to a wider range of applications and has significant potential,

especially for wind energy harvesting. The integration of PWEH with macro-scale energy harvesting systems in wind power plants (WPPs) shows that it can be used both in micro-energy systems and as an effective method for macro-scale energy harvesting in the future.

In this context, research on PWEH offers an important solution to optimize the use of renewable energy sources and especially to efficiently convert wind energy at both micro and macro levels. Therefore, PWEH is expected to become more prominent in the future as a sustainable alternative to meet the energy needs of low-power sensor networks, MEMS devices, and other electronic devices. These developments will not only lead to increased efficiency in power generation but also contribute to carbon footprint reduction and environmental sustainability.

REFERENCES

Alaei, E., Afrasiab, H., & Dardel, M. "Analytical and numerical fluid–structure interaction study of a microscale piezoelectric wind energy harvester." Wind Energy 23.6 (2020): 1444-1460.

Ali, A., Ali, S., Shaukat, H., Khalid, E., Behram, L., Rani, H., ... & Noori, M. "Advancements in piezoelectric wind energy harvesting: A review." Results in Engineering (2024): 101777.

Brusa, E., Carrera, A., & Delprete, C. "A Review of Piezoelectric Energy Harvesting: Materials, Design, and Readout Circuits." Actuators. Vol. 12. No. 12. MDPI, 2023.

Calautit, K., & Johnstone, C. "State-of-the-art review of micro to small-scale wind energy harvesting technologies for building integration." Energy Conversion and Management: X (2023): 100457.

Caliò, R., Rongala, U. B., Camboni, D., Milazzo, M., Stefanini, C., De Petris, G., & Oddo, C. M. "Piezoelectric energy harvesting solutions." Sensors 14.3 (2014): 4755-4790.

Chen, B. "Introduction to energy harvesting transducers and their power conditioning circuits." Low-Power Analog Techniques, Sensors for Mobile Devices, and Energy Efficient Amplifiers: Advances in Analog Circuit Design 2018 (2019): 3-12.

Covaci, C., & Gontean, A. "Piezoelectric energy harvesting solutions: A review." Sensors 20.12 (2020): 3512.

Díez, P. L., Gabilondo, I., Alarcón, E., & Moll, F. "Mechanical energy harvesting taxonomy for industrial environments: Application to the railway industry." IEEE Transactions on Intelligent Transportation Systems 21.7 (2019): 2696-2706.

Du, W., Liang, L., Zhou, Z., Qin, W., Huang, H., & Cao, D. "Enhancing piezoelectric energy harvesting from the flow-induced vibration of an apple-shaped bluff body based on topology optimization." Energy (2024): 132667.

Ghazanfarian, J., Mohammadi, M. M., & Uchino, K. "Piezoelectric energy harvesting: a systematic review of reviews." Actuators. Vol. 10. No. 12. MDPI, 2021.

Gu, J., Lee, D., Park, H., & Kim, K. "Flutter-Driven Piezoelectric Wind Energy Harvesting System Based on PVDF Nanofiber for Low Power Applications." International Journal of Precision Engineering and Manufacturing-Green Technology (2024): 1-12.

Han, H., & Ko, J. "Power-generation optimization based on piezoelectric ceramic deformation for energy harvesting application with renewable energy." Energies 14.8 (2021): 2171.

Hannah Ritchie and Pablo Rosado (2020) - "Electricity Mix" Published online at OurWorldinData.org. Retrieved from: 'https://ourworldindata.org/electricity-mix' [Online Resource]

He, L., Gu, X., Han, Y., Zhou, Z., Tian, X., & Cheng, G. "Nonlinear dual action piezoelectric energy harvester for collecting wind energy from the environment." Journal of Alloys and Compounds 889 (2021): 161711.

He, L., Han, Y., Liu, R., Hu, R., Yu, G., & Cheng, G. "Design and performance study of a rotating piezoelectric wind energy harvesting device with wind turbine structure." Energy 256 (2022): 124675.

IEA (2021), World electricity final consumption by sector, 1974-2019, IEA, Paris https://www.iea.org/data-and-

statistics/charts/world-electricity-final-consumption-by-sector-1974-2019, Licence: CC BY 4.0

Kan, J., Liao, W., Wang, S., Chen, S., Huang, X., & Zhang, Z. "A piezoelectric wind energy harvester excited indirectly by a coupler via magnetic-field coupling." Energy Conversion and Management 240 (2021): 114250.

Kim, H., Lee, J., & Seok, J. "Novel piezoelectric wind energy harvester based on coupled galloping phenomena with characterization and quantification of its dynamic behavior." Energy Conversion and Management 266 (2022): 115849.

Li, D., Wang, C., Cui, X., Chen, D., Fei, C., & Yang, Y. "Recent progress and development of interface integrated circuits for piezoelectric energy harvesting." Nano Energy 94 (2022): 106938.

Li, S., Feng, Z., He, X., Ye, Y., & Li, J. "An in-plane omnidirectional flutter piezoelectric wind energy harvester." Mechanical Systems and Signal Processing 200 (2023): 110637.

Liao, W., Zhang, Z., Huang, X., Zhang, L., Wang, S., & Kan, J. "A novel magnetic-coupling non-contact piezoelectric wind energy harvester with a compound-embedded structure." IEEE Sensors Journal 22.9 (2022): 8428-8438.

Liu, J., Zuo, H., Xia, W., Luo, Y., Yao, D., Chen, Y., ... & Li, Q. "Wind energy harvesting using piezoelectric macro fiber composites based on flutter mode." Microelectronic Engineering 231 (2020): 111333.

Liu, L., He, L., Han, Y., Zheng, X., Sun, B., & Cheng, G. "A review of rotary piezoelectric energy harvesters." Sensors and Actuators A: Physical 349 (2023): 114054.

Liu, L., Pang, Y., Yuan, W., Zhu, Z., & Yang, Y. "A self-powered piezoelectric energy harvesting interface circuit with efficiency-enhanced P-SSHI rectifier." Journal of Semiconductors 39.4 (2018): 045002.

Liu, X., Jia, H., Li, M., Li, Y., Tao, Y., & Dai, F. "Piezoelectric wind energy harvester of bi-stable hybrid symmetric laminates." Composites Science and Technology 242 (2023): 110198.

Ma, X., & Zhou, S. "A review of flow-induced vibration energy harvesters." Energy Conversion and Management 254 (2022): 115223.

Mohammadi, M., & Sohn, I. "AI based energy harvesting security methods: A survey." ICT Express 9.6 (2023): 1198-1208.

Molla, S., Farrok, O., & Alam, M. J. "Electrical energy and the environment: Prospects and upcoming challenges of the World's top leading countries." Renewable and Sustainable Energy Reviews 191 (2024): 114177.

Naqvi, A., Ali, A., Altabey, W. A., & Kouritem, S. A. "Energy harvesting from fluid flow using piezoelectric materials: a review." Energies 15.19 (2022): 7424.

Pradeesh, E. L., Udhayakumar, S., Vasundhara, M. G., & Kalavathi, G. K. "A review on piezoelectric energy harvesting." Microsystem Technologies 28.8 (2022): 1797-1830.

Sapkal, S., Kandasubramanian, B., & Panda, H. S. "A review of piezoelectric materials for nanogenerator applications." Journal of Materials Science: Materials in Electronics 33.36 (2022): 26633-26677.

Sezer, N., & Koç, M. "A comprehensive review on the state-of-the-art of piezoelectric energy harvesting." Nano energy 80 (2021): 105567.

Sharma, S., Kiran, R., Azad, P., & Vaish, R. "A review of piezoelectric energy harvesting tiles: Available designs and future perspective." Energy Conversion and Management 254 (2022): 115272.

Sheeraz, M. A., Malik, M. S., Rahman, K., Elahi, H., Khurram, M., Eugeni, M., & Gaudenzi, P. "Multimodal piezoelectric wind energy harvester for aerospace applications." International Journal of Energy Research 46.10 (2022): 13698-13710.

Sheeraz, M. A., Malik, M. S., Rehman, K., Elahi, H., Butt, Z., Ahmad, I., ... & Gaudenzi, P. "Numerical assessment and parametric optimization of a piezoelectric wind energy harvester for IoT-based applications." Energies 14.9 (2021): 2498.

Shi, T., Hu, G., & Zou, L. "Aerodynamic shape optimization of an arc-plate-shaped bluff body via surrogate modeling for wind energy harvesting." Applied Sciences 12.8 (2022): 3965.

Shi, T., Hu, G., Zou, L., Song, J., & Kwok, K. C. "Performance of an omnidirectional piezoelectric wind energy harvester." Wind Energy 24.11 (2021): 1167-1179.

Sitharthan, R., Yuvaraj, S., Padmanabhan, S., Holm-Nielsen, J. B., Sujith, M., Rajesh, M., ... & Vengatesan, K. "Piezoelectric energy harvester converting wind aerodynamic energy into electrical energy for microelectronic application." IET Renewable Power Generation 15.9 (2021): 1968-1975.

Song, Y. "Finite-element implementation of piezoelectric energy harvesting system from vibrations of railway bridge." Journal of Energy Engineering 145.2 (2019): 04018076.

Tian, S., Lai, L., Xin, J., Qu, Z., Li, B., & Dai, Y. "Hybrid Triboelectric-Electromagnetic-Piezoelectric Wind Energy Harvester toward Wide-Scale IoT Self-Powered Sensing." Small 20.20 (2024): 2307282.

Truitt, A., & Mahmoodi, S. N. "A review on active wind energy harvesting designs." International Journal of Precision Engineering and Manufacturing 14 (2013): 1667-1675.

Vijayakanth, Thangavel, et al. "Recent advances in organic and organic–inorganic hybrid materials for piezoelectric mechanical energy harvesting." Advanced Functional Materials 32.17 (2022): 2109492.

Wakshume, D. G., & Płaczek, M. Ł. "Optimizing Piezoelectric Energy Harvesting from Mechanical Vibration for Electrical Efficiency: A Comprehensive Review." Electronics 13.5 (2024): 987.

Wang, J., Kan, J., Gu, Y., He, C., Ren, Z., Meng, F., ... & Zhang, Z. "Design, performance evaluation and calibration of an indirectly-excited piezoelectric wind energy harvester via a double-bluffbody exciter." Energy Conversion and Management 284 (2023): 116969.

Wang, J., Zhang, C., Gu, S., Yang, K., Li, H., Lai, Y., & Yurchenko, D. "Enhancement of low-speed piezoelectric wind energy harvesting by bluff body shapes: Spindle-like and butterfly-like cross-sections." Aerospace Science and Technology 103 (2020): 105898.

Wang, S., Liao, W., Zhang, Z., Liao, Y., Yan, M., & Kan, J. "Development of a novel non-contact piezoelectric wind energy harvester excited by vortex-induced vibration." Energy Conversion and Management 235 (2021): 113980.

Wei, N., Zhang, Z., Cheng, G., Yang, H., Hu, Y., & Wen, J. "Study of a vortex-induced vibration piezoelectric wind energy

harvester based on the synergy of multi-degree-of-freedom technology and magnetic nonlinear technology." Mechanical Systems and Signal Processing 214 (2024): 111381.

Wen, Q., He, X., Lu, Z., Streiter, R., & Otto, T. "A comprehensive review of miniatured wind energy harvesters." Nano Materials Science 3.2 (2021): 170-185.

Wu, N., Bao, B., & Wang, Q. "Review on engineering structural designs for efficient piezoelectric energy harvesting to obtain high power output." Engineering Structures 235 (2021): 112068.

Yang, K., Nabawy, M. R., Cioncolini, A., Revell, A., & AlGhrairy, S. "Planform geometry effects of piezoelectric wind energy harvesting composite inverted flags." Smart Materials and Structures 30.11 (2021): 115014.

Yang, K., Su, K., Wang, J., Wang, J., Yin, K., & Litak, G. "Piezoelectric wind energy harvesting subjected to the conjunction of vortex-induced vibration and galloping: comprehensive parametric study and optimization." Smart Materials and Structures 29.7 (2020): 075035.

Younis, A., Dong, Z., ElBadawy, M., AlAnazi, A., Salem, H., & AlAwadhi, A. "Design and development of bladeless vibration-based piezoelectric energy–harvesting wind turbine." Applied Sciences 12.15 (2022): 7769.

Yurchenko, D., Machado, L. Q., Wang, J., Bowen, C., Sharkh, S., Moshrefi-Torbati, M., & Val, D. V. "Global optimisation approach for designing high-efficiency piezoelectric beam-based energy harvesting devices." Nano Energy 93 (2022): 106684.

Zhang, D., Zhang, X., Tan, P., Li, S., & Yin, P. "Exploring the influence of concave-convex surface modifications on

piezoelectric wind energy harvesting: A numerical analysis." Ocean Engineering 311 (2024): 118866.

Zhang, J., Qu, D., Fang, Z., & Shu, C. "Optimization of a piezoelectric wind energy harvester with a stepped beam." Journal of Mechanical Science and Technology 34 (2020): 4357-4366.

Zhao, B., Qian, F., Hatfield, A., Zuo, L., & Xu, T. B. "A review of piezoelectric footwear energy harvesters: Principles, methods, and applications." Sensors 23.13 (2023): 5841.

Zhao, K., Zhang, Q., Wang, W., Han, J., & Hao, S. "Topological optimization of a variable cross-section cantilever-based piezoelectric wind energy harvester." Frontiers in Materials 9 (2022): 956182.

Zheng, X., He, L., Wang, S., Liu, X., Liu, R., & Cheng, G. "A review of piezoelectric energy harvesters for harvesting wind energy." Sensors and Actuators A: Physical 352 (2023): 114190.

Zhu, H., Tang, T., Yang, H., Wang, J., Song, J., & Peng, G. "The State-of-the-Art Brief Review on Piezoelectric Energy Harvesting from Flow-Induced Vibration." Shock and Vibration 2021.1 (2021): 8861821.

ÇOK SEVİYELİ DÖNÜŞTÜRÜCÜLERDE MODÜLASYON YÖNTEMLERİ[1]

Merve MOLLAHASANOĞLU[2]

Halil İbrahim OKUMUŞ[3]

1. GİRİŞ

Çok seviyeli dönüştürücüler, modern güç elektroniği sistemlerinde özellikle elektrikli araçlar (EV) gibi uygulamalar için kritik öneme sahiptir. Elektrikli araçların hızlı şarj sistemleri, yüksek verimlilik, düşük harmonik bozulma ve enerji kayıplarını minimize eden çözümlere ihtiyaç duyar. Bu noktada çok seviyeli dönüştürücüler, sağladıkları yüksek çözünürlüklü gerilim ve akım sinyalleri sayesinde, geleneksel dönüştürücülere kıyasla önemli avantajlar sunar. Modülasyon yöntemleri ise bu dönüştürücülerde performans ve verimliliği en üst düzeye çıkaran anahtarlama stratejilerini optimize eder.

Hızlı şarj istasyonlarının artan talebi, enerji yönetimi ve batarya sağlığı açısından gelişmiş modülasyon yöntemlerine duyulan ihtiyacı artırarak çok seviyeli dönüştürücülerin rolünü daha da kritik hale getirmiştir. Bu dönüştürücüler, fazla enerji seviyesi barındırdıkları için yüksek verimlilik, düşük harmonik distorsiyon ve üstün performans sağlar. Modülasyon stratejisi,

dönüştürücünün topolojisi ile doğrudan ilişkili olup, sistemin genel performansını büyük ölçüde etkiler. Çok seviyeli dönüştürücülerde, her biri farklı uygulamalara dolayısıyla farklı avantajlara sahip çeşitli modülasyon yöntemleri kullanılmaktadır. En yaygın teknikler arasında Taşıyıcı Tabanlı Darbe Genişlik Modülasyonu (DGM) ve Uzay Vektör Modülasyonu (UVM) bulunmaktadır.

Seviye Kaydırmalı DGM ve Faz Kaydırmalı DGM gibi taşıyıcı tabanlı DGM teknikleri, basitlikleri ve basit uygulama prensiplerinden dolayı yaygın olarak kullanılmaktadır. Bu yöntemler, dönüştürücü için anahtarlama sinyalleri üretmek üzere bir modülasyon sinyalinin üçgen bir taşıyıcı dalga ile karşılaştırılmasını içerir. Özellikle faz kaydırmalı yaklaşım, anahtarlama eylemlerini dönüştürücünün fazları arasında dağıtarak harmonik bozulmayı en aza indirme ve çıkış kalitesini artırma kabiliyetiyle dikkat çekmektedir (Mollahasanoglu ve diğerleri, 2024).

Uzay Vektör Modülasyonu, gerilim kontrolü ve harmonik azaltma açısından gelişmiş performans sunan bir diğer önemli tekniktir. UVM, iki boyutlu bir gerilim uzayında çalışır ve önceden tanımlanmış bir vektör kümesinden uygun anahtarlama durumlarını seçerek çıkış gerilimlerinin hassas denetimini sağlar. Bu yöntem özellikle ortak mod gerilimini (CMV) ortadan kaldırmada ve çok seviyeli dönüştürücülerde toplam harmonik bozulmayı (THD) azaltmada etkilidir (Boopathi, Jayanthi ve Ansari, 2020). Ancak UVM'nin karmaşıklığı, daha basit PWM tekniklerine kıyasla genellikle daha fazla hesaplama kaynağı gerektirmektedir (Mollahasanoglu ve diğerleri, 2023).

Bu çalışmada, çok seviyeli dönüştürücülerde yaygın olarak kullanılan modülasyon teknikleri, teorik bir çerçevede ele alınacaktır. Özellikle uzak vektör modülasyonu ve darbe genişlik modülasyonu üzerine odaklanılarak, bu yöntemlerin temel

prensipleri, çok seviyeli yapılar üzerindeki etkileri ve güç elektroniği sistemlerindeki genel uygulamaları incelenecektir. Modülasyon tekniklerinin performansa olan katkıları, harmonik içeriği azaltmadaki rolleri ve anahtarlama stratejileri bağlamında değerlendirilecektir.

2. ÇOK SEVİYELİ DÖNÜŞTÜRÜCÜLER İÇİN MODÜLASYON YÖNTEMLERİ

Çok seviyeli dönüştürücülerde kullanılan modülasyon yöntemleri Şekil 1'de gösterildiği gibi kategorize edilmiştir.

Şekil 1. Çok Seviyeli Dönüştürücülerde Kullanılan Modülasyon Yöntemleri
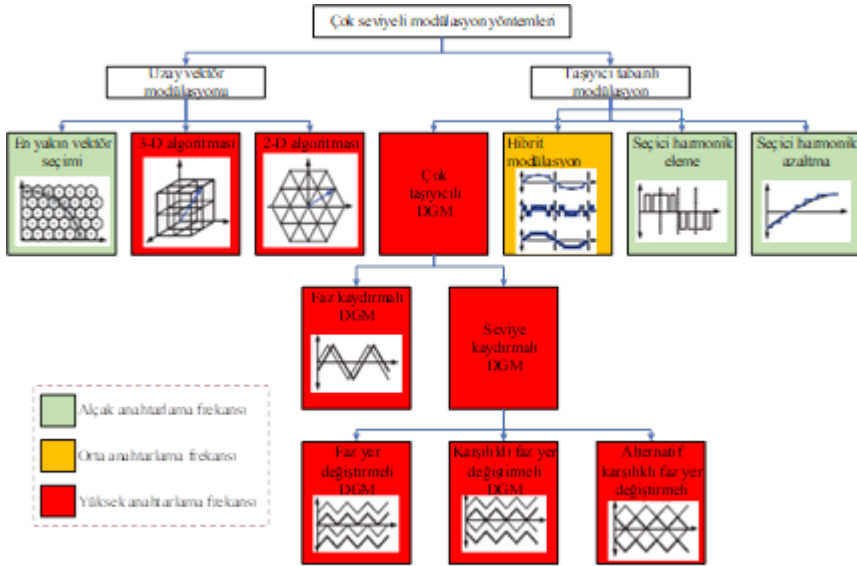
Şekil 1'de görüldüğü gibi, DGM ailesine ait olan bu modülasyon teknikleri, birbirlerinden farklı yapıda olmalarına rağmen belirgin bir üstünlük göstermemektedir. Bu yöntemlerin ikisinin de kendi içinde avantajları ve dezavantajları bulunmaktadır. Uzay Vektör Modülasyonu, DGM'nin

başaramadığı ek anahtarlama durumlarını oluşturarak, daha fazla serbestlik derecesi sunabilir.

UVM, üç aşamalı bir işlem gerektirir: vektör seçimi, görev döngüsü hesaplaması ve vektör sıralaması (Maswood ve Tafti, 2018). İki ve üç boyutlu UVM yöntemleri klasik UVM ile karşılaştırıldığında, klasik UVM daha düşük hesaplama maliyeti sunar. Taşıyıcı tabanlı klasik DGM yöntemleri, çok seviyeli dönüştürücüler için daha fazla taşıyıcı gerektirirken, UVM bu taşıyıcı sayısını artırmadan hesaplamalara dayalıdır. Ancak UVM, yüksek anahtarlama frekansı gerektirdiği için, yüksek güçlü uygulamalar için fazladan anahtarlama kayıpları oluşturabilir (Palanisamy ve diğerleri, 2023). UVM teknikleri hakkında birçok çalışmaya rağmen, taşıyıcı tabanlı modülasyon özellikle elektrikli araç şarj topolojileri için endüstride daha sık tercih edilmektedir.

EA hızlı şarj topolojilerinde kullanılan taşıyıcı tabanlı modülasyon teknikleri, düşük maliyetli dijital işlemciler ile uygulanabilmektedir. UVM ve taşıyıcı tabanlı modülasyon tekniklerinin karşılaştırmalı analizleri, çok seviyeli H-köprü evirici ve diyot kenetlemeli dönüştürücü, sırasıyla (Andler ve diğerleri, 2009) ve (Kouro, Perez, Robles ve Rodriguez, 2008)'de ele alınmıştır. Bu çalışmalar, her iki yöntem arasındaki anahtarlama kayıplarının benzer olduğunu göstermektedir. Endüstriyel uygulamalarda UVM ve taşıyıcı tabanlı DGM yöntemleri arasında net bir seçim yapmak, güç elektroniği dönüştürücüsünün özelliklerine bağlıdır. Genellikle yüksek anahtarlama frekanslarında, taşıyıcı tabanlı sinüzoidal DGM, 1 kHz'in üzerinde çalışmasına rağmen, yüksek güç gereksinimlerine uygun olarak daha düşük frekanslarda (yaklaşık 500 Hz) kullanılabilir.

2.1. Uzay Vektör Modülasyonu

Genellikle üç fazlı sistemlerde kullanılan bir teknik olan uzay vektör modülasyonu, çok seviyeli dönüştürücülerde, farklı anahtarlama durumları hatlar arasındaki gerilim alanları ile ilişkilendirilir ve bu durumlar, uzay vektör altıgeni meydana getirir. Gerilim referansı da bu altıgenle eşleştirilebilir ve çeşitli anahtarlama durumları ile birleştirilebilir. Bazı vektörler için, bazı kontrol hedeflerine ulaşmak için birden fazla anahtarlama durumu kullanılabilir. Daha fazla seviyeye sahip bir dönüştürücüde, daha fazla uzay vektörü olacaktır. Bu bağlamda, dönüştürücünün anahtarlama durumlarının sayısı, seviye sayısına doğrudan bağlıdır. Yüksek seviyeli dönüştürücüler, daha fazla yedek anahtarlama durumu ve referans gerilimini belirlemek için kompleks hesaplamalar gerektirmektedir. Bu nedenle, UVM yöntemi yüksek seviyeli sistemlerde uygulanabilirliğini kaybedebilir. Fakat, nötr nokta gerilim dengesi için sağlanan kontrol serbestliği nedeniyle, üç seviyeli diyot kenetlemeli dönüştürücü topolojisi için uygun bir seçenek olarak görülebilir.

Üç fazlı güç sistemlerinde, genel olarak $\alpha\beta\gamma$ koordinatları ya da *dq* çerçevesi kullanılarak yüksek performansa sahip kontrolörler geliştirilir. Dengeli sistemlerde γ bileşeni sıfırdır. Dönüştürücünün potansiyel anahtarlama durumları $\alpha\beta$ çerçevesinde gösterilir ve referans gerilimi, ilgili dönüştürücünün en yakın anahtarlama durumlarının bir kombinasyonu ile elde edilir. Uzay vektör modülasyonu, anahtarlama sırasını ve karşılık gelen görev döngülerini belirlemek için geometrik bir problem çözme yaklaşımını benimser (Leon ve diğerleri, 2016). Bu modülasyon yöntemi, ilk olarak iki seviyeli üç fazlı dönüştürücüler için geliştirilmiş, daha sonra çok seviyeli dönüştürücülerde kullanılmak üzere uyarlanmıştır. Durum vektörleri DA gerilim dengesinin kontrolü, ortak mod geriliminin azaltılması ve anahtarlama kayıplarının minimize edilmesi gibi kontrol hedefleri için kullanılabilmektedir.

Şekil 2'de, diyot kenetlemeli doğrultucu için optimize edilmiş anahtarlama dizileriyle uygulanan klasik UVM anahtarlama tekniği yer almaktadır.

Şekil 2. UVM Kontrol Blok Diyagramı
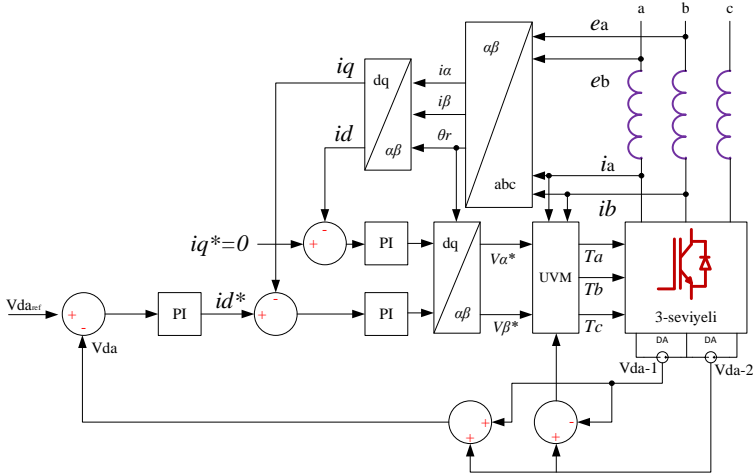
UVM'nin temelinde, üç fazlı akım ile gerilim değerlerini sabit bir referans çerçevesine dönüştürmek vardır. Bu süreçte, üç fazlı a, b ve c gerilimleri iki eksenli d ve q eksenlerine döndürülür. Şekil 2'de diyot kenetlemeli doğrultucu için kullanılan UVM metodu ile gerçekleştirilmiş kontrol şeması, α-β-0 ile d-q dönüşümleri blok olarak gösterilmektedir. Gerilim değerine ilişkin matematiksel ifadeler Denklem 1-3'te verilmiştir:

$$V = V_a + \alpha V_b + \alpha^2 V_c \qquad (1)$$

$$V = V_\alpha + jV_\beta, \quad V_\alpha = \frac{2}{3}(V_a - \frac{1}{2}V_b - \frac{1}{2}V_c) \qquad (2)$$

$$V_\beta = \frac{2}{3}(\frac{\sqrt{3}}{2}V_b - \frac{3}{2}V_c) \qquad (3)$$

Aynı şekilde akım dönüşüm eşitlikleri Denklem 4 ve 5' te ki gibidir.

$$I = I_\alpha + jI_\beta, \ I_\alpha = \frac{2}{3}(I_a - \frac{1}{2}I_b - \frac{1}{2}I_c) \tag{4}$$

$$I_\beta = \frac{2}{3}(\frac{\sqrt{3}}{2}I_b - \frac{3}{2}I_c) \tag{5}$$

Gerilim vektör denklemi ve dönen referans çerçevesinde (d-q) Denklem 6-9'da verilmektedir.

$$V_d = L\frac{di_d}{dt} + \omega L i_q + V_d' \tag{6}$$

$$V_q = 0 = L\frac{di_q}{dt} + \omega L i_d + V_q' \tag{7}$$

$$V*_d = L\frac{di_d}{dt} + \omega L i_q + V_d' - \omega L i_q \tag{8}$$

$$V*_q = 0 = L\frac{di_q}{dt} + \omega L i_d + V_q' - \omega L i_d \tag{9}$$

Burada ω üç fazlı gerilimin açısal frekansını ifade etmektedir. V_d, $V*_d$, i_d ve V_q, V_q', i_q ise sırasıyla d ve q ekseninde V, V' ve i'nin bileşenlerini oluşturmaktadır.

Şekil 3'te ise üç faz üç seviyeli diyot kenetlemeli GFD doğrultucusunda yirmi yedi anahtarlama durumu ve on dokuz vektör olduğu gösterilmektedir.

Şekil 3. GFD doğrultucu için uzay vektördeki tüm anahtarlama durumları (a), ilk sektörün referans vektörü (b)
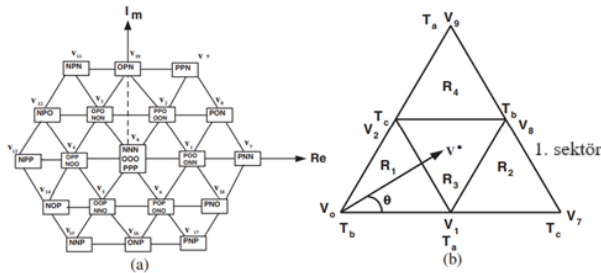
Bu vektörler, 24 bölgeye ayrılmıştır. Her bir sektör ise dört bölge bulunan altı sektöre bölünmektedir. Sıfır vektör V_0, küçük vektörler ($V_1 - V_6$), Orta vektörler ($V_8, V_{10}, V_{12}, V_{14}, V_{16}$ ve V_{18}), Büyük vektörler (V_7, V_9, $V_{11,} V_{13}, V_{15}$ ve V_{17}), olarak dört kategoriye ayrılmıştır. Şekil 3.b'de, karmaşık (α-β) düzleminde 1. sektörün üçüncü bölgesinde bulunan dönen referans vektörü (V^*veya V_{ref}) gösterilmektedir.

2.2. Darbe Genişlik Modülasyon Yöntemi

Güç elektroniği uygulamalarında modülasyon yöntemi geliştirmek için temel yaklaşım, darbe genişlik modülasyonudur (DGM). Bu yöntemde, anahtarlama sinyalleri referans geriliminin yüksek frekanslı bir taşıyıcı sinyalle (genellikle üçgen dalga) karşılaştırılmasıyla oluşturulur. Çok seviyeli dönüştürücüler başlığı altında kullanılan modülasyon yöntemleri, klasik DGM tekniklerinin geliştirilmesiyle gelişmiştir. N seviyeli birçok seviyeli dönüştürücüde, taşıyıcı tabanlı modülasyon yöntemleri, referans gerilimini n-1 adet üçgen taşıyıcıyla karşılaştırır. Bu taşıyıcıların kullanım ve dağıtım durumuna göre DGM yöntemleri sürekli olarak gelişmektedir.

Sinüzoidal DGM (SDGM), iki seviyeli hatta çok seviyeli dönüştürücülerde yaygın olarak tercih edilen bir tekniktir. Bu klasik yöntem, sinüzoidal bir referans geriliminin yüksek frekanslı bir üçgen taşıyıcı dalga ile karşılaştırılmasıyla çalışır. Dönüştürücünün çıkış gerilim genliği, genlik modülasyon indeksi (m_a) ile kontrol edilir. Taşıyıcı dalganın genliği sabit olduğundan, çıkış gerilim genliği referans geriliminin genliğini değiştirerek azaltılıp ya da artırılabilir. Fakat, modülasyon indeksi, 0 ile 1 arasında olmak zorundadır. Aksi takdirde aşırı modülasyon, dönüştürücünün standart dışı çalışmasına yol açabilir. Şekil 4, klasik SDGM tekniğini göstermektedir.

Şekil 4. Klasik Sinüzoidal DGM tekniği anahtarlama işaretleri
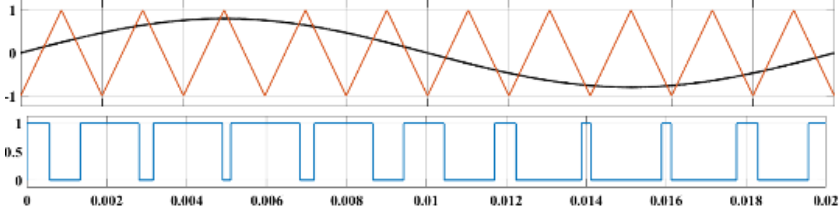
Referans sinyali, üçgen taşıyıcının genliğini aştığında anahtarlama işareti "0" değerini alır. Ayrıca, referans sinyalin genliği, taşıyıcı sinyalin genliğinden daha düşük olduğunda anahtarlama işareti "1" olur, yani anahtar iletim durumundadır. Bu nedenle, anahtarlama darbesinin görev döngüsü, sinüzoidal referans sinyalinin sin (ωt) fonksiyonuna bağlı olarak değişiklik gösterir. Denklem 10, modülasyon süresince anahtarlama darbesini ifade etmektedir:

$$S_x(t) = \begin{cases} 1 & e\breve{g}er \sin(\omega t) > tri(t) \\ 0 & e\breve{g}er \sin(\omega t) < tri(t) \end{cases} \qquad (10)$$

2.2.1. Taşıyıcı Tabanlı Düşük Frekanslı Modülasyon

Yüksek güçlü uygulamalarda (Megavat seviyesindeki), anahtarlama kayıplarını minimize etmek amacıyla güç cihazlarının anahtarlama frekansı genellikle oldukça sınırlıdır. Bu tür sistemlerde anahtarlama sinyalleri neredeyse 1kHz'in altına düşer. Geleneksel taşıyıcı tabanlı DGM (Darbe Genişlik Modülasyonu) veya UVM (Uzay Vektör Modülasyonu) teknikleri, anahtarlamadan kaynaklanan harmonik bozulmalar üretir. Bu durum, standartları karşılayabilmek için filtre boyutlarının büyümesine neden olur.

Çok seviyeli dönüştürücülerde, yüksek güçlü uygulamalarda yüksek frekanslı modülasyon metotları harmonik bozulmalardan kaynaklı büyük filtreler gerektirir. Bu durum uygulamanın tasarımını zorlaştırır, sistemi hantallaştırır ve

gereksiz yere büyütür. Bu sorunu hafifletmek için, değişken anahtarlama işaretlerine dayalı olarak çıkış gerilim dalga biçimlerinin harmonik spektrumu hesaplanır. Analitik hesaplama, harmonik sırasına, modülasyon indeksi ile gerilim dalga biçiminin ana periyodunun dörtte birindeki gerilim geçişlerine göre yapılır. Seçici Harmonik Yok Etme (SHE) yöntemi, bu hesaplamaları kullanarak belirli harmonik bileşenleri ortadan kaldırmayı hedefler (Yang, Liu, Li, Yu ve Wang, 2023). Bu teknik iyi sonuçlar verse de yalnızca yüksek dinamik performans gerektirmeyen ve kararlı çalışma gerektiren çok seviyeli dönüştürücülerde uygulanabilir.

Son yıllarda, çevrim içi olarak harmonik içeriği belirleyen ve SHE yöntemini geliştiren Seçici Harmonik Azaltma Yöntemleri (SHM'ler) daha popüler hale gelmiştir (Moeini, Zhao ve Wang, 2018). SHM-DGM metodu kullanılarak tek fazlı, çift H-köprülü ve çok seviyeli bir evirici üzerinde analizler yapılmıştır (Pourdadashnia ve diğerleri, t.y.). Bu analizlerin amacı sabit ve de değişken iki izoleli DA kaynağı ile çalışan tek fazlı çok seviyeli eviricinin çıkış gerilim kalitesini artırmaktır. Ayrıca, bağımsız modda SHE-DGM tekniğini kullanan, dört tam köprüye sahip tek fazlı 9 seviyeli H-köprü eviricisi için bir teknik önerilmiştir. Bu teknik, üçüncü, beşinci ve yedinci harmonik bileşenleri ortadan kaldırarak çıkış geriliminin temel bileşenini korumayı amaçlar (Vivert ve diğerleri, 2022).

2.2.2. Taşıyıcı Tabanlı Yüksek Frekanslı Modülasyon

Çok seviyeli dönüştürücü topolojilerinde kullanılan Sinüzoidal Darbe Genişlik Modülasyonu (SDGM) yöntemleri, genellikle birden fazla taşıyıcı sinyalle gerçekleştirilir. Bu yöntemler arasında Faz Kaydırmalı Darbe Genişlik Modülasyonu (FK-DGM) ve Seviye Kaydırmalı Darbe Genişlik Modülasyonu (SK-DGM) öne çıkar. SK-DGM, üç farklı faz düzenine sahiptir: Faz Yer Değiştirmeli (FYD), Karşılıklı Faz Yer Değiştirmeli

(KFYD), ve Alternatif Karşılıklı Faz Yer Değiştirmeli (AKFYD). Şekil 5'te bu SK-DGM türlerinin taşıyıcı sinyallerinin dağılımı gösterilmektedir.

Şekil 5. Faz yer değiştirmeli SK-DGM yöntemleri

a)   FYD SK-DGM

b)   KFYD SK-DGM
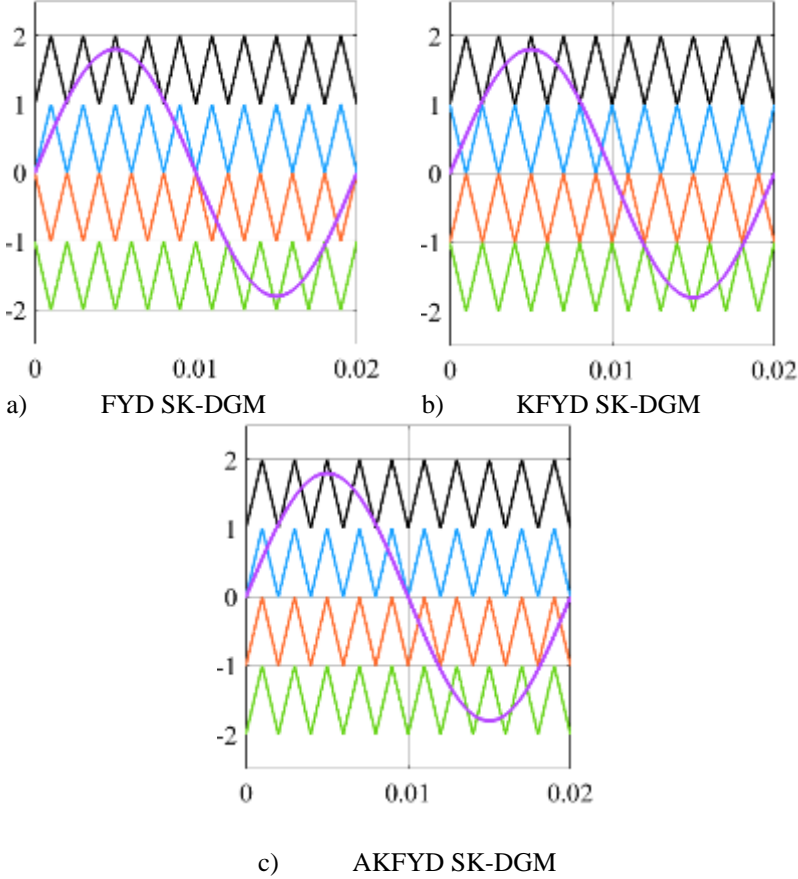
c)   AKFYD SK-DGM

SK-DGM yöntemleri, özellikle FYD-SK-DGM, harmonik performans açısından FK-DGM'ye göre daha başarılı olabilir ve bu nedenle FYD-SK-DGM daha sık tercih edilen bir topoloji haline gelmiştir. Fakat, SK-DGM her zaman belirli harmonik sıralarında Toplam Harmonik Bozulmaya (THB) neden olabilir. FK-DGM ise taşıyıcı sinyallerin faz kaymasından dolayı THB'yi azaltabilir. Elektriksel manyetik girişim (EMI), yüksek güçlü uygulamalarda endişe kaynağı olmamakla birlikte, SK-

DGM yöntemleri genellikle 5 seviyeli çıkış fazı gerilimi için uygundur ve 4 taşıyıcı sinyal kullanır.

Şekil 6, modülasyon indeksine göre SK-DGM yönteminin anahtarlama işaretlerini göstermektedir.

Şekil 6. SK-DGM anahtarlama işaretleri: Mi= 0.9 (a), Mi= 0.3 (b),
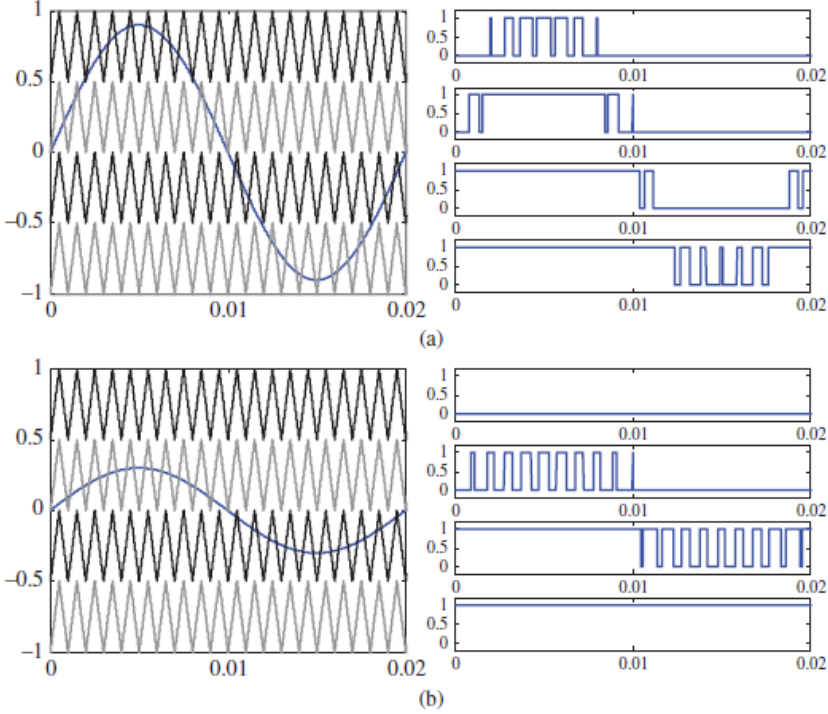
Modülasyon indeksi 0.9 olan yüksek durumda anahtarlama işaretleri normaldir, ancak 0.3 modülasyon indeksinde bazı anahtarlar sürekli kapalı veya sürekli açık kalır, bu da cihazlarda aşırı gerilim ve akım stresine yol açabilir ve güvenilirliği olumsuz etkiler.

Şekil 7'de ise FK-DGM'nin düşük modülasyon indeksinde bu tür problemlerle karşılaşmadığı görülmektedir, bu da FK-DGM'nin bazı uygulamalarda daha yüksek güvenilirlik sağlayabileceğini göstermektedir. Ancak, yapılan çalışmalara bakıldığında diyot kenetlemeli dönüştürücüler için SK-DGM

tabanlı modülasyon topolojilerinin daha başarılı olduğu görülmektedir. Elde edilen çıktılar standartları sağlamaktadır, bu yüzden SK-DGM daha sıklıkla tercih edilmektedir.

Şekil 7. FK-DGM 7 anahtarlama işaretleri: Mi= 0.9 (a), Mi= 0.3 (b)
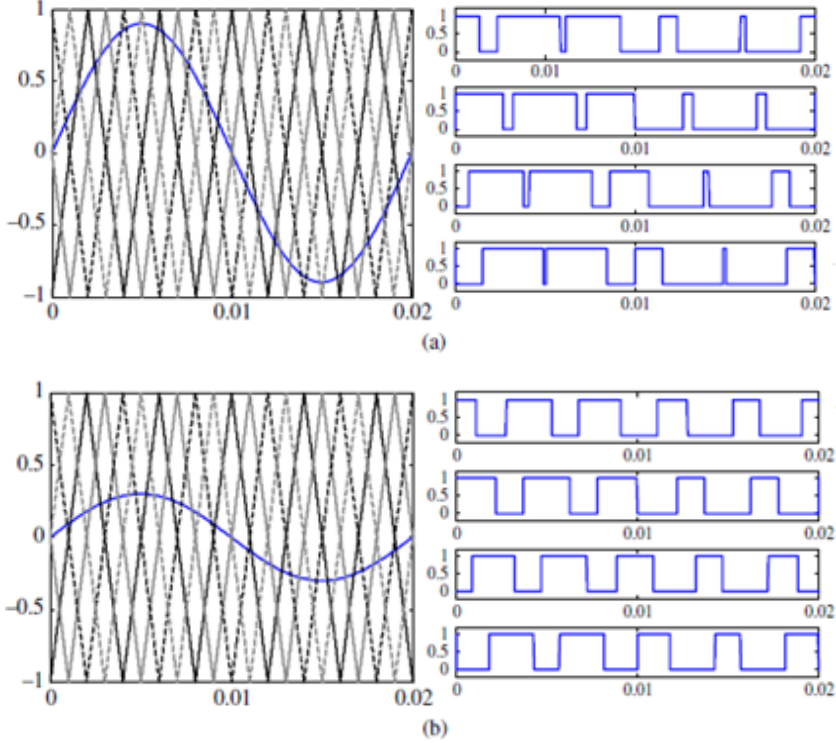
2.2.3. Taşıyıcı Tabanlı Hibrit Frekanslı Modülasyon

Klasik taşıyıcı tabanlı DGM teknikleri çoğu çok seviyeli dönüştürücülere uygulanabilir. Ancak, bazı topolojiler, özellikle asimetrik yapılar, daha iyi performans sağlamak için özel modülasyon yöntemlerine ihtiyaç duyar. Örneğin, asimetrik bir kaskad H-köprü dönüştürücüye Faz Kaydırmalı DGM (FK-DGM) yöntemi uygulandığında, hücreler arasında güç kayıpları oluşmaktadır (Leon ve diğerleri, 2017). Benzer şekilde, beş seviyeli diyot kenetlemeli bir dönüştürücü, UVM yöntemiyle çalıştırıldığında asimetrik yapı nedeniyle optimal olmayan

anahtarlama kayıpları meydana gelir. Bu gibi durumlarda, hibrit frekanslı modülasyon yöntemleri geliştirilerek hem anahtarlama kayıpları en aza indirilebilir hem de güç cihazları arasındaki güç dağılımı dengelenebilir. Yüksek gerilime dayanması gereken cihazlar düşük frekansta anahtarlanırken, düşük gerilimli cihazlar yüksek kalitede çıkış dalga formu yakalamak için yüksek frekanslı bir DGM ile çalıştırılır. Bu yaklaşım, özellikle yüksek güçlü uygulamalar için uygun olup verimliliği artırır (Monopoli ve diğerleri, 2024).

Şekil 8'de, hibrit topolojiler ve asimetrik kaskad H-köprü topolojisi için karışık frekans modülasyonuyla elde edilen seviyeler gösterilmektedir.

Şekil 8. Karışık frekans modülasyonu: Asimetrik kaskad (a) ve hibrit topolojiler (b)
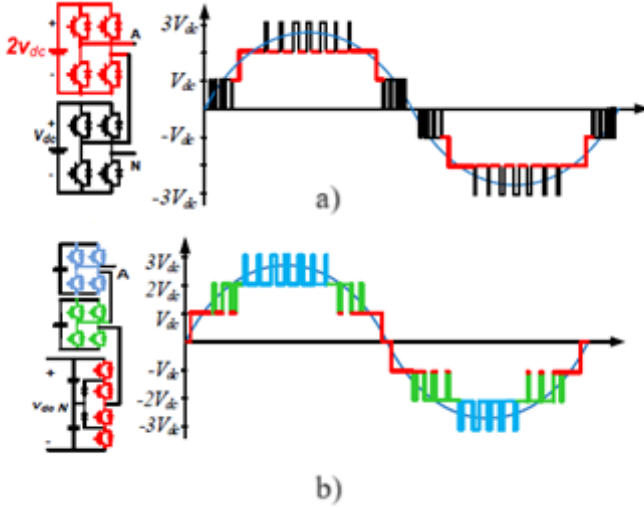
Üst hücreler düşük frekansta anahtarlanarak anahtarlama kayıpları azaltılırken, alt hücreler yüksek frekansla anahtarlanarak Toplam Harmonik Bozulma (THB) azaltılmaktadır. Hibrit frekans modülasyonu, asimetrik yapıların yanı sıra simetrik yapılara da uygulanabilir.

Literatürde hibrit frekanslı modülasyonun bir yöntemi, taşıyıcı sinyallerin formunu değiştirmektedir. Üçgen taşıyıcıları kullanmak yerine farklı sinyal formları kullanılarak karışık frekansta anahtarlama sinyalleri üretilebilir. Şekil 9'da literatürde yer alan çeşitli taşıyıcı sinyaller gösterilmektedir (Chitra ve Valluvan, 2020; Mollahasanoglu vd., 2023; Özkop, 2022; Singh ve Mandal, 2023).

Şekil 9. Taşıyıcı sinyal (TS) formları
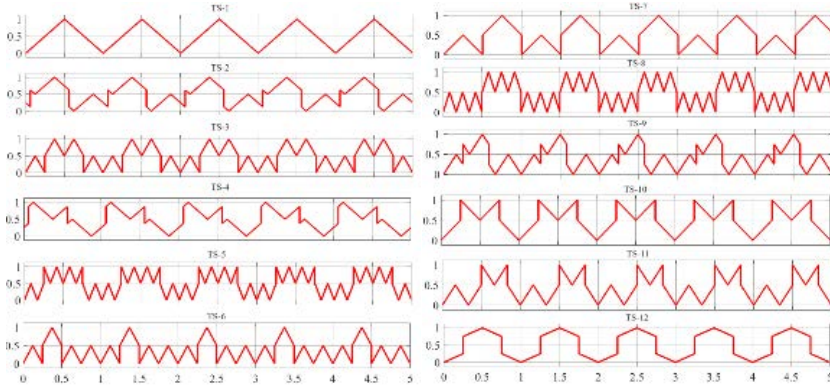
3. SONUÇ

Çok seviyeli dönüştürücüler, günümüz güç elektroniği uygulamalarında büyük bir öneme sahiptir. Elektrikli araçlar, yenilenebilir enerji sistemleri ve hızlı şarj istasyonları gibi alanlarda sağladıkları avantajlar, bu teknolojilerin yaygınlaşmasını desteklemektedir. Bu dönüştürücüler, yüksek verimlilik ve düşük harmonik distorsiyon sunarak enerji kayıplarını minimize etmekte ve sistem performansını artırmaktadır.

Modülasyon yöntemleri, çok seviyeli dönüştürücülerde performansın artırılmasında kritik bir rol oynamaktadır. Taşıyıcı tabanlı darbe genişlik modülasyonu (DGM), yüksek çıkış gerilimleri sağlarken, uzay vektör modülasyonu (UVM) ise daha

iyi çıkış kalitesi ve daha az harmonik distorsiyon sunmaktadır. Her iki yöntem de belirli avantajlar ve dezavantajlar taşımaktadır. Örneğin, DGM'nin uygulanabilirliği daha basitken, UVM daha karmaşık hesaplamalar gerektirebilir, bu da belirli uygulamalarda sistemin kontrolünü zorlaştırabilir.

Ayrıca, modülasyon yöntemlerinin seçimi, uygulamanın gereksinimlerine, sistem dinamiklerine ve tasarım hedeflerine bağlı olarak dikkatlice değerlendirilmelidir. Örneğin, yüksek güç uygulamalarında verimlilik ön planda iken, düşük güç uygulamalarında çıkış kalitesi daha kritik olabilir. Bu nedenle, her uygulama için en uygun modülasyon yöntemi belirlenmeli ve sistem tasarımında bu yöntemlerin etkileri göz önünde bulundurulmalıdır.

Sonuç olarak, çok seviyeli dönüştürücülerin etkin kullanımı ve uygun modülasyon yöntemlerinin seçimi, enerji verimliliği ve sistem performansının artırılmasında önemli bir etkiye sahiptir. Gelecek araştırmalarda, bu modülasyon tekniklerinin daha da geliştirilmesi ve yeni uygulama alanlarının keşfedilmesi, güç elektroniği alanındaki ilerlemeleri destekleyecektir.

KAYNAKÇA

Andler, D., Kouro, S., Perez, M., Rodriguez, J. ve Wu, B. (2009). Switching loss analysis of modulation methods used in neutral point clamped converters. *2009 IEEE Energy Conversion Congress and Exposition* içinde (ss. 2565-2571). 2009 IEEE Energy Conversion Congress and Exposition, sunulmuş bildiri, San Jose, CA, USA: IEEE. doi:10.1109/ECCE.2009.5316040

Boopathi, R., Jayanthi, R. ve Ansari, M. M. T. (2020). Maximum power point tracking-based hybrid pulse width modulation for harmonic reduction in wind energy conversion systems. *Computers & Electrical Engineering*, *86*, 106711. doi:10.1016/j.compeleceng.2020.106711

Chitra, S. ve Valluvan, K. R. (2020). Design and implementation of cascaded H-Bridge multilevel inverter using FPGA with multiple carrier phase disposition modulation scheme. *Microprocessors and Microsystems*, *76*, 103108. doi:10.1016/j.micpro.2020.103108

Kouro, S., Perez, M., Robles, H. ve Rodriguez, J. (2008). Switching loss analysis of modulation methods used in cascaded H-bridge multilevel converters. *2008 IEEE Power Electronics Specialists Conference* içinde (ss. 4662-4668). 2008 IEEE Power Electronics Specialists Conference, sunulmuş bildiri, Rhodes, Greece: IEEE. doi:10.1109/PESC.2008.4592703

Leon, J. I., Kouro, S., Franquelo, L. G., Rodriguez, J. ve Wu, B. (2016). The Essential Role and the Continuous Evolution of Modulation Techniques for Voltage-Source Inverters in the Past, Present, and Future Power Electronics. *IEEE Transactions on Industrial Electronics*, *63*(5), 2688-2701.

IEEE Transactions on Industrial Electronics, sunulmuş bildiri. doi:10.1109/TIE.2016.2519321

Leon, J. I., Vazquez, S. ve Franquelo, L. G. (2017). Multilevel Converters: Control and Modulation Techniques for Their Operation and Industrial Applications. *Proceedings of the IEEE*, *105*(11), 2066-2081. Proceedings of the IEEE, sunulmuş bildiri. doi:10.1109/JPROC.2017.2726583

Maswood, A. I. ve Tafti, H. D. (2018). *Advanced Multilevel Converters and Applications in Grid Integration*. John Wiley & Sons.

Moeini, A., Zhao, H. ve Wang, S. (2018). A Current-Reference-Based Selective Harmonic Current Mitigation PWM Technique to Improve the Performance of Cascaded H-Bridge Multilevel Active Rectifiers. *IEEE Transactions on Industrial Electronics*, *65*(1), 727-737. IEEE Transactions on Industrial Electronics, sunulmuş bildiri. doi:10.1109/TIE.2016.2630664

Mollahasanoglu, H., Mollahasanoglu, M. ve Ozkop, E. (2024). Comparative study of single-phase multilevel cascaded transformerless inverters with different modulation methods. *Engineering Science and Technology, an International Journal*, *51*, 101652. doi:10.1016/j.jestch.2024.101652

Mollahasanoglu, M., Mollahasanoglu, H. ve Okumus, H. I. (2023). A New PWM Technique for Three-Phase Three-Level Neutral Point Clamped Rectifier. *Arabian Journal for Science and Engineering*. doi:10.1007/s13369-023-08312-8

Mollahasanoglu, M., Mollahasanoglu, H. ve Okumus, H. (2023). New modified carrier-based level-shifted PWM control for NPC rectifiers considered for implementation in EV

fast chargers. *Turkish Journal of Electrical Engineering and Computer Sciences*, *31*(7), 1255-1275. doi:10.55730/1300-0632.4046

Monopoli, V. G., Alcaide, A. M., Bruno, L., Rendine, G., Leon, J. I., Liserre, M. ve Franquelo, L. G. (2024). A Hybrid Modulation Technique for Operating Medium-Voltage High-Power CHB Converters Under Grid Voltage Disturbances. *IEEE Transactions on Industrial Electronics*, *71*(1), 462-472. IEEE Transactions on Industrial Electronics, sunulmuş bildiri. doi:10.1109/TIE.2023.3241246

Özkop, E. (2022). Şebeke Bağlantılı Tek Fazlı Transformatörsüz Evirici için Modifiye Edilmiş Taşıyıcı Temelli DGM Kontrolü. *EMO Bilimsel Dergi*, *12*(2), 7-14.

Palanisamy, R., Singh, M., Ramkumar, R., Usha, S., Thentral, T. M. T., ve Kitmo. (2023). Capacitor voltage unbalance minimization for three-phase five-level diode-clamped inverter using hexagonal hysteresis space vector modulation. *Multiscale and Multidisciplinary Modeling, Experiments and Design*. doi:10.1007/s41939-023-00238-w

Pourdadashnia, A., Farhadi-Kangarlu, M., Tousi, B. ve Sadoughi, M. (t.y.). SHM-PWM technique in a cascaded H-bridge multilevel inverter with adjustable DC-link for wide voltage range applications. *International Journal of Circuit Theory and Applications*, *n/a*(n/a). doi:10.1002/cta.3519

Singh, A. K. ve Mandal, R. K. (2023). Switched-capacitor-based five-level inverter with closed-loop control for grid-connected PV application. *Computers and Electrical Engineering*, *108*, 108686. doi:10.1016/j.compeleceng.2023.108686

Vivert, M., Diez, R., Cousineau, M., Bernal Cobaleda, D., Patino, D. ve Ladoux, P. (2022). Real-Time Adaptive Selective Harmonic Elimination for Cascaded Full-Bridge Multilevel Inverter. *Energies*, *15*(9), 2995. doi:10.3390/en15092995

Yang, J., Liu, Q., Li, C., Yu, Y. ve Wang, L. (2023). Online adaptive SHE algorithm for multilevel converters and implementation with embedded control system. *Energy Reports*, Selected papers from 2022 International Conference on Frontiers of Energy and Environment Engineering, *9*, 1190-1202. doi:10.1016/j.egyr.2023.04.215

A NOVEL APPROACH TO COMPLEX ACTIVITY RECOGNITION WITH APPLICATION TO FOOTBALL VIDEO GAME[1]

Celal Onur GÖKÇE[2]

Uğur HALICI[3]

1. INTRODUCTION

Given a video containing human/humans performing some actions, whether simple as breathing or complex as activities in a movie, human behavior understanding problem is to find the class of actions performed automatically. Most studies in the literature are on datasets with complexity levels of simple actions like walking and running. The problem is attacked with several approaches using different feature extraction and classification methods. While shape features, which are global or local shapes of body or body parts in each frame, are independent of other frames, motion features, which are obtained by optical flow or spatio-temporal filters, encode information considering changes between frames. A survey of human behavior understanding is given in Turaga et al., 2008.

İkizler and Duygulu. 2007, represented shape of each pose by histograms of oriented rectangular patch features. For classification, Support Vector Machine (SVM) and some other

---

[1] This study is produced from PhD Thesis of Celal Onur Gökçe.

[2] Assist. Prof. Dr., Afyon Kocatepe University, Faculty of Engineering, Department of Software Engineering, cogokce@aku.edu.tr, ORCID: 0000-0003-3120-7808.

[3] Prof. Dr., Middle East Technical University, Faculty of Engineering, Department of Electrical and Electronics Engineering, halici@metu.edu.tr, ORCID: 0000-0002-2469-1163.

classifiers such as Dynamic Time Warping (DTW) were employed. Bobick and Davis, 2001, aggregated background subtracted images to a single 2D image called motion history image. Hu moments were computed as feature descriptors and Mahalanobis distance was used as classifier.

Veeraraghavan et al., 2005, used a sparse statistical shape descriptor to extract features from binarized silhouette. As classifiers, autoregressive model and DTW were used. In Kepenekçi, 2011, 3D Gabor filters selected by genetic algorithm were used as features. Profile HMM was used as classifier to recognize the behavior. In Schuldt et al., 2004, ST jets of order four were used as feature descriptor. NNC and SVM were used as classifier. In Dollár et al., 2005, a new ST interest point detector consisting of spatial and temporal parts was proposed. In a cuboid around interest points, a feature descriptor considering brightness gradient was computed. K-means algorithm was used to construct a library of cuboids. NNC and SVM were used for classification. In Niebles and Fei-Fei, 2007, a hierarchical model considering spatial shape features described in Belongie et al., 2002, and cuboid features described in Dollar et al, 2005 were used. PCA was used for dimension reduction, Expectation Maximization (EM) was used for estimating parameters of the hierarchical model and SVM was used for classification.

In Efros et al., 2003, a four channel optical-flow based motion descriptor was used as feature descriptor. A version of normalized correlation was used to compare different feature vectors. World Cup football game was used to test the proposed approach. This dataset resembles to our newly generated football video game dataset which will be explained in detail below. But it is quite primitive compared to ours. In their dataset, only actions of running and walking in 8 different directions are used.

In Ofli et al., 2014, an easy-to-implement representation for human actions based on skeletal joint selection was proposed. The actions were represented as sequence of most informative joints. Selection of joints was based on interpretable measures like mean or variance of joint angle trajectories. In Yang and Tian, 2014, an action descriptor based on differences of skeletal joints was proposed. An informative frame selection scheme was used to reduce computational cost. A non-parametric Bayes Classifier is used for classification. In Wang et al., 2014, a representation of interaction of a subset of human joints was used as a model. A 3D appearance feature that describes the depth appearance near a joint was proposed. Additionally, a discriminative temporal representation robust to noise was used.

In this study, it is intended to examine complex actions in Human Behavior Understanding problem. Since the existing datasets available in literature are insufficient to include complex actions, firstly a new dataset, which is called the Football Video Game (FVG) Dataset, is established to fulfill the requirement. Then, a grammar based hierarchical architecture proposed for recognition of these activities, which are composed of several atomic actions and some of these atomic actions being common in different type of activities.

The organization of the rest of the paper is as follows: The FVG dataset that we established is explained in Section 2. The details of the proposed hierarchical architecture are given in Section 3. The experimental results obtained on the FVG dataset are presented in Section 4. Finally, the study is concluded in Section 5.

2. THE FOOTBALL VIDEO GAME DATASET

Note that most of the datasets in the literature consist of simple actions like walking, running, hand waving, etc. Actually

human activities range from simple actions to more complex actions. In order to have a dataset having some complex actions, football game is chosen. In order to build a more controlled dataset, instead of using real football games, football video game is chosen.

FIFA2011 computer simulation game is played naturally and samples are recorded at 1920x1080 resolution with 25 fps using video capture software of NCH software suite. Some of the samples recorded are used for generating atomic action dataset. Each of the atomic actions last for half second and consists of 12 frames. Totally there are 215 atomic actions in the dataset. Mixture of poses algorithm is tested on this dataset. The types of simple actions are as follows: 1) ballAlone: none of the players controls ball and ball is alone, 2) beat: two or more rival players fight for control of the ball, 3) hitBall: a player hits the ball, 4) maneuver: a player changes direction while moving with the ball, 5) run: a player controlling the ball runs straight with the ball, 6) takeBall: a player takes control of the ball. Some sample actions taken from atomic action dataset are shown in Figure 1.

Activities are videos consisting of several atomic actions cascaded sequentially. In activity dataset, there are totally 40 videos each consisting one of five types of activities: 1) Drippling consists of runs and optionally maneuvers, 2) LongPass consists of hitBall followed by one or more ballAlone and finished by takeBall, 3) Lose consists of run followed by beat and finished by ballAlone, 4) ShortPass resembles longPass with the difference that there is no ballAlone but only hitBall and takeBall, 5) Tackle consists of run followed by beat and finished by run.
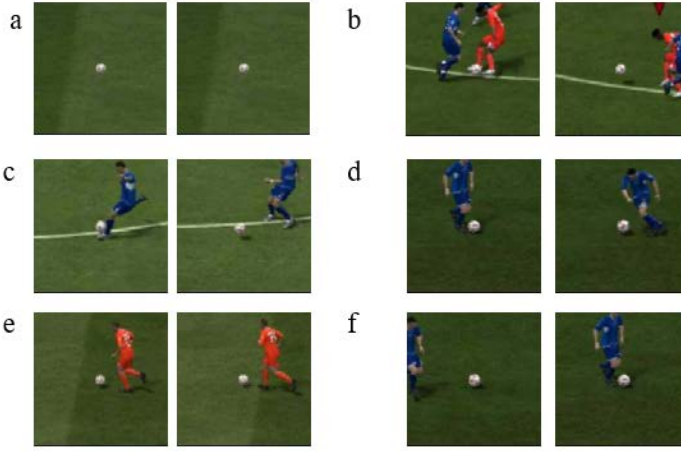
Figure 1 Sample figures from atomic action dataset: a) ballAlone b) beat c) hitBall d) maneuver e) run f) takeBall

Activities are complex three dimensional data. Each activity video consists of several sequential atomic actions. In our dataset of activities, there are 40 videos. Each activity is one of five classes: 1) Drippling is several sequential runs and sometimes may include maneuvers, 2) Long pass is composed of hit ball action at start followed by one or several ball alone actions and lastly take ball action, 3) Lose starts with run action followed by beat action and sometimes lasts with ball alone action, 4) Short pass is similar to long pass without ball alone action, 5) Tackle starts with run action followed by beat action and lasts with run action again.

Note that these activities can be recognized by both CFG and HMM. But it is known that theoretically there are sequences that CFG can recognize but HMM cannot. Here we give an example of such activity. In football game, when a team achieves the score it aims, they would like to pass time by making some common activities. One example is passing the ball around among players. Instead of attacking, the team members just pass between each other in order to gain time. This corresponds to

sequences where number of pass activity is higher than total of other activities.

3. PROPOSED APPROACH

Below in Figure 2 is shown the proposed approach as block diagram.

Figure 2. Block Diagram of The Proposed Approach
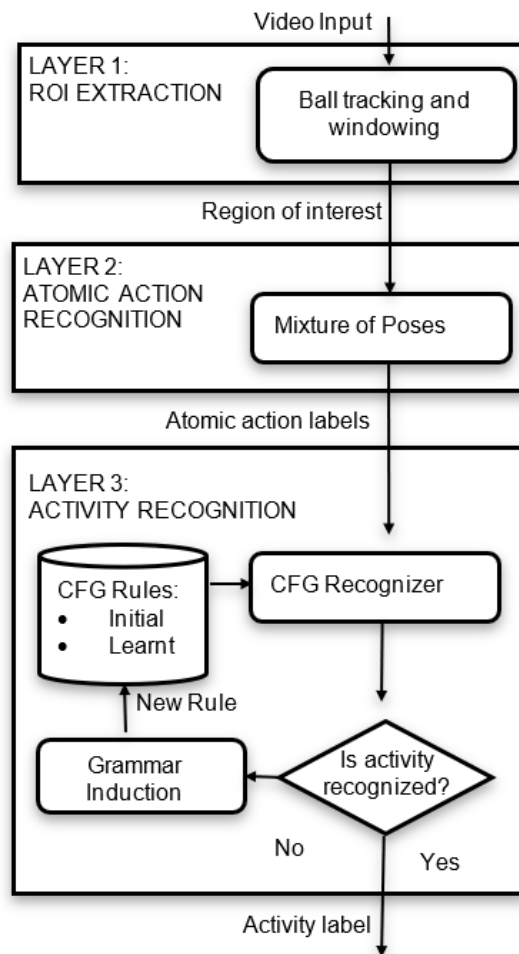
A complex activity data is given as input to the proposed system. First, area of interest is found around the ball. The most important area is where the ball resides in games especially in football game; therefore, it is around ball also for FVG Dataset. The ball detection and tracking block in Layer 1 serves to extract region of interest (ROI) which is simply a sub video of certain duration centered on ball.

Note that an activity like a type of attack of several seconds is composed of simpler atomic actions occurring sequentially. Next process after extraction of ROI is to classify the atomic action occurring around ball.

Mixture of Poses (MoP) that we proposed in Halıcı and Gökçe, 2013, is employed for atomic action recognition in Layer2. The atomic actions to be recognized for FVG dataset were explained previously in Section 2. The output of atomic action classification layer is given as input to the next upper layer.

Layer 3 serves for recognizing the activity consisting of the series of atomic actions labeled in the previous layer. A Grammar based method is proposed for activity recognition in this last layer. Two main types of activities in our study are manually taught and learnt by thee system. A Context Free Grammar (CFG) based recognizer is used for pre-taught activities and a grammar induction block is used for learning new rules. Output of context-free-grammar block is the label of the activity to be recognized. In case the activity is not recognized the grammar induction block serves for learning new CFG rules which are added to the rule set for being used in recognition of even further activities.

Alternatively, using cuboid features of Dollar et.al. together with k-NN and SVM classifiers is considered for the atomic action recognition layer, and HMM is considered for the

activity recognition layer for comparison of the performances on the FVG dataset

In the following subsections, each layer is explained in detail.

3.1.Ball Detection and Tracking

For detection and tracking of ball, algorithm in Liang et al.'s, 2005, is used. Initial performance with the original algorithm is very low. This is due to the difference of appearance of ball in video games and real football matches. Images of ball can be different between adjacent frames in video games which is shown in Figure 3 below.

Figure 3. Image of Ball in Two Adjacent Frames in Football Video Game
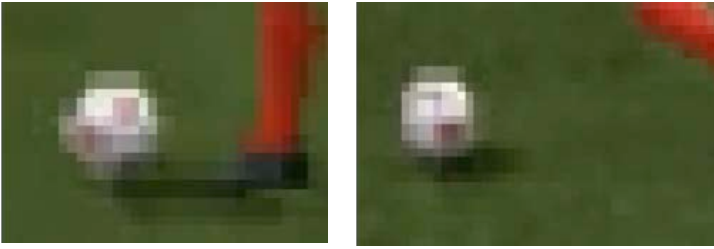
For this reason, for ball detection a discriminative solution is used. Multi-Layer Perceptron (MLP) Duda et al., 2000, is used for ball detection in this study.

In order to use MLP as a ball detector, a ball image dataset is constructed with 142 positive and 187 negative sample images of 12x12 pixel size.

In this study an MLP with 20 nodes in the hidden layer is used. The output layer contains 1 node output of which is 1 for the positive samples and -1 for negative samples. The input layer has 432 nodes, which is determined by the ball sizes in the dataset. An average ball size of 12x12 pixels with 3 color channels corresponds to a vector of size 432. Backpropagation algorithm

Duda et al., 2000, is employed with 2000 iterations to train the network. Since false positives are observed to be more than acceptable, learning with queries Duda et al., 2000, is further employed to improve performance. For this purpose, MLP trained using the dataset mentioned above is used as initial detector. A sample frame in the video is searched and whenever output of the MLP is positive indicating that a ball is found, its validity is checked. False positives are included in the training dataset. The procedure is repeated with other sample frames until the performance reached to 97%. Note that this resembles to the well-known Ada-Boost algorithm in a sense. Most informative negative samples are collected using learning with queries method in this way. At the end the number of negative samples reached to 273.

In the initial frame, the ball is found using MLP by searching the whole frame and detecting the highest score window as ball. This approach is computationally expensive since all of the frame is searched and MLP detector is utilized for each sub frame. A ball tracker is utilized to reduce computational load. Particle filter is tried as first alternative. Even with 1000 particles performance was lower than acceptable. Increasing the number of particles is not feasible due to excessive computational cost. As a more feasible alternative tracker a simple tracking algorithm, that is named as growing window tracker, is utilized in this study.

It is assumed that in between two consecutive frames ball cannot move to pixels which have distance above a certain threshold since time between two consecutive frames is very small. This fact suggests to search for ball in next frame within relatively small neighborhood of ball's position in last frame. A neighborhood of 20 pixels in each direction is searched initially and this neighborhood is enlarged iteratively if the ball is not found. This initial neighborhood of 20 pixels is chosen by considering balls maximum velocity. The size of neighborhood is

increased linearly for 5 consecutive frames since distance of ball after each consecutive frame is likely to be increased linearly with time. Failure of detection after 5 iterations with this method results in restarting the search for whole frame.

3.2. Atomic Action Recognition Layer

3.2.1. Mixture of Poses

In this study, we use the Mixture of Poses (MoP), which is a global shape descriptor that we proposed recently in Halıcı and Gökçe, 2013, in order to model an action class for a single person, where Weizmann dataset were used in testing. Although it resembles somehow the approach proposed in Niebles and Fei-Fei, 2007, since both uses Mixture of Gaussians (MoG), they are quite different. MoP uses MoG as a global shape descriptor while the approach in Niebles and Fei-Fei, 2007 uses them mainly as local shape and motion descriptors.

First phase of MoP algorithm starts with background subtraction. Median background subtraction is used first but the performance was far from being satisfactory. For this reason, background subtraction method is enhanced by subtracting green and white pixels, where green pixels are grass and white pixels correspond to field lines. Below are some pictures of foreground extracted.

Figure 4. Foreground Frames Extracted Using Background Subtraction Method
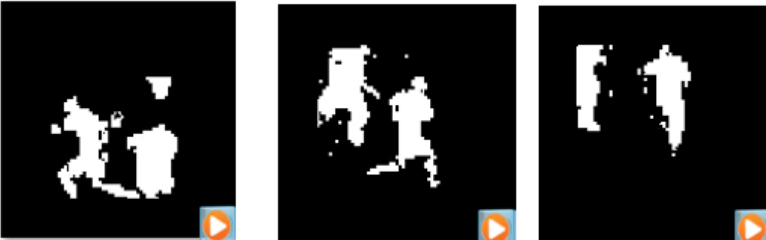
In MoP, Shape Context Descriptors (SCDs) Belongie et al., 2002, are extracted for each frame, which is called a pose, in all sample videos in the training set and their sizes are reduced by Principle Component Analysis (PCA). The collection of reduced size SCDs for an action class for a single person is employed in modeling that action of that person. First the center poses are obtained by utilizing K-Medoid Clustering on the collection. Note that numbers of center poses are found adaptively depending on the complexity of action. This means that for actions having more different poses, more center poses are found to represent the action. This number is found as follows. First, average distance between all poses is found. Then, the first frame is selected as the first center pose. Following frames are each compared to existing center poses and if any frame is further than certain threshold, which is chosen to be 150% of average distance, then that frame is initiated as a new center pose. The center poses are used both to determine number of mixtures automatically and also to initialize EM algorithm to extract MoGs.

MoP's are the MoGs extracted in this way to model each different action class with all videos belonging to that class and they are collected in a library in order to be used for comparison in recognition phase. Notice that, the number of mixtures in MoPs obtained as explained above is not fixed, but depends on the inner structural complexity of the action and the style of the performer.

In the recognition phase, the MoP is extracted for the input video and compared with each MoP available in the library using L2 norm which is the distance between two MoGs. To deal with computational complexity, instead of L2 norm integral computation, discrete sum within hyper cubes centered around the Gaussian means is calculated. The label of the closest class of MoP in the library obtained from training set is assigned.

3.2.2. Fisher Vector Representation to Improve Speed Performance

In MoP, computation of the distance between MoGs has very high cost. In order to deal with computational complexity, Fisher vector representation is used, Vedaldi and Fulkerson, 2008. Fisher vector representation allows representing MoG as a single vector. Each part of the vector represents a mode in MoG. Vectors obtained are reduced to the length of the shortest vector. Fisher Vector Representation is also used in other studies on action recognition, Castro et al., 2014, Peng et al., 2014.

3.2.3. Cuboid Features

Cuboid features in Dollar et al. 2005 are used to recognize atomic actions as an alternative action recognition method for performance comparisons on the FVG Dataset. One dimensional Gabor filter is used to find local maxima. Gradient data is used as features in cuboid volumes around regions of interest. Nearest neighbor classifier and SVM are utilized to classify features. The popularity and success of cuboid features is well known. The results are reported in Section 4.

3.3. Activity Recognition Layer

In activity recognition layer, complex activities like attack types are detected. These are longer videos lasting a few seconds. In order to compare the results, two frameworks are utilized. First, HMM is utilized which can be considered as FSM with probability concepts incorporated. HMMs are popular classifiers in applications like automatic speech recognition where the data is sequential in time. Note that activities are also sequential data which is a suitable problem to utilize HMM. CFG is used as a novel alternative, which is higher in the hierarchy of computation than FSM so that theoretically can recognize more complex data that FSM cannot. The novelty of using CFG in this study stems

from the learning part which is different from other studies in the literature. This is the main and novel effort done in this study.

Each approach is explained below.

3.3.1. HMM for Activity Recognition

HMM, which is introduced in Rabiner, 1989, is utilized widely as classifier in the literature especially for solution of automatic speech recognition problem. In this study, HMM is utilized in the layer of activity recognition. Atomic actions detected in the corresponding lower layer are given as input to HMM and complex activity class is detected. Results are reported in corresponding section of this study.

3.3.2. CFG LEARNING for Activity Recognition

Context free grammars are higher than finite state machines in the hierarchy of computation and can recognize more complex data.

A context free grammar (CFG) is a 4-tuple G = (N, T, P, S), where:

N: a finite set of non-terminal symbols

T: a finite set of terminal symbols

P: a finite set of production rules of the form A-> β, where A ∈ N, β ∈ (N U T)*

S: S ∈ N is the starting symbol.

In theory, a PDA can be used to recognize a CFL. The problem with the PDA approach to language recognition is in the nondeterministic nature of PDAs. With their naïve forms, they cannot be converted to standard computer programs which are deterministic in nature. Although any nondeterministic FSM (NFSM) has a corresponding deterministic FSM (DFSM) and a standard procedure exists to convert NFSM to DFSM, this is not

the case with PDAs, Martin, 2003. There may be languages that can only be recognized with nondeterministic PDAs. So, other techniques instead of straight implementation of PDAs are used to recognize CFLs. Language recognition problem can be defined informally as deciding whether given a string is in the language or not. During recognition, it may also be possible to infer how a string is derived with the language rules. Inferring the derivation of the string is called parsing.

There are several parsing algorithms for CFGs. The one used in this study is called CYK (Cook, Yunger and Kasami) algorithm, Hopcroft et al., 2007.

The CYK algorithm used uses a special form of CFG, namely revised Chomsky normal form, where all the production rules are of the form:

$$A \rightarrow \alpha 1 \alpha 2 \ , \ \alpha 1, \alpha 2 \in (N \cup T)$$

The CYK algorithm requires a grammar and a string to check whether the string belongs to the grammar. It is also possible to learn the grammar from samples strings that do and do not belong to the grammar. This problem is known as "grammar induction" in literature and for CFGs it is mentioned to be a hard problem. It is shown theoretically in Gold, 1967, that learning an arbitrary CFG from only positive samples is not possible. But natural languages are higher than CFGs in the Chomsky hierarchy and humans can learn from only positive samples Marcus, 1993.

The grammar induction algorithm used in this study is so called Synapse, Nakamura and Ishiwata, 2000, which has the inductive CYK algorithm at its core Nakamura and Ishiwata, 2000.

Note that Synapse and Inductive CYK are nondeterministic algorithms, which have to be converted to the deterministic versions in order to code in conventional computers,

Floyd, 1967. Writing programs in nondeterministic way makes them shorter and more intuitive but this requires a systematic and careful conversion procedure.

As a domain of interest, football matches are chosen in this study for the reasons explained in section 2. The ultimate aim of the system in this domain will be the following: Given a full length football match, the system will divide it into sub-videos composed of several activities where each can be defined by a grammar learned previously. A 90 minute of video input can be analyzed and as output the structure of the video will be given by sequences of recognized activities.

4. EXPERIMENTAL RESULTS

As ball detector MLP is used as explained previously. Below results for both multilayer neural networks trained with Backpropagation and those for enhanced detector with learning with queries are given in Table 1. The recognition performance of MLP with BP is 88% and it is improved to 97% when learning with queries is employed.

Table 1. Confusion matrix for ball detection with MLP trained with BP and Learning with Queries

	MLP		Learning with Queries	
	ball	not ball	ball	not ball
ball	99	1	99	1
not ball	128	872	37	963

In middle layer three approaches are used in this study for comparison. One is the well-known Dollar et al.'s, 2005, cuboid features. The other is an approach proposed in Halıcı and Gökçe, 2013, named as Mixture of Poses. Third is Fisher Vector Representation, Vedaldi and Fulkerson, 2008. MoP and Fisher

Vector Representation gives clearly better recognition rate as shown in Table 2. Details of the results are given in Table 3 as confusion matrix.

Table 2. Recognition Rates (%) for Atomic Actions

Atomic Actions	#of videos	Recognition rate (%)		
		MoP-L2	Mop-FV	Cuboid-SVM
a: ballAlone	25	84.0	80.0	68.0
b: beat	15	20.0	20.0	33.3
h: hitBall	15	13.3	13.3	13.3
m: maneuver	15	6.7	6.7	6.7
r: run	110	95.7	92.2	75.7
t: takeBall	30	40.0	40.0	13.3
overall	215	69.3	67.0	54.0

Table 3. Confusion Matrix for Classifying Six Atomic Action Types for MoP-L2/MoP-FV/Cuboid-SVM

	a	b	h	m	r	t
a	21/20/17	0/0/0	1/2/1	0/0/0	0/0/5	3/3/2
b	0/0/0	3/3/5	2/2/0	2/2/1	7/7/6	1/1/3
h	0/0/1	2/2/1	2/2/2	1/1/6	2/2/1	8/8/4
m	0/0/0	2/2/1	2/2/2	1/1/1	9/9/6	1/1/5
r	0/0/5	1/2/7	1/1/0	2/5/5	110/106/87	1/1/11
t	2/2/1	4/4/4	6/6/5	1/1/5	5/5/11	12/12/4

The performance results for activity recognition layer with MoP in atomic action recognition layer are given in Table 5.

Table 5. Recognition Rates (%) for Activities

| Activities | #of videos | Recognition rate (%) | | | |
| | | MoP_in layer 2 | | Manual feed | |
		HMM	CFG	HMM-M	CFG -M
d: drippling	10	70.0	70.0	100	100
p_l: longPass	10	60.0	60.0	100	100
l: lose	5	60.0	60.0	100	100
p_s: short pass	10	60.0	60.0	100	100
t: tackle	5	60.0	60.0	100	100
overall	40	62.5	62.5	100	100

Table 6 Confusion Matrix for Whole System with MoP in Atomic Action Recognition Layer

	d	p_l	l	p_s	t	none
d	7	0	0	0	0	3
p_l	0	6	0	0	0	4
l	0	0	3	0	0	2
p_s	0	0	0	6	0	4
t	0	0	0	0	3	2

5. CONCLUSIONS AND FUTURE WORKS

In this study, a novel dataset using football video game is generated. Both simple atomic actions and complex actions called activities exist in the dataset. In order to recognize both atomic actions and activities, a novel hierarchical architecture is proposed and tested.

Results are compared with a widely referenced feature, namely Dollar et. al's cuboid features and well known HMM. Quite encouraging results are achieved for the proposed architecture. For atomic actions 69.3% success rate is observed

by the MoP approach, which clearly exceeds 54.0% of Dollar et. al's success rate.

For activities, 62.5% success rate is observed with MoP and CFG pair while 42.5% is the success of cuboid and CFG layer. When HMM is used instead of CFG in activity recognition, the same recognition performance is obtained if MoP is used for atomic action recognition. Note that when data is fed manually to higher layer, either CFG or HMM, 100% success rate is observed.

CFG is higher in complexity hierarchy than HMM. So, it can recognize more complex sequences that HMM cannot. An example of such a sequence namely passing the ball around activity is provided together with its CFG production rules to show that it can be recognized by CFG.

REFERENCES

Belongie S., Malik J., and Puzicha J.. 2002, Shape matching and object recognition using shape contexts. IEEE Trans. PAMI, 24(4):509–522.

Bobick A. F. and Davis J. W., 2001, "The recognition of human movement using temporal templates," IEEE Trans. Pattern Anal. Mach. Intell., 23(3):257–267.

Castro F.M., Marin-Jimenez M.J., Medina-Carnicer R., 2014, Pyramidal Fisher Motion for Multiview Gait Recognition, Proc. ICPR.

Dollár P., Rabaud V., Cottrell G., and Belongie S., 2005, "Behavior recognition via sparse spatio-temporal features," in Proc. IEEE Int. Workshop Vis. Surveillance Performance Eval. Tracking Surveillance, pp. 65–72.

Duda R. O., Hart P. E., Stork D. G., 2000, Pattern Classification, 2nd edition, Wiley-Interscience.

Efros A. A., Berg A. C., Mori G., Malik J., 2003, Recognizing actions at a distance, Proc. IEEE International Conference on Computer Vision.

Floyd, R. W., (1967), Nondeterministic Algorithms, Jour. of ACM 14, No. 4 636-644.

Gold E. M., 1967, Language identification in the limit. Information and Control, 10:447-474.

Halıcı, U., Gökçe O., 2013, Mixture of Poses for human behavior understanding, Proc. IEEE Conf. CSIP, China, 112-116.

Hopcroft J.E., Motwani R., Ullman J. D., 2007, Introduction to Automata Theory, Languages, and Computation, 3rd edition,.

İkizler N., Duygulu P., 2007, Human Action Recognition Using Distribution of Oriented Rectangular Patches, Proc. ICCV, 271-284.

Kepenekçi B., 2011, Human Activity Recognition by Gait Analysis, PhD Thesis.

Liang D., Liu Y., Huang Q., Gao W., 2005, A scheme for ball detection and tracking in broadcast soccer video, Proc. Advances in Multimedia Information Processing, PCM, pp 864-875.

Marcus, G.F. 1993, Negative evidence in language acquisition. Cognition, 46, 53-85.

Martin J., 2003, Introduction to Languages and the Theory of Computation, 3rd edition, McGraw-Hill.

Nakamura K., Ishiwata T., 2000, Synthesizing Context Free Grammars from Sample Strings Based on Inductive CYK Algorithm, Lecture Notes in Computer Science, 1891: 207-208.

Niebles J. C. and Fei-Fei L., 2007, "A hierarchical model of shape and appearance for human action classification," in Proc. IEEE Conf. CVPR, pp. 1–8.

Ofli F., Chaudhry R., Kurillo G., Vidal R., Bajcsy R., 2014, Sequence of the most informative joints (SMIJ): A new representation for human skeletal action recognition, Journal of Visual Communication and Image Representation Volume 25, Issue 1, Pages 24–38.

Peng X., Zou C., Qiao Y., Peng Q., 2014, Action recognition with stacked fisher vectors - Computer Vision–ECCV 2014, – Springer, pp 581-595.

Rabiner LR, 1989, A tutorial on hidden Markov models and selected applications in speech recognition, Proceedings of the IEEE, pp 257-286.

Schuldt C., Laptev I., and Caputo B., 2004, "Recognizing human actions: A local SVM approach," in Proc. ICPR, pp. 32–36.

Turaga P., Chellappa R., Subrahmanian V.S., Udrea O., 2008, Machine Recognition of Human Activities, IEEE Trans. on circuits and systems for video technology, 18,(11): 1473-1488.

Vedaldi A., Fulkerson B., 2008, {VLFeat}: An Open and Portable Library of Computer Vision Algorithms, http://www.vlfeat.org/, accessed on 15-Jan-2016.

Veeraraghavan A., Roy-Chowdhury A. K., Chellappa R., 2005, "Matching Shape Sequences in Video with Applications in Human Movement Analysis", IEEE Trans. PAMI, vol. 27, no. 12, pp. 1896–1909.

Wang J., Liu Z., Wu Y., Yuan J., 2014, Learning Actionlet Ensemble for 3D Human Action Recognition, IEEE Trans. on PAMI, 36(5), p 914-927.

Yang X., Tian Y., 2014, Effective 3D action recognition using EigenJoints, Journal of Visual Communication and Image Representation Volume 25, Issue 1, p 2–11.

ELEKTRİK-ELEKTRONİK VE HABERLEŞME

MÜHENDİSLİĞİ

yaz
yayınları